I. DEVELOPMENT OF A CRYOGENIC SHOCK TUBE

II. EXPERIMENTAL INVESTIGATION OF THE INTERACTION OF A SHOCK WAVE WITH LIQUID HELIUM I AND II

Thesis by

John C. Cummings

In Partial Fulfillment of the Requirements

For the Degree of

Doctor of Philosophy

California Institute of Technology

Pasadena, California

1973

(Submitted May 11, 1973)

ACKNOWLEDGMENTS

This project has been supported by the Air Force Office of Scientific Research.

Many members of the GALCIT staff have contributed to this work. In particular, the efforts of Mrs. Jacquelyn Beard, Mr. Ray Wagoner, and Mr. Earl Dahl are greatly appreciated.

Professors Bradford Sturtevant, Anatol Roshko, and Donald Coles have given their time, interest, and suggestions. Dr. Harris Notarys has been indispensable as a consultant on experimental problems encountered at cryogenic temperatures.

My wife Ellen has contributed immensely to this effort. Her typing and proofreading have been a great help; her patience and understanding have been invaluable.

Professor Hans W. Liepmann has provided motivation and inspiration. I am indebted to him for his help with this project, for his contributions to my education, and for his friendship.

DEVELOPMENT OF A CRYOGENIC SHOCK TUBE

ABSTRACT

A cryogenic shock tube has been developed as a tool for research in fluid mechanics and low temperature physics. The shock tube is designed to operate with the test section immersed in a cryogenic liquid. A unique diaphragm changing mechanism makes this shock tube an economical and practical device.

There are several advantages in operating a shock tube at cryogenic temperatures. Shock waves of very large Mach number can be produced. The flow field can be accurately calculated using ideal shock tube - perfect gas theory. Boundary layer effects are decreased so that long test times are possible.

The cases which have been studied are test gas temperatures of 300, 77, 4.2, and 2.3°K. Helium is used as both test and driver gas. The largest Mach numbers which have been observed range from 2.4 at 300°K to 32 at 2.3°K (several runs at 1.46°K have produced Mach 40 shocks). As the test gas temperature is decreased the observed Mach numbers approach those calculated using the ideal shock tube equation. The observed test times can be interpreted using laminar or turbulent boundary layer theory if the effects of shock formation distance and wall temperature rise are taken into account.

As a laboratory tool the cryogenic shock tube may be applied in many areas and modified for use in even more. Large Mach number shocks and large Reynolds number flows can be produced with this device. The rapid increase in temperature and pressure

across a shock wave is useful for studies of sublimation, evaporation, or chemical reactions. Quantum mechanical effects in cryogenic materials, superconductors, or superfluid helium can also be investigated.

EXPERIMENTAL INVESTIGATION OF THE INTERACTION OF A SHOCK WAVE WITH LIQUID HELIUM I AND II

ABSTRACT

The flow field produced by a shock wave reflecting from a helium gas-liquid interface has been investigated using a new cryogenic shock tube. Incident and reflected shock waves have been observed in the gas; transmitted first and second sound shocks have been observed in the liquid. Wave diagrams have been constructed to compare the data to theoretical wave trajectories. Qualitative agreement between data and theory has been shown. Quantitative differences between data and theory indicate a need for further analysis of both the gas-liquid interface and the propagation of nonlinear waves in liquid helium.

This work is essentially a first step in the experimental investigation of a very complex nonequilibrium state. The well controlled jump in temperature and pressure across the incident shock wave provides unique initial conditions for the study of dynamic phenomena in superfluid helium.

The results clearly demonstrate the usefulness of the cryogenic shock tube as a research tool.

TABLE OF CONTENTS

TABLE OF CONTENTS (cont'd)

TABLE OF CONTENTS (cont'd)

TABLE OF CONTENTS (cont'd)

TABLE OF CONTENTS (cont'd)

TABLE OF CONTENTS (cont'd)

LIST OF SYMBOLS

p_c	critical pressure
$p_{s.v.}$	saturated vapor pressure
LN_2	liquid nitrogen
LHe	liquid helium
LHe I	liquid helium above the λ-point
LHe II	liquid helium below the λ-point, superfluid helium
OD	outer diameter
ID	inner diameter
U_s	shock wave velocity
x_s	effective shock tube length
t_s	test time as seen by an observer located a distance x_s from the diaphragm
ℓ	test length: separation distance between the shock wave and contact surface
ℓ_m	maximum separation distance between the shock wave and contact surface, i.e., the maximum test length
d	diameter of the shock tube
$X = \frac{x_s}{\eta \ell_m}$ $T = \frac{\ell}{\ell_m}$	similarity parameters used in the boundary layer calculations
T	temperature
η	density ratio across the incident shock wave
C	heat capacity of a solid or liquid
k	heat conductivity
U_{shock}	speed of the incident shock wave

LIST OF SYMBOLS (cont'd)

$\bar{A}$	average value of A data
R. M. S.	root mean square
$\vec{u}$	gas particle velocity
x	distance
t	time
p	pressure
a	speed of sound
$\gamma = C_p/C_v$	ratio of specific heats
C_p	specific heat at constant pressure
C_v	specific heat at constant volume
M	Mach number: ratio of the velocity to the speed of sound
$M_s\Big\vert_{\text{limit}}$	Mach number attained in an ideal shock tube when the diaphragm pressure ratio is infinite
R	gas constant
τ_m	limiting test time
LBL	laminar boundary layer
TBL	turbulent boundary layer
ρ	density
μ	viscosity
HPD	high-performance driver
T_c	critical temperature
θ_i	ionization temperature
$K = \frac{k}{\rho C_p}$	coefficient of thermal diffusivity
$Pr = \frac{C_p \mu}{k}$	Prandtl number

LIST OF SYMBOLS (cont'd)

δ	boundary layer thickness
J	total enthalpy
τ	sheer stress
q	heat flux
$\nu = \frac{\mu}{\rho}$	kinematic viscosity
h	enthalpy
Q	total heat
$\vec{j} = \rho\vec{v}$	mass flux
$\vec{v}$	liquid particle velocity
$\vec{v}_s$	superfluid velocity
$\vec{v}_n$	normal fluid velocity
$\vec{w} = \vec{v}_n - \vec{v}_s$	relative velocity between the normal fluid and superfluid
$\vec{\vec{\pi}}$	stress tensor
s	entropy per unit mass
Φ	chemical potential per unit mass
C_h	specific heat of LHe
C_{10}	infinitesimal amplitude first sound speed
C_{20}	infinitesimal amplitude second sound speed
C_1	finite amplitude first sound speed
C_2	finite amplitude second sound speed
T	time of arrival of the incident shock wave at the liquid surface
L	depth of the LHe measured vertically from the lucite endwall

LIST OF SYMBOLS (cont'd)

$\chi = \frac{L-x}{L}$ $\tau = \frac{t-T}{L}$	similarity parameters used in plotting wave diagrams
ΔT	change in temperature; temperature jump
Δp	change in pressure; pressure jump
p_T	pressure behind the reflected shock after it has collided with the contact surface

LIST OF SUBSCRIPTS

s	shock, incident shock solid superfluid
0, 1, 2, . . . 9	shock tube flow region
1	initial test gas conditions
4	initial driver gas conditions
m	maximum value
w	value at the wall
L	laminar
T	turbulent transmitted
I	incident
R	reflected
o	room temperature conditions
c	critical
s. v.	saturate vapor
i	ionization variable shock tube flow region number
n	normal fluid variable flow region number
e	external flow values, outside the boundary layer
e, o	external flow values at the shock wave
e, ℓm	external flow values at the contact surface
obs	experimentally observed value
ideal	theoretically predicted value
limit	limiting value

LIST OF TABLES

LIST OF FIGURES

LIST OF FIGURES (cont'd)

LIST OF FIGURES (cont'd)

I. INTRODUCTION

I.A. Large Mach Number Shock Tubes

Since its initial use over seventy years ago (Ref. 1) the shock tube has evolved into an extremely valuable tool in the fluid mechanics laboratory.* So many modifications and refinements of the basic concept exist that it is impossible to mention but a few developments pertinent to this paper. Much of the effort to obtain large Mach number shocks has been directed toward techniques to increase the driver gas temperature and pressure. Conventional, electromagnetic, detonation, and wave process methods are the general techniques used with "high performance" driver sections which can generate shock waves of Mach numbers 60 and larger (Ref. 2). Test section modifications to increase shock Mach numbers consist mainly of geometrical convergences. High temperature real gas effects (e.g. rotational and vibrational relaxation, dissociation, ionization, and radiation) are generally of interest in these large Mach number shock tubes.

*For an explanation of shock tube notation and ideal gas-shock tube relations see Appendix A and Figure 1.

I. B. Cryogenics

The increased availability and decreased cost of cryogenic (temperature below ~ 200°K) fluids have in recent years caused a great deal of interest in the use of phenomena which only occur or are enhanced at cryogenic temperatures. The engineering developments of superconducting motors and generators, and cryogenically cooled electrical transmission lines are the most spectacular examples of this interest. In the field of fluid mechanics the advantage of working at cryogenic temperatures has been manifested through the development of a cryogenic ballistics range (Ref. 3), and more recently with cryogenic wind tunnels (Ref. 4) and shock tubes (Ref. 5,6,7).

I. C. Basic Principles of a Cryogenic Shock Tube

I. C. 1. Large Mach Numbers

The shock wave Mach number in an ideal shock tube (containing perfect gases in all flow regions) is related to the diaphragm pressure ratio, the ratio of speeds of sound of the driver and test gases, and the ratio of specific heats for both gases. This relation is commonly known as "the shock tube equation":

$$\frac{p_4}{p_1} = \frac{1 + \frac{2\gamma_1}{\gamma_1+1}\left(M_s^2-1\right)}{\left[1 - \frac{\gamma_4-1}{\gamma_1+1}\frac{a_1}{a_4}\frac{M_s^2-1}{M_s}\right]^{2\gamma_4/(\gamma_4-1)}} \qquad (1)$$

(see Figure 1 for conventional notation used with shock tubes). It is possible to increase the shock Mach number by increasing the ratio of speeds of sound (a_4/a_1). For "cold" (room temperature) driver shock tubes, helium or hydrogen are commonly used as driver gases since they have the largest speeds of sound at room temperature. The "high performance" shock tubes increase the driver gas temperature in order to raise the driver gas sound speed. A cryogenic shock tube can increase the ratio a_4/a_1 by decreasing the temperature of the test gas which lowers the test gas sound speed.

From equation 1 it can be seen that as the diaphragm pressure ratio approaches infinity the shock Mach number approaches a limiting value. That is:

$$p_4/p_1 \to \infty$$

implies that

$$M_s \to M_s\Big|_{\text{limit}} = \frac{A + \sqrt{A^2+4}}{2} \tag{2}$$

where

$$A = \frac{\gamma_1+1}{\gamma_4-1} \quad \frac{a_4}{a_1}$$

Consider the special case of using helium gas as driver and test gas, and assume that the helium behaves as a perfect gas so that $a_i = \sqrt{\gamma R T_i}$. The limiting Mach number takes the form:

$$M_s\Big|_{\text{limit}} = 2\sqrt{\frac{T_4}{T_1}} + 2\sqrt{\frac{T_4}{T_1} + \frac{1}{4}} \tag{3}$$

and the increase of Mach number with increasing T_4 or decreasing T_1 is more evident. To compare the two temperature directions it is convenient to consider $T_4/T_1 \gg \frac{1}{4}$ (not a bad approximation even for $T_4 = T_1$) . Then equation 3 reduces to

$$M_s\Big|_{\text{limit}} \doteq 4\sqrt{\frac{T_4}{T_1}} \tag{4}$$

Equation 4 illustrates the advantage of attaining high Mach numbers with cryogenic temperatures. For a limiting Mach number of 40 the "diaphragm temperature ratio" T_4/T_1 must be 100. The high-performance-driver (HPD) shock tubes generally operate with $T_1 = 300^{\circ}K$ and hence T_4 must approach $30,000^{\circ}K$ to obtain

shock Mach numbers near 40*. If a cryogenic shock tube operates with $T_4 = 300^{\circ}K$ then the test gas must be cooled to $3^{\circ}K$ to achieve the same Mach number. Comparing the energy requirements of the two methods, the heat added to the driver gas per unit mass is over 100 times as large as the heat removed from the test gas.

I. C. 2. The Ideal Shock Tube

There are essentially two processes which can affect the "idealness" of the shock tube itself independent of the "idealness" of the gas used. The first is the diaphragm opening process. The second is the effect of energy and momentum transfer from the gas to the shock tube walls.

In an ideal shock tube (Fig. 1) the diaphragm is a massless piston separating the driver and driven gases. It accelerates impulsively to the ideal piston velocity thus causing instantaneous shock wave formation. The actual diaphragm bursting process is very different from this idealization and hence the shock formation is not instantaneous but occurs over several tube diameters. Using a four-bladed knife edge to cut the diaphragm, four "petals" unfold in a finite amount of time** releasing a jet of driver gas

---

*A significant percentage of the helium driver gas would be ionized at this temperature and the ideal shock tube equations must be modified, but the order of magnitude of T_4 is unchanged.

**An estimate of the diaphragm opening time which places a lower limit on the time would be $t \geq (\rho \tau r/\Delta p)^{\frac{1}{2}}$ where ρ is the diaphragm density, τ is the diaphragm thickness, r is the effective test section radius, and Δp is the pressure jump across the diaphragm when it ruptures. For the diaphragm material used in this shock tube $t \geq 30$ μsec.

which eventually forms the front of the contact surface "zone". The disturbances introduced at the diaphragm and the effect of the finite shock formation distance can generally be neglected for observations made after ~ 20 diameters downstream of the diaphragm location (Ref. 8).

Boundary layer growth behind the shock wave and expansion fan causes shock wave curvature, flow irregularities, two-dimensional effects, and a limitation of test time (the time between the arrival of the shock and the contact surface). Following the experimental evidence of Duff (Ref. 9) and Glass and Patterson (Ref. 10), Roshko (Ref. 11) and Mirels (Ref. 12) developed a laminar boundary layer (LBL) theory capable of estimating the LBL effect on test time. This approach and the corresponding turbulent boundary layer (TBL) theory (Ref. 13) will be discussed more thoroughly in Section III and Appendix C. It suffices here to point out that the limiting test time (Fig. 16) assumes the form

$$\frac{\ell_m}{a_1 M_s} = \tau_m = \begin{cases} F_L(\gamma_1, M_s)\left[\dfrac{d\,\rho_1}{\mu_w}\right] \cdot d & \text{LBL} \\ F_T(\gamma_1, M_s)\left[\dfrac{d}{a_1^3}\dfrac{\rho_1}{\mu_w}\right]^{\frac{1}{4}} \cdot d & \text{TBL} \end{cases} \tag{5}$$

where d is the effective tube diameter, ρ_1 is the initial test gas density, a_1 is the test gas speed of sound, and μ_w is the viscosity of the gas behind the shock but at the wall temperature.

As an extension of the comparison between the HPD shock

tubes and a cryogenic tube it is convenient to express equation 5 with reference to room temperature conditions. Using helium gas, working at the same Mach number, and with the same test section diameter

$$\frac{\tau_{m_{cryo}}}{\tau_{m_{HPD}}} \sim \begin{cases} \left(\frac{T_o}{T_1}\right)^{1.6} & \text{LBL} \\ \left(\frac{T_o}{T_1}\right)^{.77} & \text{TBL} \end{cases} \qquad (6)$$

where the test gas is assumed to be perfect, T_w is assumed to equal T_1, T_o is room temperature, and the viscosity of the test gas is determined as $\mu_1 = \mu_o (T_1/T_o)^{.6}$. Equation 6 indicates that if the cryogenic tube has a test gas temperature T_1 of 3^oK and if the HPD tube operates with test gas at room temperature T_o, then the limiting test time for the cryogenic tube is more than three orders of magnitude larger than that for the HPD tube (if the boundary layers are laminar).

An important implication of equation 5 is that using a small diameter test section in a cryogenic shock tube acceptable test times can be obtained.

I. C. 3. Ideal Gas Behavior

At moderate temperatures and low pressures most gases behave like an ideal gas. Real gas effects (dissociation, ionization, radiation) become important at high temperatures; at low temperatures compressibility effects cause gas behavior to deviate from

ideal. For helium gas the temperature range of ideal gas behavior is larger than for any other gas. The temperature of helium gas is not high until it approaches 285,000°K (the ionization temperature, θ_i) and it is not low until it approaches 5.2°K (the critical temperature, T_c). If the temperature in any region of the shock tube is of the order of T_c or θ_i then the pressure of the gas in that region will determine the "idealness".

For an ideal shock tube using ideal gases (Fig. 1) it is possible to consider real gas effects in the light of a "worst case" analysis. Consider the limiting case when $p_4/p_1 \to \infty$ and $T_4/T_1 \gg 1$. In this limiting case the following approximations are accurate representations of flow quantities:

$$\begin{aligned} p_2/p_1 &\leq 20\ (T_4/T_1) \\ p_5/p_1 &\leq 120\ (T_4/T_1) \\ T_2 &\leq 5\ T_4 \\ T_5 &\leq 12\ T_4 \end{aligned} \tag{7}$$

Equation 7 indicates the dependence of flow quantities on the diaphragm temperature ratio. More important to the case of a cryogenic shock tube operated with $T_4 \sim 300°K$ is the limitation of gas temperatures behind both the incident and reflected shocks to less than 3600°K. The pressures in these flow regions are greater than 10^{-1} torr for cases of consideration. Under these conditions the degree of ionization is less than 10^{-14} for helium gas and consequently real gas effects can be completely negligible

for a cryogenic shock tube (Ref. 14).

Compressibility effects in a cryogenic shock tube are certainly of concern regarding the idealness of the gas into which the shock wave propagates. The parameter T_1/T_c can be less than 1 for the case of helium gas with liquid helium (LHe) as the cryogenic coolant. Consequently the pressure parameters p_1/p_c and $p_1/p_{s.v.}$ (p_c is the critical pressure, $p_{s.v.}$ is the saturated vapor pressure of helium gas at temperature T_1) play the major role in determining how valid an ideal gas approximation will be. For helium gas at $T_1 = 2.3^{\circ}K$ ($T_1/T_c = .44$) an analysis of the second virial coefficient* indicates that $p = \rho RT$ will be accurate to within 1% for $p_1 \leq p_{s.v.} = 47$ torr. Variation of helium speed of sound as p_1 approaches $p_{s.v.}$ indicates that the ideal gas relation $\sqrt{\gamma RT}$ is valid to within 1% for $p_1/p_{s.v.} \leq 0.5$.

As a further consideration of compressibility effects, it is necessary to consider condensation at the walls in flow regions 2 and 3. In these regions the pressure may be above $p_{s.v.}$ for certain run conditions and hence gas may condense at the walls. Since condensation at the walls is related to boundary layer effects it will be considered in Section III. It suffices here to point out that the extremely small heat capacity of the shock tube wall at cryogenic temperatures insures a relatively large wall temperature rise which prohibits gas condensation under certain conditions.

---

*Using a Lennard-Jones (6-12) potential and considering quantum mechanical effects (Ref. 15).

I. D. Previous Shock Tubes

To the author's knowledge there have been only two previous shock tubes working at cryogenic temperatures. (The tubes were developed independently.) In 1971 Yoder built the first such tube (Ref. 5) to look at low temperature shock waves in molecular hydrogen. In 1972 Rupert (Ref. 6) used a cryogenic shock tube to study experimentally the strengthening of a shock wave by a positive density gradient. The operating characteristics of these shock tubes were not extensively examined.

Yoder's tube was cooled using the gaseous boil-off from a cryogenic reservoir. Both driver and test sections were maintained at temperatures down to 30°K with LHe and down to 80°K with liquid nitrogen (LN_2). A limited number of runs were made using LHe as a coolant due to a very high cost per run. This resulted from the diaphragm changing apparatus which consisted of a plexiglass dry box built around the diaphragm location. This technique allowed for only 4 or 5 shots to be taken during a day. With LN_2 as a coolant, Yoder was able to adjust the shock tube temperature continuously over the range from 80°K up to room temperature. Using optical techniques he studied the Rankine-Hugoniot shock equation and rotational relaxation times for both normal hydrogen and parahydrogen.

The Rupert shock tube consisted of a vertically mounted tube with the test section partially immersed in a cryogenic bath. Shock waves formed in the room temperature region, entered the temperature gradient region, and then travelled through the

cryogenic temperature region. Using LHe (at 4.2^{o}K) or LN_2 (at 77^{o}K) as coolants the effects of gradient amplitude and width on shock strengthening were studied. Rupert concluded that even when the length scales of the three test section regions (room temperature, temperature gradient, cryogenic temperature) were comparable (each roughly 20 tube diameters) the shock strength approached the ideal case with a temperature jump across the diaphragm.

I. E. Goals of the Project

From the discussion of ideal shock tube theory and perfect gas behavior it is obvious that for certain run conditions a cryogenic shock tube can very accurately approximate an ideal shock tube. Very large Mach number shock waves can be produced with accurately known flow conditions in all shock tube regions.

The major goal of the project is to develop and test a prototype cryogenic shock tube capable of producing high Mach number shock waves and governed by ideal shock tube equations.

Of great importance to this effort is the need for diaphragm temperature ratios of 100 or larger. As an engineering problem, it is necessary to limit gas temperature gradients to an extent of not more than several tube diameters upstream and downstream of the diaphragm. Design criteria and constraints imposed upon this effort are as follows:

a) develop an efficient, fast, contamination-free diaphragm changing scheme

b) minimize cryogenic coolant boil-off so that the overall cost per run is minimized

c) utilize existing cryogenic dewars (i. e. the physical dimensions of the cryogenic system are fixed)

d) maximize the test section diameter so as to minimize boundary layer effects

e) maximize the test section length so that the test times are as long as possible

f) considering d) and e) together have the test section

length equal to at least 20 tube diameters so that the shock is well-formed and diaphragm opening effects are minimized.

Once developed, this shock tube is viewed as a prototype tool for the study of both fluid mechanic and cryogenic phenomena. At cryogenic temperatures gas kinematic viscosity is greatly reduced so that large Reynolds numbers are attainable. Studies of condensation, sublimation, evaporation, and critical point phenomena are also possible future applications. Quantum mechanical effects generally dominate at low temperatures, so the cryogenic shock tube may be a useful tool for experimental investigations. Finally, the rapid rise in pressure and temperature across a shock wave suggests the possibility of using the shock tube in the study of reaction rates, cryogenic materials, superconductors, and superfluid helium II (He II).

II. EXPERIMENTAL APPARATUS AND PROCEDURE*

II.A Shock Tube System

A schematic diagram of the device is shown in Figure 2. The shock tube consists of three stainless steel tubes: support tube, driver section, and test section. The driver and test tubes have a 1-inch inner diameter (ID) and the test section is 22 inches long. The axes of the tubes are arranged vertically with the test section at the lower end. The support section serves the dual functions of holding the test tube rigidly in place and housing the driver section.

The driver section is made of two concentric tubes (Fig. 3). A vacuum is drawn in the space between the tubes and radiation shielding is wrapped around the outside of each tube. In order to keep the driver section inner tube at $\sim 300^{\circ}K$ an electrical heating tape is wrapped around the outside of this tube and a small voltage drop is maintained across this tape.

A bellows and clamps arrangement permits the driver section to be displaced vertically while the entire shock tube is under vacuum or filled with test gas. This allows the diaphragm to be changed (driver section lifted off the test section) in a contaminant-free environment and then allows the unruptured diaphragm to be sealed into position above the knife edges (driver section clamped down onto the test section).

---

*A more detailed description of the apparatus and instrumentation may be found in Appendix B.

The diaphragm changing mechanism is the main design feature making the entire shock tube practical.* The diaphragm material is a 2-inch wide roll of 1/2-mil thick mylar. There is a direct analogy between this mechanism and the workings of a simple box camera. Starting from an output spindle the mylar runs vertically down the support tube, then between the driver and test sections, and finally up to a takeup spindle. This takeup spindle is attached to a room temperature region of the support tube and can be rotated manually from the outside. After a run the following sequence occurs:

a) the driver section is clamped in the "up" position

b) the takeup spindle is turned several times to pull a new portion of the mylar roll between the driver and driven sections

c) the test pressure is set

d) the driver is clamped in the "down" position

e) the driver is pumped out and then filled with driver gas until the diaphragm bursts.

By loading 20 feet of mylar roll onto the output spindle it is possible to run 70 shots during a day. Using LHe as the test section coolant, approximately 25 liters are required for a day of runs with a corresponding cost per run of about one dollar. The shock tube may be seen assembled and disassembled in Figures 4 and 5.

---

*This concept was suggested by Prof. D. Coles of this laboratory.

II. B. Cryogenic System

A large stainless steel dewar contains LN_2 for the case $T_1 = 77^{\circ}K$. For the other cryogenic cases this dewar provides an LN_2 bath in which the LHe dewar is immersed. The LHe dewar is a pyrex fully-silvered dewar provided with a large pump-out tube. A pyrex pipe flange allows a two-piece collar to mount the dewar under a stainless steel support plate. The pump-out tube is used to lower the bath temperature. (The dewars and collar are seen in Figure 6.)

The main cryogenic features specific to the shock tube are the O-rings which maintain pressure-vacuum seals in the cryogenic temperature regions. Indium solder is used in all such seals except the two O-rings that seal the diaphragm to the driver and test sections. Special cryogenic O-rings (teflon jacketed stainless steel cable springs) are used in these two vital sealing areas.

II. C. Instrumentation

With helium specified to be the driver and driven gas, it is possible to write the ideal shock velocity as

$$U_s = F\ (T_1,\ T_4/T_1\ ,\ p_4/p_1)$$

The instrumentation is designed to measure or infer all of these quantities so that a comparison to the ideal value can be made.

The cryogenic bath level is visually observed in the LN_2 cases but a level detector is used for the LHe cases. The detector is a standard design using carbon resistors and capable of determining whether liquid or vapor exists at discrete vertical positions.

The test pressure is monitored with an electronic manometer. Absolute accuracy with this gauge is roughly $\pm 2\%$ but repeatability of pressure settings (except for pressures $\leqslant 10^{-2}$ torr) is much better than this. A combination gauge is used to determine the driver gas burst pressure. With a "fast fill" technique this gauge reading is probably not better than $\pm$ 10% which is roughly the actual scatter in burst pressures over a day's runs.

The cryogenic bath temperature is determined from the saturated vapor pressure above the bath. A mercury barometer is used to determine ambient pressure when the bath is left open to the atmosphere. An electric manometer is employed for cases when the bath pressure is less than ambient. Based on vapor pressure temperature scales the largest error in absolute temperature is $\pm$ 1%. It is assumed that the test gas temperature is

equal to the bath temperature. This assumption has been verified for the LN_2 cases using a fine-wire thermocouple gauge.

Glass bead thermistors are used in the driver section (Fig. 3) to determine both the wall temperature (so that the heating tape current can be regulated) and the gas temperature. The gas thermistors are employed to infer the driver gas temperature as a function of time with an accuracy of ± 5%.

Platinum "thin film" heat transfer gauges are used in the determination of shock velocities and test times. The platinum films are baked onto a microscope glass slide. This is mounted on the test section end flange so that the length of the slide is parallel to the shock tube axis. The leading edge of the slide is sharpened to reduce interference effects. The tip film is used to trigger an oscilloscope which then records the arrival of the shock wave at two lower films. Current levels of 10^{-3} and 2×10^{-4} amps are used with the films. For three films this corresponds to a total power input of 10^{-3} and 4×10^{-5} watts respectively. (A schematic diagram of the glass slide film gauges and a typical oscillogram are shown in Figure 7.)

Distances between the films are measured very accurately (less than .2% error) on an optical comparator but arrival time errors vary from ± 1% to ± 4% depending on the time increment, signal-to-noise ratio, and signal rise time. Test time measurements are based on qualitative changes in the film voltage output and hence errors may be as large as 20%.

III. RESULTS AND DISCUSSION

Four cases were run in order to determine the performance characteristics of the cryogenic shock tube. Each case is defined by the test gas temperature T_1, and within each case only the test gas pressure is varied. The four cases are listed below:

a) $T_1 = 300^{\circ}K$ (room temperature)

b) $T_1 = 77.36 \pm .18^{\circ}K$ (LN_2 at 744 torr with a bath depth of 22 inches) referred to as $T_1 = 77^{\circ}K$

c) $T_1 = 4.196 \pm .004^{\circ}K$ (LHe at 744 torr with an average bath depth of 20 inches) referred to as $T_1 = 4.2^{\circ}K$

d) $T_1 = 2.287 \pm .023^{\circ}K$ (LHe at 47 torr with an average bath depth of 18 inches) referred to as $T_1 = 2.3^{\circ}K$

A few runs were made with $T_1 = 1.46^{\circ}K$ (LHe at 3 torr).

The test gas temperatures listed above represent the temperature of the cryogenic bath at half-depth (surface (-) and full-depth (+) temperatures are also given). To calculate the saturated vapor pressure at a given liquid depth the hydrostatic pressure is added to the surface pressure. The bath temperature is determined from the saturated vapor pressure using conversion tables (Ref. 16, 17).

III. A. Temperature Measurements

III. A.1. Test Gas Temperature

A chromel-constantan thermocouple is mounted near the test section wall roughly one diameter below the diaphragm location. The voltage output measures the temperature difference between the test gas inside the tube and the cryogenic bath (LN_2) outside. Based on a commercial calibration scale the sensitivity at this temperature is 26 μ volts/^{o}K. The noise level of 5 to 7 μ volts is continuously observed even while filling the driver section nearly to burst pressure. Checks are made over a range of test pressures. Only when the diaphragm actually ruptures does the voltage output increase (to several thousand μ volts).

The thermocouple data indicates that in the LN_2 cases the test gas (near the wall at one diameter below the "hot" driver section) remains at the cryogenic bath temperature until the shock wave passes. With LN_2 as a coolant it is inexpensive and easy to maintain the bath level above the top of the test section during the entire day's runs. However, the LHe cases present an entirely different set of problems: LHe is expensive; its density and its latent heat of vaporization are small. Consequently, to avoid excessive boil-off for the LHe cases the following procedure is used. Starting with the bath level at the top of the test section, runs are made until the level is roughly 5 to 6 diameters below the diaphragm location. The bath is then refilled and the procedure is repeated. Approximately 4 to 5 hours (20 to 25 shots) of run

time are possible between refills. The thermocouple temperature measurements are not made in the LHe cases due to the absence of any observed correlation between bath level and shock tube performance. Within the accuracy of the shock velocity measurements there is no difference between runs made with the bath level at the diaphragm and those made with the bath level 5 to 6 diameters below the diaphragm. Hence the width of test gas temperature gradient seems unimportant over distances comparable to the shock formation distance. This result is consistent with the conclusion drawn by Rupert (Ref. 6).

III. A. 2. Driver Gas Temperature

As indicated previously, the driver section is heated to help offset the heat loss resulting from clamping the driver down onto the "cold" test section. One wall thermistor (Fig. 3) is maintained at $\sim 330^{\circ}K$ by regulating the voltage across the heating tape. (This wall thermistor is located 5 diameters above the diaphragm location.) The resistances of the four gas thermistors are recorded as functions of time while the driver gas pressure is raised from vacuum to burst pressure. A commercial calibration scale is used to convert the resistances to temperatures. Thermistors 1, 2, 3, and 4 are arranged to be 0, 1/2, 1, and 1 1/2 diameters above the diaphragm.

III. A. 2. a. $T_1 = 300^{\circ}K$

For this case it is assumed that room temperature conditions apply initially in all regions of the shock tube (ambient

temperature in the lab is 297°K) and hence $T_4 = 300°K$.

III. A. 2. b. $T_1 = 77°K$

The results of four runs are seen in Figure 8. During each run a different gas thermistor resistance is recorded. The driver section is evacuated to 10^{-2} torr before adding driver gas; the flat portions of each curve indicate this time. Note that the steady state wall temperature gradient is followed during this period. The driver is brought up to burst pressure in roughly 1/4 of a second. The gas temperature appears to be spatially uniform and equal to 300°K at the time of diaphragm rupture. As seen in the figure the "hot" wall thermistor indicates a temperature of 325°K during these runs, so that the measured temperature rise seems quite reasonable. These results indicate that the glass bead thermistors are capable of fast time response in the turbulently mixing driver gas.

III. A. 2. c. $T_1 = 4.2°K$

Figure 9 shows similar data taken in a somewhat different manner. The temperature values for thermistors 2, 3, and 4 are recorded during a single run by using an analog channel selector (Ref. 18) to sequentially sample the three inputs. These thermistors indicate a gas temperature of 300°K while the lowest thermistor is at 284°K. Once again the driver section is filled with gas in 1/3 to 1/4 of a second.

III. A. 2. d. $\underline{T_1 = 2.3^{\circ}K}$

The results of measurements made for the $2.3^{\circ}K$ case are found in Figure 10. The data are taken during four runs as in the $77^{\circ}K$ case and the results are similar. An average temperature of approximately $300^{\circ}K$ is obtained in a fill time of 1/3 to 1/4 of a second.

III. B. Shock Wave Mach Number Measurements

The main effort involved in characterizing the performance of the shock tube is directed towards determining shock wave velocities. The observed shock velocity is used to compute the shock wave Mach number which is a figure of merit in high performance shock tubes. A comparison between observed and ideal shock velocities is made as one measure of the "idealness" of the cryogenic shock tube.

Helium gas is used both as a driver and test gas for all runs in all cases. The driver gas pressure is nearly constant within each case and hence the diaphragm pressure ratio is varied by changing the test gas pressure. All velocity measurements represent an average between two gauges (with the midpoint of the gauges located 21 diameters from the diaphragm). For most runs the separation distance between the gauges is 4 to 5 cm (with a measurement error of $\pm$ .1%). The difference in shock arrival time at the two gauges is measured on an oscillogram with an error between $\pm$ 1% and $\pm$ 4% (the error generally increases as the test pressure decreases).

Decreasing the power dissipated by the platinum film gauges (i.e., decreasing the current levels) has a negligible effect. To the accuracy of the measurements the observed shock velocities are unchanged. The voltage signals also appear to be qualitatively similar. Consequently any local heating of the test gas can be neglected.

Results for all cases are summarized in Table 1 and Figure 15.

III. B. 1. $T_1 = 300^{\circ}K$

The room temperature results are presented in Figure 11. Actual run data are used for this case. From these results it is important to note several things. The largest Mach number observed at room temperature is 2.4. The increasing departure from ideal values as the test pressure is decreased has been observed often before (e.g., Ref. 10) and has been explained on the basis of boundary layer effects (Ref. 11, 12, 13). The departure from ideal values for initial pressures of 5, 9, and 25 torr is similar to that observed by Duff (Ref. 9) using a test gas density equal to that in the 5 torr runs.

III. B. 2. $T_1 = 77^{\circ}K$

Results of the LN_2 coolant case are presented in Figure 12. The bars in the figure correspond to R.M.S. deviations. For this case the largest Mach number observed is 5.1*. From the figure it seems that boundary layer effects are negligible for test pressures greater than 9 torr when the shock wave has travelled 20 tube diameters.

III. B. 3. $T_1 = 4.2^{\circ}K$

Data for this test gas temperature are presented in Figure 13. From the figure it is apparent that the trends which were suggested by the $77^{\circ}K$ data are now more clearly defined. The shock velocity appears to be well predicted by ideal shock tube theory. Boundary

*For the $T_1 = 77^{\circ}K$ case the test gas pressure of .01 torr would imply a mean free path of ~ 4 mm compared to the tube diameter of 25.4 mm (consequently this one case may show the effects of shock thickness and curvature). The mean free path for all other cases is less than 1 mm.

layer effects are negligible over this length of test section until the test pressure is below .1 torr. The largest shock Mach number observed is 20.7.

The departure from ideal velocity at a test pressure of 5 torr appears to be real and is somewhat puzzling. The speed of sound at 5 torr is within .1% of the ideal gas value (Ref. 19). Compressibility effects (computed from the second virial coefficient using a Lennard-Jones (6-12) potential) on the ideal gas equation of state represent only a .02% deviation.

The possibility of shock wave-processed gas condensing at the test section walls will be considered in the discussion of boundary layer effects (Section III. C. 2). It should be noted that unless the gas actually condenses then LBL or TBL theory should fully account for any shock wave deceleration. Finally there is the possibility that the shock wave acceleration is not completed 20 diameters from the diaphragm for this highest pressure case. This seems unlikely in the light of room temperature shock formation evidence (Ref. 20) but cannot be completely ruled out in the cryogenic shock tube at this time.

III. B. 4. $T_1 = 2.3^{\circ}K$

Figure 14 presents the data collected from runs made with $T_1 = 2.3^{\circ}K$. This case represents the culmination of the trends which begin in the $77^{\circ}K$ case and extend through the $4.2^{\circ}K$ case (Fig. 15). The observed shock wave velocity is predicted to within 2% for all runs made at this temperature (except the highest test

pressure case). No boundary layer effects can be seen within the accuracy of the measurements. The highest shock wave Mach number observed is 32.2.

Arguments similar to those given for the highest pressure 4.2°K case can be made for the 3 torr runs in this case. The departure from ideal velocity is somewhat less at 2.3°K than at 4.2°K but the departure does seem to be real. The data from these two cases may support the explanation of shock wave acceleration in the high density cases (ρ_1 for these two cases is 8×10^{-5} gm/cm^3; at room temperature the pressure required to attain this density is 400 torr).

III. B. 5. $T_1 = 1.46^{\circ}K$

Four runs are made at this temperature with test pressures ranging from .01 - .0015 torr. The observed shock wave Mach numbers range from 36 to 40.

III. C. Shock Tube Test Times

As a further characterization of shock tube performance observed test times are compared to theoretically predicted values.

III. C. 1. Experimental Measurements

The experimental values are determined from the voltage history of the platinum film gauges. The film which is located along the leading edge of the glass slide (film #7 in Figure 7) acts somewhat like a stagnation gauge so a change in the slope of its voltage output can be used to determine the arrival time of the contact surface. For room temperature run conditions this arrival time can be clearly seen on the oscillograms, but for the cryogenic cases the change in voltage slope is much less dramatic. Consequently, the test time data taken from the cryogenic cases are to be considered only approximate. A stagnation wire was used for several cryogenic runs in an attempt to better define the contact surface arrival time but the results were no more satisfactory than with the films.

III. C. 2 Theoretical Predictions*

Three theoretical models are used to calculate test times: ideal, LBL, and TBL (Fig. 16). There are no adjustable parameters in any of these models, but after comparing the data to the original calculations it is apparent that the theories will have to be modified. The problem is that the test section is very short so

*A more detailed analysis may be found in Appendix C.

that the effects of the diaphragm opening process and finite shock wave formation distance can not be neglected. The theories are modified by assuming that an "effective" test section length (x_s) should be used in the calculations rather than the actual distance from the diaphragm to the gauges. From the observations of White (Ref. 20) it is expected that x_s will be a weak function of diaphragm pressure ratio and will probably differ from room temperature to cryogenic temperature since the diaphragm bursting process changes.

III. C. 2. a. Ideal Theory

From the ideal shock tube equations it is possible to derive the test time in the following form:

$$t_s = F(\gamma_1, M_s) \frac{x_s}{a_1}$$

where t_s is the test time seen by an observer who is a distance x_s from the diaphragm.

The shock wave Mach number M_s used in calculating the ideal test time is the observed Mach number rather than that predicted from the ideal shock tube equation.

III. C. 2. b. LBL and TBL Theory

Roshko (Ref. 11) and Mirels (Ref. 13) developed theoretical models to account for the change in test time due to the growth of a boundary layer behind the shock. The theory starts from an experimentally observed asymptotic state where the shock and contact surface are separated by a constant distance ℓ_m.

It is possible to write this maximum distance as

$$\ell_m = \begin{cases} F_L(\gamma_1, M_s)\left[\dfrac{\rho_1 a_1 d}{\mu_w}\right] \cdot d & \text{LBL} \\ F_T(\gamma_1, M_s)\left[\dfrac{\rho_1 a_1 d}{\mu_w}\right]^{\frac{1}{4}} \cdot d & \text{TBL} \end{cases}$$

A closed-form analytical solution can be obtained for both laminar and turbulent boundary layers by introducing similarity variables

$$X = \frac{x_s}{\eta\ \ell_m}$$

and

$$T = \frac{\ell}{\ell_m}$$

Theoretical consideration of the functions F_L and F_T leads to numerical solutions of boundary layer integrals. The final solutions agree with experimental data to an accuracy of ~ 10% (Ref. 12, 21).

As a rough guide Mirels states that LBL theory should apply when $dp_1 < .5$ and TBL theory should be used for $dp_1 > 5$ (d is the test section diameter in inches and p_1 is the test pressure in centimeters mercury). As seen from the expressions for ℓ_m a more relevant parameter is $dp_1\alpha$, where $\alpha = (\rho_1/\rho_o)\ (a_1/a_o)\ (\mu_o/\mu_1)$. The Mirels' criterion is modified for application to the cryogenic runs using helium gas:

$$dp_1\alpha = dp_1 \left(\frac{T_o}{T_1}\right)^{1.1} \begin{cases} < .5 & \text{LBL} \\ > 5 & \text{TBL} \end{cases}$$

where T_o is room temperature. This criterion is evaluated for the various cases in Table 2. It should be noted that boundary layer transition is a function of wall roughness and T_2/T_w. There is experimental evidence (Ref. 22) to indicate that for high Mach number shocks the increase in T_2/T_w acts to stabilize the LBL and inhibit transition. It has been demonstrated analytically that a decrease in viscosity from the external flow to the wall acts on the boundary layer in the same manner as a favorable pressure gradient (Ref. 23).

Observation of the voltage history of a platinum film gauge located in the middle of the glass slide (Fig. 7) indicates heat transfer characteristic of an LBL for the case p_1 = 1 torr and $T = 4.2^oK$ $(dp_1\alpha = 8)$. Since the shock tube walls are not honed the wall surface is rougher than the glass slide; it is possible that for this same case the wall boundary layer might become turbulent ahead of the contact surface.

III. C. 2. c. Wall Temperature Rise

The temperature of the shock tube wall is very important when considering test times for the 4.2^oK and the 2.3^oK cases. If the wall temperature rise is several degrees then the viscosity of the gas at the wall can increase by a factor of two. If the wall temperature rise is negligible then the gas behind the shock will condense at the walls for the larger test pressure cases. Either effect will decrease the test time.

Using an analysis based on the work of Sturtevant and Okamura (Ref. 24) it is possible to estimate the wall temperature rise for an LBL behind the shock wave. Assume that the gas everywhere is perfect, the Prandtl number is unity, $\rho\mu$ is constant through the boundary layer, and $M_s^2 \gg 1$. Then it can be shown that

$$T_w - T_1 \doteq (.3)\left(\frac{\rho_2 \mu_2}{\rho_s C_s k_s}\right)^{\frac{1}{2}} U_{shock}^2$$

The subscript s refers to the solid shock tube wall.

The results of this calculation can be seen in Table 3. Over the range of test pressures used the wall temperature is $\sim 8^\circ K$ for the $4.2^\circ K$ cases and $\sim 6^\circ K$ for the $2.3^\circ K$ cases. For the various runs the pressure behind the shock wave never exceeded 400 torr and hence it may be concluded that the gas never condensed at the test section walls (T_w would have to be less than $3.6^\circ K$ to condense at 400 torr). For a TBL the rise in wall temperature should have been even larger.

III. C. 3. Comparison of Theory and Measurements

Data and theoretical predictions for the four cases are seen in Figures 17 - 20. The theoretical curves represent a qualitative "best fit" to the data but due to the data scatter and small variation between LBL and TBL curves no general conclusions regarding the nature of the boundary layer will be made.

Figure 17 shows room temperature results with the somewhat surprising implication that the effective test section length is

roughly half of the actual length. It is not clear at the higher test pressures if the effective length is increasing or if the boundary layer is becoming turbulent. The Mirels' criterion indicates TBL test times for $p_1 \geq 50$ torr.

At cryogenic temperatures the effective test section length appears to be about 75 - 100% of the actual length. The effects of a rise in wall temperature for the $2.3^{\circ}K$ and $4.2^{\circ}K$ cases are considered in the LBL and TBL calculations.

Considering the shock tube performance on the basis of shock wave velocity measurements the tube appears to perform ideally at $2.3^{\circ}K$. As shown in Figure 20 the test time data for this case appear to be far from ideal if one x_s is used for all test pressures. However, test time data may be plotted on an ideal curve if x_s varies from 14 to 5 as p_1 varies from 3 torr to .003 torr. This means that is possible to fit the data on the boundary layer curves with a variable x_s so that the deviation from an ideal curve is small. White (Ref. 20) has observed an increase in shock formation distance (which corresponds to a decrease in effective shock tube length) with a decrease in pressure.

IV. CONCLUSIONS

A cryogenic shock tube capable of producing large Mach number shock waves has been developed. The shock tube performance with regard to shock velocity appears to be governed by ideal shock tube-perfect gas behavior. Observed test times are compared to ideal, LBL, and TBL predictions. Based on this prototype shock tube it appears that a larger cryogenic shock tube would be capable of producing high Mach number shock waves with long test times. The conditions in all flow regions can be accurately calculated on the basis of perfect gas behavior.

The development of this cryogenic shock tube as a practical and economical device leads to questions of modification and application. A cryogenic shock tunnel or a Ludwieg tube are possible extensions of the basic shock tube. Using a cryogenically cooled driver section it is possible to use the shock tube as a short duration wind tunnel with extremely large Reynolds number.

The cryogenic shock tube is essentially a tool which can be used to study fluid mechanic and cryogenic phenomena. Areas of possible further application and study are listed below:

a) large Mach number shock waves in ideal or real gases

b) large Reynolds number effects ($\mu \rightarrow 0$ as $T \rightarrow 0$)

c) phenomena involving the effects of C_p and $k \rightarrow 0$

d) boundary layer effects due to large ratios of external/wall temperatures

e) condensation, evaporation, sublimation, and critical point phenomena

f) quantum mechanical effects at low temperatures

g) use of the rapid increase in the pressure and temperature across the shock wave to study chemical reaction rates (e. g. frozen species which are heated with an inert gas shock), cryogenic materials, superconductors, or superfluid helium

The major conclusion of this effort is that working at cryogenic temperatures can be advantageous in a large number of experimental problems.

I. INTRODUCTION

Helium is the only substance that can exist as a liquid at 0° K. As the temperature of the liquid approaches 2° K helium experiences a λ-transition (Fig. 27) from helium I (LHe I) to helium II (LHe II). The unusual behavior of LHe II cannot be explained using the ideas of classical mechanics. At 1° K the deBroglie wavelength of a helium atom is of the order of the interatomic spacing. Consequently the behavior of LHe II is dominated by quantum mechanical effects.

London (Ref. 31) and Tisza (Ref. 32) viewed the λ-transition as the condensation of a degenerate Bose-Einstein gas. This approach provides a qualitative picture of LHe II being composed of a macroscopic proportion of ground state atoms. Landau (Refs. 33, 34) proposed a model which identified two forms of excitations which act as quasi-particles: phonons (sound quanta) and rotons. On the basis of the energy spectrum associated with these excitations Landau accurately predicted the thermodynamic functions of LHe II for temperatures below about 1.7° K. The concept of an additional form of excitation, the quantized vortex, was introduced by Onsager (Ref. 35) and Feynman (Ref. 36). The breakdown of superfluid properties or the onset of turbulence in the flow of LHe II is often explained using the ideas of quantized vorticity.

I. A. The Two-Fluid Theory

Below the λ-point helium behaves as if it were composed of two fluids. A two-fluid model has been proposed (Ref. 33) to explain the unusual properties of LHe II. This model assumes that the liquid is composed of a superfluid (subscript s) and a normal fluid (subscript n). The superfluid is an ideal, irrotational fluid: it carries no entropy and has no viscosity. The normal fluid is normal in the sense that it has viscosity and entropy. The two fluids are intermingling but noninteracting, i. e., the model assumes that below certain critical velocities the two fluids can move relative to one another without a transfer of momentum or energy.

I. A. 1. The Hydrodynamic Equations of LHe II

A development of the hydrodynamic equations of LHe II can be found in References 33 and 49. To begin, assume that:

$$\rho = \rho_s + \rho_n$$

and $$\vec{j} = \rho\vec{v} = \rho_s\vec{v}_s + \rho_n\vec{v}_n$$

That is, each infinitesimal volume of the liquid has associated with it two densities and velocities.

Neglecting dissipative processes the conservation of mass, momentum, and entropy can be written as:

MASS $$\frac{\partial \rho}{\partial t} + \vec{\nabla} \cdot \vec{j} = 0$$

MOMENTUM $$\frac{\partial \vec{j}}{\partial t} + \vec{\nabla} \cdot \vec{\vec{\pi}} = 0$$

ENTROPY $$\frac{\partial \rho s}{\partial t} + \vec{\nabla} \cdot (\rho s \vec{v}_n) = 0$$

where $$\vec{\vec{\pi}} = \rho_n \vec{v}_n \vec{v}_n + \rho_s \vec{v}_s \vec{v}_s + p \vec{\vec{I}}$$

($\vec{\vec{I}}$ is the identity tensor)

A fourth equation is required to close the system.* The superfluid is an ideal, irrotational fluid so that it is possible to write

$$\vec{\nabla} \times \vec{v}_s = 0$$

This means that $\vec{v}_s$ is the gradient of a scalar potential. It is possible to identify this potential as the chemical potential per unit mass Φ. Consequently the equation of motion for the superfluid can be written as:

SUPERFLUID MOTION $$\frac{\partial \vec{v}_s}{\partial t} + \vec{\nabla} (\tfrac{1}{2} v_s^2 + \Phi) = 0$$

This system of coupled, nonlinear equations is very complicated. The dependence of ρ, ρ_n, ρ_s, s, and Φ on the relative velocity $\vec{w} \equiv \vec{v}_n - \vec{v}_s$ makes the equations even more complex.

The boundary conditions at a solid surface require that the normal component of mass flux $\vec{j}$ vanish, the tangential component of $\vec{v}_n$ vanish, and the normal component of heat flux

*An equation of state is also necessary.

($\vec{q} = \rho s T \vec{v}_n$) be continuous.

I. A. 2. First and Second Sound*

The hydrodynamic equations can be linearized by assuming that $\vec{v}$ and $\vec{w}$ are small. This approach is accurate when considering small perturbations in ρ, p, T, and s about their equilibrium values. The linearized equations become

$$\frac{\partial \rho}{\partial t} + \vec{\nabla} \cdot \vec{j} = 0$$

$$\frac{\partial \vec{j}}{\partial t} + \vec{\nabla} p = 0$$

$$\frac{\partial \rho_s}{\partial t} + \rho s \vec{\nabla} \cdot \vec{v}_n = 0$$

$$\frac{\partial \vec{v}_s}{\partial t} + \vec{\nabla} \Phi = 0$$

Using thermodynamic identities for Φ and p these four equations reduce to two wave equations

$$\frac{\partial^2 \rho}{\partial t^2} = \nabla^2 p$$

$$\frac{\partial^2 s}{\partial t^2} = \left(\frac{\rho_s}{\rho_n} s^2\right) \nabla^2 T$$

Let ρ, p, s, and T be equal to their equilibrium values plus small fluctuating terms. If the fluctuations are proportional to $e^{-i\omega(t-x/C)}$ (where C is a wave speed) then the two equations

*A more detailed analysis may be found in Appendix D.

reduce to

$$C^4 - C^2 \left[\left(\frac{\partial p}{\partial \rho}\right)_s + \frac{\rho_s}{\rho_n} \frac{Ts^2}{C_v} \right] + \frac{\rho_s}{\rho_n} \frac{Ts^2}{C_v} \left(\frac{\partial p}{\partial \rho}\right)_T = 0$$

For LHe II $C_v \doteq C_p$ and it follows that $\left(\frac{\partial p}{\partial \rho}\right)_s \doteq \left(\frac{\partial p}{\partial \rho}\right)_T$. Denoting the specific heat by C_h, the two solutions for wave speed may be written as

$$C_{10} = \left(\frac{\partial p}{\partial \rho}\right)^{\frac{1}{2}}$$

$$C_{20} = \left(\frac{\rho_s}{\rho_n} \frac{Ts^2}{C_h}\right)^{\frac{1}{2}}$$

The first solution is the familiar acoustic speed and this wave propagation is called first sound. Second sound travels with the wave speed C_{20}. Since ρ_s vanishes at the λ-point the phenomenon of second sound does not occur above 2.172° K.

First sound can be identified as a density or pressure wave in which

$$\vec{v}_s = \vec{v}_n \left[1 + O(\alpha T)\right]$$

$$p - p_o \equiv \Delta p = \rho v C_{10} \left[1 + O(\alpha T)\right]$$

$$T - T_o \equiv \Delta T \doteq \frac{C_{10} v}{C_h} \left[\alpha T\right]$$

where $\alpha \equiv -\frac{1}{\rho} \frac{\partial \rho}{\partial T}$ is the expansion coefficient and the subscript o refers to equilibrium conditions. For LHe II below 2° K αT is $\sim -.01$. Consequently $\vec{v}_s \doteq \vec{v}_n \doteq \vec{v}$; the entire liquid moves as one fluid.

In a wave of second sound the entropy or temperature fluctuations are of the first order:

$$\vec{v}_s = - \frac{\rho_n}{\rho_s} \vec{v}_n \left[1 + O(\alpha T)\right]$$

$$\Delta T = \frac{\rho_n C_{20} w}{\rho s} \left[1 + O(\alpha T)\right]$$

$$\Delta p = \frac{-\rho_s C_{20} w s}{C_h} \left[\alpha T\right]$$

In a second sound wave the mass flux $\vec{j}$ and particle velocity $\vec{v}$ are approximately zero; the two fluids move in opposite directions.

I. A. 3. Finite Amplitude First and Second Sound Waves*

Khalatnikov (Refs. 37, 38) has determined the jump conditions across both pressure and temperature discontinuities in LHe II by considering terms of order w^2 in the hydrodynamic equations. The analysis is restricted to wave propagation with no dissipative losses.

For a pressure discontinuity it can be shown that:

$$C_1 = C_{10} \left[1 + \frac{\Delta p}{2} \frac{\partial}{\partial p} \ell n \, (\rho C_{10})\right]$$

$$v = \frac{\Delta p}{\rho C_1}$$

$$\frac{C_h \Delta T}{C_{10}^2} = O\left[\frac{\Delta p}{\rho C_{10}^2}\right]^3$$

and $$\frac{w}{C_{10}} = O\left[\frac{\Delta p}{\rho C_{10}^2}\right]^3$$

*A more detailed analysis may be found in Appendix D.

As seen in Figures 28 and 29, ρ and C_{10} are not weak functions of p. Consequently C_1/C_{10} can be significantly larger than 1 for a Δp of several atmospheres.

For a temperature discontinuity it is possible to find:

$$C_2 = C_{20}\left[1 + \frac{\Delta T}{2}\,\frac{\partial}{\partial T}\,\ell n\left(C_{20}^{\,3}\,\frac{\partial s}{\partial T}\right)\right]$$

$$w = \left[\frac{\rho}{\rho_n}\,\frac{s}{C_{20}}\right]\Delta T$$

$$\frac{\Delta p}{\rho C_{20}^2} = O\left[\frac{w}{C_{20}}\right]^2$$

$$\frac{C_{10}{}^v}{C_{20}^2} = O\left[\frac{w}{C_{20}}\right]^2$$

The analysis of Khalatnikov indicates that the nonlinear behavior of both first and second sound waves can cause wave steepening. As in an ordinary liquid or gas only a compression first sound wave will steepen into a discontinuity or shock wave. However, due to a change in sign of $\frac{\partial C_{20}}{\partial T}$ it is possible for a decrease in temperature to propagate as a second sound shock wave. This means that the front edge of a negative temperature pulse and the back edge of a positive temperature pulse will steepen. *

*Consequently the front edge of a positive temperature pulse will disperse.

I. B. Previous Experimental Studies of Finite Amplitude Waves in LHe II

In 1950 Osborne (Ref. 39) experimentally studied "second sound shock waves." This work was essentially qualitative, but many of the features of finite amplitude second sound waves were established. Osborne used an electrical pulse through a fine wire to generate the second sound waves. A maximum heat input of 3.6 watts/cm^2 was used.

Dessler and Fairbank (Ref. 40) in 1956 established the validity of Khalatnikov's analysis for values of $\frac{w}{C_{20}} \lesssim 10^{-2}$. An aluminum film evaporated on a plate glass was used as a pulsed heater. A small amplitude mark pulse was transmitted alone and then superimposed on a larger amplitude carrier pulse. The change in second sound velocity with amplitude was determined by comparing the time of flight of the small pulse with and without the carrier pulse. A maximum heat flux of 1.6 watts/cm^2 was used for the carrier pulse.

Gulyaev (Refs. 41, 42) published experimental results of optical studies of large amplitude second sound in 1969 and 1970. Using a Schlieren (Toepler method) system he was able to detect both first and second sound waves. The geometry of the heater was somewhat unusual, consisting of .47 mm-wide constantan ribbons spaced 1 mm apart. With electrical pulse amplitudes as large as 19 watts/cm^2 (9 watts/cm^2 in two directions) Gulyaev was able to investigate boiling of the LHe at the surface of the ribbons and the interaction of first and second sound waves at a

vapor-liquid interface.

To the author's knowledge there has been no experimental work on finite amplitude first sound waves in LHe I or LHe II.

I. C. Goals of the Present Investigation

The present experiment involves the reflection of a gas-dynamic shock wave from liquid helium (LHe in equilibrium with its vapor represents a very simple two-phase system). Consider a Mach 10 shock wave propagating through the vapor with initial pressure 3 torr and temperature 1.46° K. The shock reflects from the LHe surface in a time of the order of 3 nanoseconds ; it raises the pressure to 3 atmospheres and the gas temperature to 120° K. Since LHe is very compressible this pressure jump creates a first sound shock which moves 7% faster than the acoustic speed and a liquid particle velocity of 10 m/sec. The sudden increase in gas temperature causes surface boiling and generates a large amplitude second sound wave (second sound shock).

In the light of the above considerations the goals of the present investigation are as follows:

a) check the validity of the first order terms in Khalatnikov's analysis of the pressure discontinuity in both LHe I and LHe II.

b) examine the nature of second sound shock waves generated from the liquid surface

c) study the interaction of finite amplitude first and second sound waves (travelling in the opposite or the same direction)

d) determine the magnitude of the second sound wave which is coupled to the first sound shock

e) if possible, determine the effect of surface evaporation (mass source) on the reflected gasdynamic shock wave.

In sum, this experiment is designed to test the hydrodynamic two-fluid model with large gradients in temperature and pressure.

II. EXPERIMENTAL APPARATUS AND PROCEDURE

II. A. Shock Tube and Cryogenic Systems

The shock tube (Figs. 2-5) and cryogenic system (Fig. 6) have been previously described in Part I and Appendix B. The only change in the shock tube concerns a problem with diaphragm petals falling into the test section. After 30-40 runs there are 2-6 petals or petal pieces on the test section end wall; to eliminate these a conically shaped screen (vertex up) was soldered below the knife edges. Some of the data are taken with this screen installed, some without: no difference is observed.

LHe condenses at the bottom of the test section (to a depth of roughly 1 inch) by admitting helium gas to the shock tube. The gas condenses until its pressure matches the vapor pressure of the LHe in the cryogenic bath (temperature equilibrium). The shock tube run procedure is the same as given in Part I except the test pressure is regulated by controlling the bath temperature.

II. B. Instrumentation

The test section pressure is measured using a Barocel Electronic Manometer. With LHe inside the shock tube the manometer also provides a measure of the bath temperature. This vapor pressure-temperature is compared to the resistance-temperature of an Allen Bradley carbon resistor located within the bath to insure repeatability of the run conditions.

As in the development work on the shock tube a combination gauge measures the driver gas pressure. A wall thermistor and heating tape are used to maintain the driver gas at room temperature.

Two types of instrumented false-endwalls (Fig. 32) are used on the stainless steel end flange. The gas detectors use carbon card (500 ohms per square) as the detecting element while the liquid detectors employ flakes of an Allen Bradley carbon resistor (10 ohms; 1/2 watt) as the sensitive elements. Both kinds of elements are sanded to a thickness of less than 10 mils.

As indicated in Figure 33 the detectors are made by coating the copper rods with epoxy. The detecting elements are epoxied into position and then the rod is sanded smooth. Silver conducting paint is used to provide electrical contact from the detector to the copper rod and copper wire. The rods are about 70 mils in diameter so that they occupy less than 2% of the cross section of the shock tube.

The rods are epoxied into the lucite disc which then fits inside the shock tube with a diameter clearance of 20 mils.

Both types of liquid detectors have their sensitive elements less than one inch above the lucite while the gas detectors are located from 1 1/4 to 2 1/4 inches above the endwall. The same gas detectors are used with both endwalls.

A constant current of 10^{-4} amps is maintained across each detector. The power dissipated is 10^{-5} watts corresponding to a heat load of 10^{-3} watts/cm^2. The sensitivity of the liquid detectors (determined from a static calibration) is approximately .1 volt/°K from 1.46°K to 2.1°K. When exposed to the gas-dynamic shock wave the liquid detectors show a rise time of 5-10 μsec indicating a frequency response of approximately 20 khz. The liquid detectors are capable of sensing the passage of the first sound shock by responding to the change in pressure and temperature.

The location of the detectors with respect to the lucite endwalls is measured using an optical comparator (top mounted detectors) or a machinist's microscope (side mounted detectors). Both of these instruments use micrometer driven tables which are capable of determining the position in 10^{-4} inch increments. Repeatability of the measurements implies a position error with respect to the endwall of less than .3%.

Most of the data were taken using the top mounted liquid detectors. In this way no wall or boundary layer effects obscure the incident first and second sound signals. Also the signal levels are much larger when the wave reflects from the detector. If the detector surface is normal to the wave vector then the

position of the detector is known very accurately and the wave rise time is not smeared by a finite extent of detector surface.

To accurately measure wave velocities and arrival times the top mounted detectors depend critically on the shock wave reflecting off a plane liquid surface. The scatter in the data taken using these detectors indicates that the liquid surface is not absolutely plane over the cross section of the shock tube. The side mounted liquid detectors eliminate the critical dependence on a plane surface and consequently greatly reduce the data scatter. Decreased signal level and increased rise time are the main disadvantages to these detectors.

II. C. Calibration Cell

A calibration cell (Fig. 34) has been constructed for the purpose of dynamically calibrating the top mounted liquid detectors. The cell is a model of the shock tube test section with an electrical second sound emitter in place of the free surface. This emitter consists of a gold film (roughly 100 Å thick) evaporated onto a glass slide. A one-inch square of this film has a resistance of 26 ohms at 300° K and 24 ohms below 100° K. An electronic pulse generator is used to heat the emitter with a Heavyside voltage pulse of adjustable amplitude and duration.

Instrumented endwall #1 sits on the cell end flange just as in the shock tube. The distance between the top mounted detectors and the emitter is adjusted by using spacers with the end flange. The entire cell is immersed in an LHe bath for calibrating. Temperature equilibrium is assured by holes drilled into the cell wall below the level of the detectors.

The cell is intended to provide a dynamic calibration of the received second sound signals. The detectors are set up exactly as with the shock tube; the same amplifiers and oscilloscope are used to record the second sound data. Electrically heated emitters are standard second sound sources and it is possible to relate the detector signal amplitude to a theoretically calculated temperature jump. These voltage calibrations can then be applied to the shock wave generated signals (neglecting the effect of increased pressure) in order to estimate the corresponding temperature jumps.

II. D. Data Reduction

The voltage outputs of the gas and liquid detectors are recorded on oscillograms. Typically, one oscilloscope is used to record the incident and reflected gas shock arrival time at two gas detectors. Another oscilloscope records the first sound signals and a third scope records the second sound signals from the two liquid detectors.

Arrival time data are taken from the oscillograms using cross hairs which are moved with a voltage dividing circuit. The times are recorded as voltages on digital tape. These voltages are converted back into times using a computer program which also corrects for time sweep errors.

III. RESULTS AND DISCUSSION

Before attempting to reflect a shock wave off LHe a simpler experiment was run at room temperature. A lucite test section was bolted onto the shock tube in place of the stainless steel section. Water with red dye was poured into the test section to a depth of one inch. Shock waves were reflected from the water surface (the test pressure was 30-50 torr).

A pair of sidewall heat transfer gauges were used to monitor the incident and reflected shocks. Shadowgraphs of the reflected shock wave and liquid-gas interface were taken in order to determine if an interface instability could be detected. No instability (waves or splashing) was observed, but water vapor did condense on the test section walls after each run.

For the runs with LHe in the test section two parameters are varied: the test gas pressure (the gas-liquid temperature is dependent on this pressure) and the liquid depth. Helium gas at $\sim 300^{\circ}K$ and 30-35 psia is used as the driver gas for all runs. One LHe I case is run:

$$P_1 = P_{s.v.} = 47 \text{ torr } (2.26^{\circ}K)$$

Four LHe II cases are run:

$$P_1 = P_{s.v.} = 25 \text{ torr } (2.02^{\circ}K)$$

$$P_1 = P_{s.v.} = 18 \text{ torr } (1.91^{\circ}K)$$

$$P_1 = P_{s.v.} = 9 \text{ torr } (1.71^{\circ}K)$$

$$P_1 = P_{s.v.} = 3 \text{ torr } (1.46^{\circ}K)$$

III. A. Wave Diagrams

A wave diagram is a graph of distance versus time. The trajectory of a wave is represented by a curve on the graph. Using the instrumented endwalls it is possible to construct a wave diagram for each run. The known position of each detector defines its "distance"; its "time" is determined from the oscillogram arrival times. Typical oscillograms which show the arrival of the incident and reflected shock, first sound waves, and second sound waves are seen in Figures 35, 36, and 37 respectively.

III. A. 1. x-t Diagrams and Calculation of the LHe Depth

If all waves are plane and if acceleration or deceleration of the waves can be neglected (for the times of interest to this problem), then each wave trajectory can be represented by a straight line (Fig. 38). Two data values on each wave line define that line for the run.

The liquid depth L and the arrival time of the shock wave at the liquid surface T are calculated from the intersection of the incident and reflected shock wave lines (see Fig. 38). These L and T values are compared to those calculated from the incident shock-first sound (and incident shock-second sound) line intersections. For most runs the liquid level is determined to within $\pm$ 1 mm. This is more accurate than most nonvisual techniques (Ref. 43, 44). The side mounted detectors determine L to $\pm$.5 mm.

III. A. 2. χ-τ Diagrams

In order to present all the data from one test pressure case on a single wave diagram it is necessary to use similarity parameters. Let

$$\chi \equiv \frac{L-x}{L}$$

and

$$\tau \equiv \frac{t-T}{L}$$

where L and T for each run are computed as indicated previously. In the χ-τ plane $\chi=0$ represents the initial liquid-gas interface, $\chi = +1$ represents the lucite end wall, $\tau < 0$ refers to time before the shock reflects from the liquid, and $\tau > 0$ to time after the reflection. Note that while χ is dimensionless, τ has the dimensions of inverse velocity (μsec/cm).

χ-τ diagrams for all of the cases are seen in Figures 39-44. For the LHe I case the liquid detectors are used to record the incident, reflected, and rereflected first sound waves. In the LHe II cases these detectors monitor the incident first and second sound waves (the apparent arrival of the liquid-gas interface is shown for several runs using the side mounted detectors). For p_1 = 25 torr (Fig. 40) the second sound signals are difficult to detect due to the low wave speed, small signal level, and long signal rise time - consequently no data can be shown with confidence.

III. A. 3. Theoretical Analysis of the χ-τ Diagrams*

All wave lines shown in the χ-τ diagrams are based on theoretical computations (except the incident shock lines which are used as input for these computations). The assumptions used in this analysis are as follows:

a) the problem is one-dimensional

b) the gas is ideal in all flow regions

c) the LHe behavior is described by the two-fluid hydrodynamic equations

d) the first and second sound waves are uncoupled and do not interact

e) changes in the liquid temperature are neglected

f) all dissipative mechanisms are neglected

g) surface evaporation effects are neglected

The first sound waves are calculated using Khalatnikov's finite amplitude theory. The velocities of second sound waves are those of infinitesimal amplitude, corrected for the region pressure (see Fig. 30), and added as vectors to the region particle velocity. Results of the calculations are presented in Table 6 where the notation of Figure 38 is used (subscripts refer to flow regions).

Some of the restrictions of this analysis can be relaxed without much complication to the calculations. However, it is the function of the χ-τ diagrams to aid in determining which neglected effects are important. For example, if the reflected shock wave is strengthened due to surface evaporation, then this may be

* A more detailed analysis may be found in Appendix E.

clear from the diagrams.

For those cases with sufficient data a first order polynomial has been fit to the (χ, τ) values using a least-squares scheme. The coslopes of the lines are the observed wave velocities. These observed velocities are compared to the theoretical values in Tables 5 and 7. The tables also contain values of the τ axis intercepts and R.M.S. τ deviations of the data from the lines.

III. B. The Gas Flow Field

III. B. 1. The Incident Shock Wave

The assumption that the gas behaves as an ideal gas is certainly valid once the incident shock wave passes. The flow variables in region 2 are calculated using the ideal gas-shock tube relations; however, since the gas in region 1 is helium vapor there is some error in these computations. As seen in Table 5 the incident shock velocity is 82-92% of that predicted using the ideal shock tube equation. This may be due to the finite shock wave formation distance since this trend was observed in Part I of this work using a large density (ideal) test gas.

It is difficult to find information regarding the equation of state and velocity of sound for helium gas below 2°K. The shock tube cases cover the range $.28 \leq T_1/T_c \leq .44$ with $.0016 \leq p_1/p_c = p_{s.v.}/p_c \leq .025$. Extrapolating calculations* of the second virial coefficient using a Lennard-Jones (6-12) potential (Ref. 15) it is possible to estimate that

$$1.001 \leq \frac{p}{\rho R T} \leq 1.006$$

for $1.46°K \leq T_1 \leq 2.26°K$

with $3 \text{ torr} \leq p_1 = p_{s.v.} \leq 47 \text{ torr}$

Consequently the equation of state differs little from that of an ideal gas.

---

* Based on a quantum mechanical analysis.

The velocity of sound in helium vapor has been measured by Van Itterbeek and De Laet (Ref. 45). The speed is 15.7% below the ideal gas value at 4.23°K, 2.6% below at 2.26°K, and 2.5% below at 2.08°K. Using the ideal gas speed of sound below 2°K may result in an error in M_s of -2%. Consequently the calculated pressure and temperature in region 2 may be ~ 4% low.

An interesting aspect of the experimental problem is the existence of an LHe film (roughly 200 Å thick) on the shock tube walls. This film will begin to evaporate with the passage of the incident shock wave. Consequently the film acts as a mass source at the wall. This effect is opposite that of the boundary layer and will tend to lengthen the test time.

III. B. 2. The Reflected Shock Wave

The reflected shock wave travels at a velocity which is ~ 15% larger than that calculated from the observed M_s * (see Table 7). This may be due to the mass source effect of evaporation at the LHe surface. U_R could also be larger than expected if T_2 or a_2 is larger than that calculated using M_s. This latter explanation requires an error in the calculated T_2 which is an order of magnitude too large.

Mass addition due to evaporation at the LHe surface is similar to the mass deletion effect of a thermal layer. When a shock wave reflects from a "cold" endwall the increased gas density at the wall acts like a receding piston and slows the reflected shock

* U_R is even larger than the ideal value with $u_5 \equiv 0$.

wave. This effect decays as $(t-T)^{-\frac{1}{2}}$. Sturtevant and Slachmuylders (Ref. 46) find that when $R = U_R^2(t-T)/K_5$ is of the order of 10^3, the velocity of the reflected shock has returned to 96% of the ideal value. For the cases considered here $R = 10^3$ when $t-T \doteq .1$ microsecond.

The surface evaporation effect is not simple to estimate and it is possible that the time scale for increased reflected shock velocity is much larger than .1 microsecond. An idealized calculation of the liquid-gas interface temperature yields values from 8°K to 20°K (the critical temperature is 5.2°K) for the present cases. The pressure behind the reflected shock is always larger than the critical pressure. Consequently the surface must evaporate or "change phase"* as the liquid and gas try to return to an equilibrium state.

Assume that all the heat which diffuses from the gas into the liquid in the time t-T is used to evaporate liquid. Then the evaporated atoms act as an advancing piston with a velocity equal to: 10^3 m/sec for $t-T=10^{-8}$ second; 10^2 m/sec for $t-T = 10^{-6}$ second; 10 m/sec for $t-T=10^{-4}$ second. On the χ-τ diagrams $t-T= 10^{-4}$ second corresponds to $\tau \sim 40$ and hence the shock trajectory should show curvature by this value if the evaporation rate has dropped significantly. Despite the data scatter no curvature is evident for any of the cases (fitting higher order polynomials to the data do not significantly reduce the R.M.S. τ deviations).

---

* Above the critical point the substance can change from liquid-like to gas-like without a latent heat (see Fig. 31).

III. B. 3. The Transmitted Shock Wave

A shock wave is transmitted to the gas when the first sound wave reflects off the liquid-gas interface (Fig. 38). The velocity jump across this wave, $u_5 + u_9$, is small compared to the speed of sound in region 5. Consequently this shock is very weak and is not observed using gas detectors (see Fig. 35).

IIIB. 4. The Contact Surface Arrival

The arrival of the contact surface can be seen in the diagrams only for the p_1 = 3 torr case (Figs. 43, 44). The contact surface-reflected shock interaction produces an expansion fan travelling into region 5. Once the expansion fan reflects from the liquid-gas interface the χ-τ diagram will be modified. The expansion wave is weak and hence the modifications are not large. No experimental data have been taken for this expansion fan.

III. C. The Liquid Flow Field

The mean free path of the test gas varies from 1.8×10^{-6} to 1.8×10^{-5} cm as p_1 varies from 47 to 3 torr. For a shock wave which is ~ 10 mean free paths thick the time of reflection off the liquid surface varies from 1 to 3 nanoseconds. In terms of estimating the liquid behavior for times greater than 30 nanoseconds after the reflection it is reasonable to assume that the gas instantaneously changed from thermodynamic state 1 to state 5. The rise times of the incident first and second sound waves should be very short initially.

A comparison of calculated and observed velocities is seen in Table 7. The scatter in second sound data makes it difficult to draw conclusions about the wave speed.

III. C. 1. First Sound Waves

The observed first sound speeds are 2-7% greater than those calculated using the observed U_s values and 2-6% greater than those calculated using the observed U_R values. The reason for this discrepancy is not clear. There may be higher order or neglected terms in Khalatnikov's equation for C_1 which should be considered. It may also be that the effects of surface evaporation provide an initial pressure pulse which is larger than that inferred from the U_R data. A set of piezoelectric transducers should be used to more accurately determine the first sound arrival time and pressure jump.

Note that for a plane wave travelling through a liquid the observed Mach numbers $M_1 = C_1/C_{10}$ are very large (M_1 varies from 1.10 to 1.16). Equivalent strength waves in water require pressure jumps of 1-2 kilobars (Ref. 47).

The first sound wave reflects off the lucite end wall and travels back through the liquid. This reflected first sound wave is a shock wave which further compresses the liquid ($p_7 > 2p_5$). When this wave reaches the liquid surface a rereflected expansion fan travels back into the liquid reducing the liquid pressure. A weak shock wave is transmitted into the gas increasing the gas pressure. The reflected and rereflected first sound waves can be readily observed in the LHe I case (see Fig. 36). The χ-τ diagram for this case (Fig. 39) shows a qualitative agreement with the theoretical wave lines.

Examination of the pressure-temperature diagram of helium shows that the λ-temperature separating LHe I from LHe II decreases as the pressure increases. This suggests an interesting experiment in the shock tube. Can LHe II be converted to LHe I by the reflected first sound wave (see Figs. 27 and 31) and then be converted back into LHe II by the rereflected wave? The cryogenic shock tube is ideal for experiments designed to test the nonsteady and nonlinear terms in the two-fluid equations.

III. C. 2. Second Sound Waves

For purposes of data comparison the second sound velocities used in the χ-τ diagrams and Table 7 are computed as follows.

The pressure and particle velocity in a region are calculated from the first sound equations. The small amplitude second sound velocity for that pressure (Fig. 30) is then added as a vector to the particle velocity. Hence

$$C_2(6) = C_{20}(p_6, T_o) + v_6$$

$$C_2(7) = C_{20}(p_7, T_o)$$

and $$C_2(8) = C_{20}(p_8, T_o) - v_8 \quad .$$

It is possible to compare the observed data to these wave lines in order to determine if the observed wave is moving faster or slower* than the small amplitude wave.

The results in Table 7 indicate two trends which may be significant. A line through the incident second sound data from the top mounted detectors indicates a high velocity and a positive τ axis intercept. Although the numbers may be in error due to the data scatter these two factors indicate a strong wave which is delayed at the surface. The side mounted detectors are in better agreement with the computed lines. Consequently the detector geometry may play an important role (through an interference effect) in the mass or heat flows.

No reliable data can be presented for the $p_1 = 25$ torr case. The signal-to-noise ratio and the wave speed are smallest for this case while the rise time of the wave front is largest.

---

* For temperatures above 1.9°K the second sound shock front should disperse as the wave travels through the liquid.

III. C. 3. Interactions Between First and Second Sound

In plotting the small amplitude second sound lines in flow regions 7 and 8 it is implied that only transmitted waves will exit the first sound-second sound interaction. The possibility of reflected waves is considered by Dessler (Ref. 48). Another approach is taken in Appendix E of this paper. Assume that the first sound wave is not affected by the interaction. If for the second sound waves:

a) the total heat of the incident (I) wave is conserved by the reflected (R) and transmitted (T) waves

b) the heat flux is conserved

then for colliding waves it can be shown that

$$\Delta T_R \doteq (\tfrac{1}{2} \frac{v}{C_2}) \Delta T_I$$

and

$$\Delta T_T \doteq (1 + \tfrac{1}{2} \frac{v}{C_2}) \Delta T$$

Here v is the change in particle velocity across the first sound wave and ΔT is the temperature change across a second sound wave.

For the present cases $v/c_2 \doteq \frac{1}{2}$ and consequently $\Delta T_R \doteq \frac{1}{4} \Delta T_I$. Experimental evidence for the existence of a reflected wave of this strength is inconclusive. For some runs the top mounted detectors indicate a secondary wave but the scatter from these detectors is too large to draw any conclusions. The side

mounted detectors have a much smaller signal level and a longer rise time making it difficult to interpret signals arriving after the incident wave.

III. C. 4. Coupling of First and Second Sound

If the expansion coefficient for LHe is identically equal to zero the two wave forms will nevertheless be coupled. For a large amplitude first sound wave it can be shown that

$$\frac{C_h \Delta T}{C_{10}^2} = O\left(\frac{\Delta p}{\rho C_{10}^2}\right)^3$$

or

$$\Delta T \doteq \frac{v^3}{C_{10} C_h}$$

For all the cases which have been run in the shock tube this temperature change is of the order of 1×10^{-3} °K.

Since the expansion coefficient for LHe has a finite value there is also a temperature change across the first sound wave due to the expansion coefficient $\alpha = -\frac{1}{\rho}\frac{\partial \rho}{\partial T}$. The magnitude of this temperature jump can be expressed as (Ref. 49):

$$\Delta T = \frac{\alpha T v C_1^3}{C_h (C_1^2 - C_2^2)}$$

or

$$\Delta T \doteq \frac{\alpha T}{C_h} C_1 v$$

This value is -8×10^{-3}°K for the $T_1 = 1.46$°K case, -15×10^{-3}°K for the 2.02°K case, and $+53 \times 10^{-3}$°K for the 2.26°K case.

The total change in temperature is expected to be roughly -10×10^{-3}°K for LHe II and $+55 \times 10^{-3}$°K for LHe I. Typical oscillograms for first sound data are seen in Figure 36. Signals from the top mounted detectors are negative voltages both above and below the λ-temperature. This indicates a decrease in the electrical resistance of the detecting element. In terms of temperature change this indicates a temperature rise. The carbon detecting elements do respond to pressure changes such that the resistance decreases with increasing pressure.

In Figure 36 note the following: for LHe I the incident and reflected waves produce negative voltage changes* while the rereflected wave is identified by a positive voltage change; in LHe II the incident wave signals are negative but much smaller in amplitude. This indicates that the pressure jump across the incident first sound wave produces a negative voltage change. Added to this is a positive or negative voltage change corresponding to the temperature jump.

The resistance and temperature sensitivity of the detectors increase with decreasing temperature. The Joule heat of the detectors is dissipated by different mechanisms in LHe I and LHe II. Consequently the magnitude of a first sound voltage change is difficult to interpret in terms of a quantitative temperature jump.

---

* One of the side mounted detectors in Figure 36 indicates a positive voltage change (corresponding to the arrival of the incident first sound wave), but this is probably due to a poor electrical contact.

There have been several experiments which have measured the coupling terms in small amplitude first and second sound waves (Refs. 50, 51, 52). Some of the results do not agree with one another or with the theoretical predictions. In large amplitude first and second sound waves the coupling terms are much larger in absolute magnitude. With more sensitive detectors in the shock tube it should be possible to measure the amplitude of the coupled temperature and pressure jumps.

III. D. Detector Calibration and Calibration Cell Results

The top mounted detectors are calibrated both statically and dynamically. A thermal boundary resistance or Kapitza resistance exists at an LHe II - solid interface (Ref. 53). This can lead to an order of magnitude error in temperature measurement if only the static calibration is considered in a dynamic situation.

The static calibration is obtained using instrumented endwall #1 in the shock tube and also in the calibration cell. The detectors are fully immersed in LHe and the detector currents are turned on so that the output voltage can be recorded digitally. Starting at 1.4°K the LHe bath temperature is allowed to slowly rise to the λ-temperature (2.172°K). A curve of voltage versus temperature is then constructed for each detector. The slopes are nearly constant with values of -.12 volt/°K for the three detectors.

These voltages are amplified by a factor of 10^3 when displayed on an oscillogram. Consequently the static calibration indicates a temperature rise of $\sim 4 \times 10^{-3}$°K for a voltage jump of -.5 volt (this is the maximum voltage change observed in the shock tube; see Fig. 37).

Instrumented endwall #1 (with the gas detector rod removed) is installed in the calibration cell for the dynamic calibration (Fig. 34). The cell is immersed in a bath of LHe. This arrangement simulates the geometry of the shock tube except that the free surface is replaced with a second sound emitter. This device permits some interesting experimentation in addition to the dynamic calibration.

An electrical pulse is converted to heat by the emitter. The amplitude (heat flux) and duration of this pulse and the bath temperature can be varied independently. Three surveys have been taken using this cell:

a) the pulse duration is varied from 3 to 300 microseconds

b) the bath temperature is varied from 1.46°K to 2.26°K

c) the pulse amplitude is varied from .57 to 15.6 watts/cm^2

The distance from the emitter to the detectors can also be changed if the calibration cell is removed from the bath. Most of the data have been taken with the detectors located 2.3 - 7.7 mm from the emitter. Some data have been taken at 6.1 - 11.5 mm.

With the bath temperature at 1.46°K and a pulse amplitude of 5.9 watts/cm^2 the pulse duration is changed. Pulse durations of 3, 30, and 300 microseconds are used (the pulse rise time is less than 1 microsecond). For the 3 microsecond pulse the detector signals are -.04 volt and the wave velocity is 20.3 m/sec. The 30 and 300 microsecond pulses are received as -.12 and -.18 volt signals with wave velocities of 20.9 and 21.0 m/sec. This indicates that for pulse durations less than ~30 microseconds the glass substrate of the emitter will store a significant portion of the input heat.

A survey of wave velocity as a function of temperature has been made. A pulse amplitude of 15.6 watts/cm^2 and duration of 300 microseconds is used. The results are presented graphically in Figure 45. The detectors are located 2.3 and 7.7 mm from the emitter. A set of typical oscillograms is shown in Figure 47.

The plot of C_2 versus temperature (Fig. 45) is qualitatively in agreement with the theoretical predictions of Khalatnikov. For temperatures below 1.9°K the large amplitude wave speed is greater than C_{20} and for temperatures above 1.9°K it is below C_{20}.*

The oscillograms (Fig. 47) clearly demonstrate the phenomenon of second sound heat transport. At 1.46°K the leading edge of the signal is very sharp while the trailing edge is elongated. The pictures at 1.71°K and 1.91°K indicate the lack of nonlinear effects on either the leading or trailing edges: the integrity of the electrical pulse is completely preserved in the liquid heat pulse. At 2.02°K and above there is evidence of LHe I or helium vapor at the emitter surface since the trailing edge of the pulse cannot be seen 700 microseconds after the arrival of the leading edge. The steep rise of the leading edge at 2.02°K is not an expected result since for all temperatures above 1.9°K the front edge of a positive temperature pulse should be dispersed as in the last two oscillograms. Osborne (Ref. 39) observed a similar occurrence at this temperature when his detectors were close to the emitter. Dessler and Fairbank (Ref. 40) interpreted Osborne's result in terms of a local temperature increase at the emitter surface above the λ-temperature.

At 1.46°K a survey has been conducted of wave speed as a function of pulse amplitude. A pulse duration of 300 μ sec is used and the detectors are positioned in two locations. The results of this survey are presented in Figure 46. The theoretical line represents

* The data used in Figure 45 represent the velocities of the wave fronts. Above 1.9°K the front will disperse (see Fig. 47) and propagate with velocity C_{20}; the back edge of a pulse will steepen and propagate with a velocity which is less than C_{20}.

Khalatnikov's predictions. There are three reasons for the disagreement between data and theory:

a) the detectors are located very close to the emitter and nonlinear effects may not be in full effect at this distance

b) the theoretical line is computed on the basis that the total Joule heat in the emitter is removed by the liquid as a second sound pulse

c) at this temperature $w/C_{20} = .05$ for a heat flux of 3-4 watts/cm^2 and hence the linear relation of Khalatnikov* may not adequately describe C_2 for heat fluxes which exceed this value.

A calculation of heat stored in the glass substrate of the emitter indicates that, for a pulse of 300 microsecond duration, this heat can be neglected with respect to the total input heat. The effect of Kapitza resistance is difficult to estimate. Judging from the oscillograms taken at 1.71°K and 1.91°K (Fig. 47) it seems reasonable to neglect any heat stored in a thermal layer next to the emitter (unless there is evidence of excessive local heating).

The main purpose of a dynamic calibration is to provide an estimate of the temperature jumps observed in a shock generated second sound wave. At 1.46°K a heat pulse of amplitude 15.6 watts/cm^2 should have a ΔT of 48×10^{-3}°K. If the observed velocity

---

* Khalatnikov's equation for C_2 indicates that $C_2 - C_{20}$ should vary linearly with the heat flux.

of the wave is used to infer a heat flux* then this value is 7.1 watts/cm^2 which corresponds to $\Delta T = 22 \times 10^{-3}{}^{o}K$.

At 1.71°K and 1.91°K the integrity of the heat pulse allows a calculation of ΔT based on the total heat input. The value which is computed on this basis is $\Delta T = 18 \times 10^{-3}{}^{o}K$.

A comparison of signals generated by a shock wave and by the gold film emitter is shown in Figure 37 for a bath temperature of 1.46°K. The received signal level in the calibration cell is roughly linear with the computed temperature rise (based on the observed wave velocity). Extrapolating the signal level to that produced in the shock tube (neglecting the effect of increased liquid pressure) yields a value of $\Delta T = 40\text{-}50 \times 10^{-3}{}^{o}K$ for the 1.46° case. At 1.71°K the shock tube ΔT is $\sim 50 \times 10^{-3}{}^{o}K$ and at 1.91°K $\sim 36 \times 10^{-3}{}^{o}K$. These values of ΔT correspond to a relative velocity w of approximately 3 m/sec.

*Based on Khalatnikov's analysis.

IV. CONCLUSIONS

A new cryogenic shock tube has been used to investigate the flow field produced by a shock wave which reflects from a helium gas-liquid interface. Wave diagrams have been constructed from the data: the incident, reflected, and transmitted wave trajectories are shown. Above the λ-point a single transmitted shock is observed in the liquid; below the λ-point two transmitted shocks (corresponding to first and second sound) are observed.

The wave trajectories and liquid flow field can be computed using Khalatnikov's expressions for nonlinear first and second sound waves (which are valid up to second order in the perturbation velocities). There are small but consistent differences between theory and experiment. These may be due to limitations of the second order theory or, more likely, to evaporation processes at the gas-liquid interface - both of which warrant further investigation.

These experiments represent a first step in using shock waves to investigate nonlinear phenomena in liquid helium and demonstrate the feasibility of the approach.

APPENDIX A

IDEAL SHOCK TUBE EQUATIONS AND NOTATION

An ideal shock tube differs from a real shock tube in two ways. First, the diaphragm is modeled as a massless piston capable of infinite acceleration so that an ideal piston velocity is achieved instantaneously. Second, the walls of the tube do not interact with the gas through any form of momentum or energy transfer. Finite diaphragm opening time and gas-wall interactions do occur in the real shock tube and their effect on deviations from ideal behavior can range from negligible to very large.

A conventional ideal shock tube is depicted in Figure 1. If the gases used are perfect then the flow regions, pressure history, temperature history, and wave diagram (x-t diagram) can be as shown in the figure. Flow region notation assigns the region number as a subscript to the variables (velocity, density, pressure, temperature, etc.) in that region. The subscript s refers to the incident shock wave while R refers to the reflected wave.

A. 1. Ideal Equations

By applying conservation laws to mass, momentum, and energy it is possible to obtain the shock wave "jump" conditions. If the gas is assumed to be perfect in all flow regions then:

$$\frac{\rho_2}{\rho_1} = \frac{U_s}{U_s - u_2} = \frac{M_s^2}{1 + \frac{\gamma_1 - 1}{\gamma_1 + 1}(M_s^2 - 1)}$$

$$\frac{p_2}{p_1} = 1 + \frac{2\gamma_1}{\gamma_1 + 1}(M_s^2 - 1)$$

$$\frac{T_2}{T_1} = \frac{p_2}{p_1} \cdot \frac{\rho_1}{\rho_2} = 1 + \frac{2(\gamma_1 - 1)(M_s^2 - 1)(1 + \gamma_1 M_s^2)}{(\gamma_1 + 1)^2 M_s^2}$$

where $M_s \equiv \frac{U_s}{a_1}$

The expansion waves which travel through the driver gas after the diaphragm ruptures are isentropic waves. Consequently, it is possible to find the fluid properties of region 3 in terms of the conditions in region 4 (note that the boundary conditions at the contact surface require $u_3 = u_2$ and $p_3 = p_2$):

$$\frac{\rho_3}{\rho_4} = \left(1 - \frac{\gamma_4 - 1}{2} \frac{u_2}{a_4}\right)^{\frac{2}{\gamma_4 - 1}}$$

$$\frac{p_3}{p_4} = \left(1 - \frac{\gamma_4 - 1}{2} \frac{u_2}{a_4}\right)^{\frac{2\gamma_4}{\gamma_4 - 1}}$$

$$\frac{T_3}{T_4} = \left(1 - \frac{\gamma_4 - 1}{2} \frac{u_2}{a_4}\right)^2$$

Using the above shock tube relations "the shock tube equation" may be written as:

$$\frac{p_4}{p_1} = \frac{p_4}{p_3} \cdot \frac{p_2}{p_1} = \frac{1 + \frac{2\gamma_1}{\gamma_1+1}(M_s^2-1)}{\left[1 - \frac{\gamma_4-1}{\gamma_1+1}\,\frac{a_1}{a_4}\,\frac{M_s^2-1}{M_s}\right]^{\frac{2\gamma_4}{\gamma_4-1}}}$$

The "jump" conditions applied across the reflected shock yield the following equations for a perfect gas:

$$\frac{U_R}{U_s} = \frac{1}{M_s^2} \cdot \frac{p_2}{p_1} - \frac{u_2}{U_s}$$

$$\frac{\rho_5}{\rho_2} = \frac{U_R+u_2}{U_R}$$

$$\frac{p_5}{p_2} = 1 + \gamma_1\left(\frac{\rho_2}{\rho_1} - 1\right)$$

$$\frac{T_5}{T_2} = \frac{p_5}{p_2} \cdot \frac{\rho_2}{\rho_5}$$

A. 2. Strong Shock Waves

For the case when $M_s^2 >> 1$ it is possible to greatly simplify the above equations. In the special case of helium gas ($\gamma = 5/3$) in both driver and test sections the strong shock equations are:

$$\frac{\rho_2}{\rho_1} \leqslant 4 \qquad \frac{u_2}{U_s} \leqslant \frac{3}{4}$$

$$\frac{p_2}{p_1} \leqslant \frac{5}{4} M_s^2 \qquad \frac{T_2}{T_1} \leqslant \frac{5}{16} M_s^2$$

$$M_2 \leqslant 1.34$$

$$1 \geqslant \frac{\rho_3}{\rho_4} \geqslant \left(1 - \frac{M_s}{4} \frac{a_1}{a_4}\right)^3$$

$$1 \geqslant \frac{T_3}{T_4} \geqslant \left(1 - \frac{M_s}{4} \frac{a_1}{a_4}\right)^2$$

$$\frac{\rho_5}{\rho_1} \leqslant 10 \qquad \frac{U_R}{U_s} \geqslant \frac{1}{2}$$

$$\frac{p_5}{p_1} \leqslant \frac{15}{2} M_s^2 \qquad \frac{T_5}{T_1} \leq \frac{3}{4} M_s^2$$

APPENDIX B

DESCRIPTION OF THE APPARATUS AND PROCEDURE

B. 1. The Shock Tube System

The shock tube consists of three stainless steel tubes: 1-inch diameter driver and test sections and a larger diameter support tube (Fig. 2). These three component tubes are arranged in a vertical configuration with the top of the test section bolted to the bottom of the support tube. A flexible bellows is used to attach the upper portion of the driver to the top of the support tube. This bellows allows the driver to be raised and lowered (inside the support tube) with respect to the test section so that a diaphragm rolling mechanism can replace the ruptured portion of diaphragm material.

B. 1. a. Driver Section

The driver section is composed of two concentric tubes with a gap between them (Fig. 3). The inside tube has a 1-inch ID and a 1 1/8-inch OD while the outside tube has a 1 3/4-inch ID and a 1 7/8-inch OD. The driver section extends over the entire length of support tube and has an overall length of 38. 5 inches. A solid aluminum rod of 7/8-inch OD fills all but the bottom 10 inches of the inner driver tube.

This aluminum rod is useful because it has a large thermal mass (maintained at approximately room temperature) which aids in keeping the incoming driver gas "warm". It occupies a

large part of the driver volume so that filling the driver section to burst pressure takes less time. Finally, the rod forces the incoming driver gas to enter the actual driver chamber by flowing along the wall (which is heated slightly above room temperature). This inflow geometry is beneficial in creating a turbulent mix of the gas which makes the gas temperature distribution more uniform.

The inner driver section wall is heated with a heating tape (rated for 576 watts at 120 volts) which is wrapped around the bottom 10 inches of the inner tube. A variac is used to control the voltage to this heater and during run conditions (test section maintained at cryogenic temperatures) a steady state power input of 4 to 6 watts is used. The heating tape is covered with a radiation shield consisting of alternate layers of quartz fiber insulator and 1/2-mil aluminum foil. The same kind of radiation shield is used to wrap the outside of the outer driver tube. The gap between the two driver tubes is evacuated (by means of a pump-out port) so that gaseous heat conduction between the inside and the outside of the driver is eliminated.

The flange at the bottom end of the driver section is silver soldered to the inner tube and soft soldered to the outer tube (a low temperature solder is necessary since the heating tape and radiation shield have to be installed before the final soft solder joint is made). The underside of this flange has an O-ring groove (upper diaphragm seal) of unique cross section machined

in it (Fig. 3). Since the driver section is raised to release the diaphragm it is necessary to insure that the O-ring will not fall out of the groove while allowing freedom of O-ring action to provide the desired gas seal. The "R" cross section has met both goals. The special cryogenic O-rings which are used to seal the diaphragm will be described in section B.2.

The two driver tubes are joined at the top end by a 1/2-inch thick flange. This flange is a rectangle of dimensions 3 inches (front-to-back) by 9 inches (side-to-side). The elongated sides are needed for the clamps which raise and lower the driver section. The outer tube is silver soldered to the flange while the inner tube joint is formed with a flexible silicone compound (R. T. V.). This flexible joint was found necessary when numerous solder joints cracked during the initial cryogenic shakedown runs.

One final feature of the driver section is a flexible metal hose which links the driver section to either the vacuum pump or the high pressure gas. This hose is a brass bellows of 1/4-inch ID, 5 feet long, and covered with a brass braid. With silver soldered end couplings the hose is rated for use from vacuum to 2300 psi (burst pressure 4200 psi). One end is attached to the driver section control panel while the other end is joined to a valve and brass end plate assembly which bolts onto the top driver section flange.

B. 1. b. Test Section

The driver section consists of a 3-inch long transition section bolted to a 19-inch long tube. This overall length of 22 diameters is generally sufficient to insure that fully-formed shock waves can be observed near the end of the test length when the diaphragm is opened using knife edges.

The 19-inch tube has a wall thickness of 1/16-inch to minimize the steady state radial temperature gradient through the wall. Its simplicity allows for ease in changing the test section geometry since all the machining work was confined to the transition section. There are no side wall gauges as all shock wave instrumentation is mounted on an endplate which is bolted to the bottom test section flange.

The short transition section serves several purposes but its main use is to attach the top of the test section to the bottom of the support tube. A 1/2-inch thick flange is used at the top of the transition section to provide a large thermal mass which is at cryogenic temperatures. In addition to an O-ring groove and bolt holes for attachment to the support tube, this flange has an O-ring for a lower diaphragm seal, a knife edge groove, diaphragm roll guides, and driver section guides.

The cross section of the lower diaphragm seal groove is the standard " U". The knife edge groove holds the knife edge which is a separate part (this will be discussed below).

Since the diaphragm must be rolled in order to remove the

ruptured portions, the two diaphragm guides keep the roll in position while the diaphragm material passes between the driver and driven sections. The guides form two slots with the transition section top flange. The outer edges of the guides are smoothed to a large radius of curvature to aid in turning the diaphragm 90^{o}.

The top pieces of the diaphragm guides act as driver section constraints in the sideways direction since they extend 1/2-inch above the transition flange. For front and back driver guides two nylon pegs are used. These pegs are 1-inch high and they are screwed directly into the transition flange.

The transition section has 1/8-inch wall so that a 1/2-inch electrical connector disc can be soldered into it. This disc was used with fine-wire thermocouples to observe test gas temperatures (discussed in Sec. II. C).

The knife edges are made from two 1/32-inch thick strips of stainless steel which are silver soldered into an "X" configuration. This "X" is soft soldered into a ring and then the top edges of the "X" are hand filed and sharpened. The inside of the ring is milled out to form a square "hole" of 3/4 inch on a side* (the four tips of the "X" are soldered to the four corners of this square). The sides of the square are filed down to create a

* This knife edge arrangement presents a 30% blockage to the shock tube cross sectional area, however this effect has been found to be negligible (e.g., 17-inch and 6-inch GALCIT shock tubes).

radius of curvature to lessen stress concentrations on the diaphragm petals.

Several different "X" configurations were tried and the final one has leading edges which are actually a few mils above the surface of the transition section flange. This arrangement lowers the diaphragm burst pressure which allows the driver to be filled more rapidly and also greatly reduces diaphragm shattering at cryogenic temperatures.

B. 1. c. Support Section

The support tube has a 3 1/2-inch ID and is 32. 5 inches in length. A support flange has been silver soldered 20. 5 inches above the bottom of the tube. This tube has a wall thickness of 1/16-inch below this flange to restrict heat conduction down the support tube and a 1/8-inch wall above it. The portion of the tube below the support flange has a small flange at the end for attachment to the test section. Above the support flange are diaphragm rolling spindles (which will be discussed below), a 1-inch ID pump-down and test gas inlet port, and a large rectangular flange at the top end. This top flange mates with a bellows-clamp-flange (which will be discussed below).

This support tube is not concentric with the support flange. This is due to space considerations within the glass dewar. Two electrical connectors and a cryogenic fluid fill port are located in the space provided by offsetting the support tube on the flange.

B. 1. d. Diaphragm and Diaphragm Rolling Mechanism

The major design feature of this shock tube is the diaphragm rolling mechanism. This mechanism was suggested by Professor D. Coles of this laboratory as a simple but effective means of changing diaphragms without opening the shock tube to atmospheric contamination.

There is a direct analogy between the diaphragm rolling mechanism and the film rolling mechanism of a camera. The unused diaphragm roll is wound around an output spindle which is positioned near the top of the support tube. Off this spindle the diaphragm runs parallel to the driver section down to one diaphragm guide. The diaphragm separates the driver from the driven section as it goes from one diaphragm guide to the other. Finally, it runs back up the support tube where it is wound around a takeup spindle. The second spindle is connected to an external knob which is turned to roll the diaphragm.

The working scheme of the mechanism is as follows:

1) After a shot the driver section is raised and clamped in the "up" position.
2) The takeup spindle knob is turned several times to advance unused diaphragm material into position between the driver and driven sections.
3) The driver section is lowered and clamped in the "down" position so that the next shot can be fired.

Two brass saddles were soldered to the outside of the

support tube in order to provide a housing for the spindles. Holes were drilled through these saddles and the support tube so that 1/8-inch rods could be used for the spindles. Larger diameter holes were counterbored in the brass pieces to provide room for the enlarged end portions of each spindle.

The output spindle has a slotted head piece which allows the unused diaphragm to be wound up by inserting a screwdriver into the slot and turning it. This spindle is vacuum sealed at each end with end caps which hold O-rings since there is no need for external connections once the diaphragm has been installed on this spindle.

The takeup spindle requires dynamic O-ring seals since it does have an external connection (to a knob) and it must be vacuum tight while rotating. The spindle seals are made using the spindle ends as O-ring holders and then tightening the "nut" end until sufficient axial pressure is obtained to insure a vacuum seal under rotation. The takeup spindle is a steel rod with a slot cut into the middle portion. The diaphragm leading edge is inserted into this slot in the same way the film leading edge is inserted into a takeup spindle in a camera.

The flexible diaphragm material used in the shock tube is 1/2- and 1-mil thick mylar. Other plastic materials were tried but the performance of mylar at cryogenic temperatures was found to be equal or superior. Immersed in LN_2 the mylar was found to be just as flexible at $77^{o}K$ as at room temperature.

Although the flexibility of mylar is unchanged by a decrease in temperature the burst pressure is affected. Using the same knife edge geometry, the burst pressure can increase by as much as a factor of four between room temperature and 1.5^{o}K run conditions. A relatively low burst pressure was desirable in order to fill the driver section rapidly with gas, so the 1/2-mil thick mylar was used for the data taking runs.

A 2-inch wide, 2000-foot long roll of this diaphragm was purchased from a local distributor. Twenty-foot sections were cut and attached to each spindle. Up to seventy shots are obtained using one of these twenty-foot lengths. The knife edges are arranged in their groove so that the sides of the square "hole" are parallel and perpendicular to the diaphragm axis. This means that only the center 3/4-inch of the 2-inch wide diaphragm is cut: the uncut sides are capable of advancing the roll without tearing.

A note should be made about diaphragm shattering . This problem appears at cryogenic temperatures but it can be solved using the raised knife edge configuration discussed previously as long as the cutting edges are kept very sharp.

B. 1. e. Bellows and Clamps

As indicated above, raising and lowering the driver section is a critical function in the operation of this shock tube. The bellows is used to provide the needed driver displacement while maintaining a vacuum seal. The two-position clamps do the actual raising and lowering of the driver section locking into both "up" and "down" positions.

The bellows is a two-ply brass corrugation type* with 7 lbs. per inch spring constant. The bottom of the bellows is soldered to a flange on the outside of the driver section. The top of the bellows is soldered to a rectangular flange which bolts onto the top flange of the support section. The equilibrium position of the bellows is reached when the driver and test section are touching so that raising the driver section compresses the bellows.

As noted previously, the bellows-to-support-section flange is rectangular as is the flange at the top of the driver section. This is necessary because these flanges must extend further sideways to accommodate the clamps. These clamps† are mounted vertically on the top support tube flange using aluminum 90^{o} angle mounts.

These clamps are rated for a maximum traverse load of

---

* Obtained from the Robert Shaw Controls Co., Fulton Sylphon Division, Anaheim, Ca.

† Lapeer Mfg. Co., Knu-Vise Products, Model P&P - 800.

800 lbs. and maximum end loads of 1200 lbs. The clamp handles are sufficiently long to allow locking forces of 60 lbs. under maximum end load conditions. This means that it is possible to clamp down the driver tightly enough on the test section that the O-rings are able to provide adequate pressure/vacuum seals above and below the diaphragm even at cryogenic temperatures

B. 1. f. Shock Tube Support System

A control panel is used in regulating and measuring gas pressures in the driver and test sections. The shock tube is roughly evacuated using a Welch pump* and then pumped to $< 10^{-4}$ torr with a Consolidated Vacuum diffusion pump.† Both test and driver gas are filtered with an LN_2 cold trap which contains activated carbon.

As a vacuum system the shock tube leak-out-gassing rate is $\sim 2 \times 10^{-3}$ torr per hour at room temperature after diffusion pumping for an hour. With the test section at cryogenic temperatures almost all gases are frozen so the rate is less than 10^{-3} torr per hour.

---

* Model 1397; free air mass flow rate: 375 liters per minute.

† Model VMF-50; mass flow rate at 10^{-4} torr: 50 liters per minute.

B.2. The Cryogenic System

The cryogenic system of this facility consists mainly of the dewars which contain the cryogenic fluids and the control panel that is used in various roles during cryogenic run conditions. Other shock tube design features which are unique to the low temperature environment will be discussed below.

B.2.a. Liquid Nitrogen Dewar

The LN_2 dewar* is constructed of type 304 stainless steel. It has an 8 1/4-inch ID and a nominal depth of 37 inches. For use with a glass LHe dewar it was necessary to extend the depth of the LN_2 dewar by constructing a urethane-form-filled collar (Fig. 6). This was accomplished by soft soldering stainless steel bands to the top inside and outside dewar walls and then pouring a liquid urethane mixture into the mold which was formed by the two bands. The useable dewar depth is now 38 inches.

The LN_2 dewar is used alone when the $77^{\circ}K$ case is being run since the liquid nitrogen boil-off rate is quite low in this dewar. For this case the shock tube is placed inside this dewar and LN_2 is poured into the dewar until the entire test section is immersed. The LN_2 bath is always left at atmospheric pressure so no vacuum connections are needed for the LN_2 dewar.

For the LHe cases it is necessary to insert a glass LHe dewar inside the LN_2 dewar. The glass dewar has a vacuum

---

* Gardner Cryogenics Corp., model N-8.2-37.

jacket which must be maintained at cryogenic temperatures whenever there is helium gas inside the dewar.† The LN_2 dewar not only serves the purpose of keeping all of the vacuum jacket immersed in LN_2 but also acts as a safety shield in the event of a glass dewar implosion or explosion.

B.2.b. Liquid Helium Dewar

As indicated above, a pyrex glass dewar (Fig. 6) is used for all of the runs at temperatures below 77°K. The top 8 inches of the dewar are of single-wall construction. A 2-inch ID pump-out port is located in this portion as is the small pump-out line which connects to the vacuum jacket. A standard pyrex 6-inch pipe flange (with O-ring groove) terminates the upper end of the single wall section.

The lower end of this top section forms the transition to the double-walled vacuum jacket. This jacket is fully silvered to reduce radiation heat input. The double-walled section has a 5 5/8-inch ID, 7-inch OD, and extends 36 inches below the top section.

B.2.c. Primary Support Plate

A large rectangular stainless steel plate is used to support both the shock tube and the LHe dewar. The plate is rigidly attached to a large supporting structure which is bolted to the floor and ceiling of the laboratory.

† Helium permeates the pyrex walls of the vacuum jacket much more readily at room temperature than at 77°K.

A 6-inch diameter hole in the center of the plate allows the shock tube to be inserted up to the bottom of the support flange. This flange mates with the top surface of the plate which contains an indium O-ring groove and blind-tapped bolt holes.

The bottom surface of the support plate has been faced-off to insure that the O-ring on the top of the LHe dewar mates with a smooth metal surface. The dewar is held up against the underside of the plate by using a two-piece aliminum collar (Fig. 6). This collar is installed around the dewar beneath the pyrex pipe flange and then bolted to the support plate. Since the shock tube support flange and the dewar top flange are both vacuum sealed to the plate with O-rings it is possible to regulate the pressure within the LHe dewar by connecting its pump-out port to a cryogenic bath control panel.

B.2.d. O-Rings

All shock tube O-rings used in areas above the support flange are standard Buna-N type. All O-rings below the support flange are indium solder O-rings with the exception of the two cryogenic O-rings which seal off the driver and test sections at the diaphragm.

The use of indium solder O-rings to vacuum seal mating flanges at cryogenic temperatures is a common low temperature technique. The indium comes in the form of a solder wire with .030-inch diameter. A groove with a depth of .015 inch and width of .030 inch is machined in one of the mating flanges. The

indium is cut to a correct length and then pressed into the groove. When a flat surface flange is bolted to this flange the indium overflows the groove and forms an excellent vacuum seal. This seal is capable of functioning properly not only in a cryogenic environment but also after thermal cycling.

Indium solder O-rings must be replaced after the initial seal is broken since the indium is plastically deformed. Consequently another form of cryogenic vacuum seal was needed to meet the diaphragm sealing requirements. At cryogenic temperatures as low as 1.3°K the diaphragm seal must be made and broken as many as 70 times. The seal must be capable of maintaining a pressure difference of several atmospheres for short periods of time and several torr for extended periods.

Commercially available O-rings have proved adequate in the diaphragm sealing application. These O-rings consist of a continuous Teflon ring with an annular cavity to accept a resilient stainless steel cable spring. The Teflon jacket has a wall thickness of only .015 inch so the cable spring is used to expand the jacket and to provide nearly uninterrupted internal support. Specifications on the cryogenic O-rings include operating temperatures from 20°K to 478°K with differential pressures up to 5000 psi.

As noted previously, the driver section O-ring groove was machined with a unique cross section to insure that the cryogenic O-ring would not fall out when the driver was raised and would

function properly when the driver was locked into the "down" position. The groove and the O-rings have worked very well at all temperatures. At room temperature however, Buna-N O-rings seem to seal better for the same driver section clamping force.

B.2.e. Heat Loss Features and Data

Besides constructing the shock tube with a low heat conductivity metal several other techniques and devices have been used to minimize the heat input to the LHe dewar. Some of these features have already been discussed and need only be mentioned here. The support tube is constructed with "thin wall" stainless steel between the support flange and the bottom flange to minimize heat conduction down the walls. The heating tape of the driver section is thermally isolated from the support tube by a vacuum space and radiation shields.

One technique which helps to keep the test section "cold" and the driver section "warm" is to minimize the time that the driver is locked in the "down" position. This lessens the vertical heat conduction through the contact which is by far the greatest heat loss. In practice it is possible to have the driver "down" for less than two minutes per shot.

Initial heat input calculations indicated that gas conduction within the LHe dewar would be a serious problem if the support flange of the shock tube remained at room temperature. Consequently a stainless steel band was soldered around the support flange in order to form a "bucket" with the top of the flange.

LN_2 at 77°K has been used in this bucket as was intended but no significant effect on the LHe boil-off rate was observed.

The LHe boil-off rate is quite acceptable: once the bath level is 2 to 3 inches below the diaphragm location (for the 4.2°K case) it takes several hours and 20 to 30 shots to boil down another four inches. For temperatures below 4.2°K the initial bath level is always below the diaphragm location but boil-off rates are similar to the 4.2°K case. It is possible to fill the LHe dewar to a level several inches above the diaphragm location using 12 to 15 liters of LHe from a storage dewar. Using a 25 liter storage dewar it is possible to operate for over 12 hours with a bath level never more than 6 inches below the diaphragm. (During this period the shock tube can be fired about 60 times with one person operating the apparatus and recording the shot data.)

B.2.f. Cryogenic Support System

The pressure within the LHe dewar is regulated from a control panel. A Kinney pump* is used to evacuate the dewar and maintain the bath pressure below ambient pressure. Regulation of the bath pressure is done manually. As a vacuum system the dewar leak-out-gassing-rate after several hours of pumping is .2 torr per hour.

* Model #KC-46; free air mass flow rate: 1290 liters per minute.

B.3 Instrumentation

The ideal shock tube equation (Appendix A) can be written in the form:

$$U_s = F(T_1,\ T_4/T_1,\ p_4/p_1)$$

for the case of ideal gases with constant ratios of specific heats. The shock tube instrumentation is designed to measure or infer all of the quantities in this equation. Hence one check of the "idealness" of the shock tube can be made by comparing measured shock velocities for a given T_1, T_4/T_1, and p_4/p_1.

B.3.a. Cryogenic Bath Level Detector

For the runs at $T_1 = 77^{\circ}K$ the open metal dewar is used to contain the LN_2. In this case it is possible to visually observe the cryogenic liquid level. The large heat of vaporization and density of LN_2 make it easy to maintain a constant bath level above the diaphragm location by pouring in LN_2 from a small dewar once every hour.

When LHe is used for the $T_1 = 4.2^{\circ}K$ case and $2.3^{\circ}K$ case a level detector is needed. Seven 1/8 - watt Allen Bradley carbon resistors are held at fixed vertical positions in the bath. It is a commonly employed cryogenic technique to measure resistance of one of these resistors in order to determine its temperature (Refs. 17, 25, 26). Since the bath level does not need to be determined very accurately, the resistances are recorded periodically and the bath level is noted as being between two of the resistors.

Repeatability of the bath temperature for the $T_1 = 2.3^{\circ}K$ case is assured using not only a pressure gauge to determine the saturated vapor pressure but also by pumping on the bath until the resistance value of one of the resistors known to be in the liquid is repeated. For example: a resistor with 530-ohm resistance at room temperature has a resistance of 118 ± 2-kohm for a series of runs at $2.3^{\circ}K$. This means that the test section temperature is repeatable to better than one percent for this series.

The shock tube diameter is a characteristic length scale to determine the cryogenic fluid level (with respect to the diaphragm location). Consequently the resistors are spaced at 1- and 2-inch intervals. LHe is added when the liquid level has boiled down to 4 - 6 ($T_1 = 4.2^{\circ}K$) or 8 - 10 ($T_1 = 2.3^{\circ}K$) diameters below the diaphragm location.

B.3.b. Test Gas Pressure

The test gas pressure is measured on a Barocel Electronic Manometer with seven scales covering the range 0-10 torr down to 0-.01 torr. This gauge was calibrated against a McLeod gauge and found to be accurate to within two percent. However, the instrument has a zero drift caused by temperature fluctuations so that the Barocel needs to be re-zeroed periodically during runs when test gas pressures of 10^{-2} torr or less are used. The test gas comes to thermal equilibrium within the shock tube before the excess gas is pumped out and the desired test pressure is reached.

B.3.c. Driver Gas Pressure

After clamping the driver section "down" the driver is evacuated to $\sim .01$ torr measured on a thermocouple pressure gauge.* The driver section is filled rapidly with gas until the diaphragm burst and burst pressure are vividly observed on a compound pressure gauge.†

This technique of measuring the driver gas pressure is not very accurate since the gauge needle deflection is slight when filling the driver section rapidly. A slower filling of the driver established the approximate burst pressure much more accurately. Over the course of one day's run at cryogenic temperatures, the burst pressure for a given T_1 case never varied more than ± 5 percent using the visual pressure determination. Using an average value of p_4 for all runs made during one day, the Mach number data for the larger test pressures has very little scatter indicating that the p_4 scatter is not excessive.

B.3.d. Test Gas Temperature

A chromel-constantan thermocouple‡ (.0005-inch diameter wires; time response of $\sim 10^{-2}$ seconds in still air) is used to measure the difference in temperature between the cryogenic bath and the test gas. The ends of the wires are soldered to the pins

---

* Hasting-Raydist, Inc.

† Greer Hydraulics, Inc.

‡ Omega Engineering, Inc.

of an electrical connector. The connector is mounted in the test section wall one inch below the diaphragm location. For the LN_2 case the outside of the electrical connector (and consequently the outside ends of the pins) is completely immersed in LN_2. Under these conditions the ends of the thermocouple are held fixed at $77^{\circ}K$. With the thermocouple junction held in the test gas the voltage output is a direct measure of the temperature difference between the gas inside the shock tube and the cryogenic coolant. The commercial calibration scale for this thermocouple indicates that at $77^{\circ}K$ a voltage output of $\pm$ 26 μvolts corresponds to a temperature difference of $\pm 1^{\circ}K$.

In the LHe cases it is experimentally determined that a temperature gradient at the beginning of the test section has no measurable effect on shock tube performance. Consequently no thermocouple temperature measurements are made at LHe temperatures. The liquid level detector is used to monitor the bath level so that the level could always be maintained within a few shock tube diameters of the diaphragm location.

The gas pressure over the bath is measured using a mercury barometer for the $77^{\circ}K$ and $4.2^{\circ}K$ cases and a 0 - 100 torr Barocel Electronic Manometer for the $2.3^{\circ}K$ runs. After correcting for hydrostatic pressure, standard conversion tables (Refs. 16, 17) are used to obtain the average bath temperature from the saturated vapor pressures.

B.3.e. Driver Gas Temperature

Glass bead thermistors* are mounted in the driver section to determine the temperature of the wall and the gas (Fig. 3). The "wall" thermistors are epoxied to the wall at 1/8 inch and 5 inches above the diaphragm so that the lowest and highest wall temperature can be measured. The voltage drop across the heating tape is adjusted so as to keep the wall temperature 5 inches above the diaphragm around 325°K.

As seen in figure 3 the "gas" thermistors are held away from the driver wall by sturdy copper wires to which are soldered the .003-inch leads from the beads. Thermistors 1, 2, 3, and 4 are located ~ 1/8, 1/2, 1, and 1 1/2 inches vertically above the diaphragm and from .2 to .4 inches away from the shock tube wall. The glass beads are .014 inch in diameter with a quoted time response of 1 second in still air. For the operating conditions of the shock tube the experimentally observed time response is roughly .1 second (Fig. 8). Based on the commercial calibration scale the error in absolute temperature at 300°K is ± 6°K.

B.3.f. Shock Wave Velocity

The shock velocity is determined by measuring the time required for the shock to travel between two gauges and then dividing the distance between these gauges by the measured time. An adaptation of the standard shock tube thin film side wall gauge is used in determining shock velocity.

* Fenwal Electronics, Inc.

A microscope glass slide is cut in half along its length. The cut side is sanded smooth and one end is tapered (Fig. 7). Platinum films are baked into the front face of the slide, indium contacts are soldered from the front face to the back, and then copper wires are soldered to the indium contacts on the back face. The flat end of the slide is epoxied perpendicular to the test section bottom flange (Fig. 5).

The films are several hundred Angstroms thick, $\sim .03$-inch high, and $\sim .5$-inch wide. Room temperature resistances range from 300 to 600 ohms and the resistances are roughly 30% lower at 4.2°K. Film height and the distance between films are measured on a Kodak optical comparator. Repeatability of the film separation distances (4 - 5 cm) is within $\pm .1$% for six measurements taken over three months. The slide is perpendicular to the flange to within $\pm .5$ of a degree. The cross sectional area of the slide represents 3.2% of the tube cross section.

B. 3. g. Additional Instrumentation

Thermocouple and thermistor data are taken using a multifunction meter* capable of reading five significant figures. The voltage output of the films is amplified a thousand times and displayed on an oscilloscope†. A time-mark** is made on each

---

* Hewlett-Packard; Model 3450A.

† Tektronix; Model 555 dual beam using type "L" plug-ins.

** Using a Tektronix Time Mark Generator; Model 180A.

oscilloscope beam as a common reference time. All of the electronic equipment is warmed up for at least 2 hours before data are taken, and the time sweeps of the scopes are calibrated‡ several times during the day.

A note should be made about current levels in the platinum films. For most cryogenic runs a current of 10^{-3} amps (total power input of 10^{-3} watts using 3 films) is used. In order to check the possibility of local test gas heating runs were made in all cryogenic cases over all test pressures with a current level of 2×10^{-4} amps (total power input of 4×10^{-5} watts). No quanitative difference in shock velocity or qualitative difference in the voltage history was observed.

‡ Using a Hewlett-Packard Pulse Generator; Model 214A.

B.4. Data Reduction

Thermocouple and thermistor data are printed on paper tape at a rate of 12 or 14 readings per second. From the printout it is possible to convert the voltages or resistances to temperatures using commercial calibration scales. Knowing the printer rates makes it possible to infer the temperature of the devices as a function of time.

Data from the oscillograms are obtained by moving a cross hair over the picture and recording its position when directly above a time-mark or shock arrival point (Fig. 7). Lines are scribed on the oscillogram for cases in which the trace rise time exceeded 1 μsec. Time correction factors for each run day, oscilloscope, and beam are calculated using the same data reduction technique. This method gives repeatable results when one oscillogram is reduced several times. The errors involved in determining the shock arrival time vary from ± 1% for the highest test pressure runs to ± 4% for the lowest test pressure runs.

APPENDIX C

THEORETICAL CONSIDERATIONS OF SHOCK TUBE TEST TIMES

The test time of a shock tube is the amount of time t_s between the arrival of the incident shock and the contact surface, as seen by an observer located a distance x_s from the diaphragm (Fig. 16). For many shock tube problems it is the thermodynamic state of the gas or the flow in region 2 which is of interest. Consequently, the test time is an important parameter in characterizing the shock tube performance.

C.1. Ideal Test Time

For an ideal shock tube (Fig. 16) it is possible to write the test time as:

$$t_s = t_2 - t_1 = x_s\left(\frac{1}{u_2} - \frac{1}{U_s}\right)$$

$$t_s = \left[\frac{U_s - u_2}{U_s}\right]\left[\frac{1}{u_2}\right] x_s$$

From the shock tube equations (Appendix A) it can be shown that:

$$u_2 = a_1\left[\frac{2}{\gamma_1+1}\quad\frac{M_s^2-1}{M_s}\right]$$

$$\frac{U_s}{U_s - u_2} = \left[\frac{(\gamma_1+1)M_s^2}{(\gamma_1-1)M_s^2 + 2}\right]$$

Consequently:

$$t_s = \left[\frac{(\gamma_1-1)M_s^2 + 2}{2\,M_s\,(M_s^2 - 1)}\right]\frac{x_s}{a_1} \qquad (1)$$

$$t_s = F(\gamma_1,\ M_s)\,\frac{x_s}{a_1}$$

The ideal test times presented for the various cases are calculated using the observed M_s rather than the M_s predicted by the shock tube equation. From equation 1 it can be seen that for strong shocks in a monatomic gas

$$t_s \doteq \frac{1}{3}\,\frac{x_s}{U_s}$$

The ideal test time increases linearly with distance along the test section.

C.2. Boundary Layer Considerations

Roshko (Ref. 11) and Mirels (Ref. 12, 13) have considered the effects of the wall boundary layer on shock tube test time. The basic concepts and notation of LBL and TBL theory are shown in Figure 16. The boundary layer acts as a mass sink at the wall causing the shock wave to decelerate as the contact surface accelerates. A maximum separation distance ℓ_m is attained when the shock and contact surface velocities are equal.

Consider the flow when the limiting separation distance is attained. In shock-fixed coordinates the flow rate through the shock is

$$\dot{m}_s = \rho_{e,o}\, u_{e,o}\, \frac{\pi d^2}{4}$$

for a circular cross section tube. This must be equal to the flow rate through the boundary layer at the contact surface. If the boundary layer is thin with respect to the tube radius then

$$\dot{m}_{cs} = \pi d\, \delta\, \rho_{w,o}(u_w - u_{e,o})$$

The boundary layer thickness at the contact surface can be written as

$$\delta = \beta_n\, \ell^{1-n} \left(\frac{\nu_{w,o}}{u_w - u_{e,o}} \right)^n$$

where $n = 1/2$ for an LBL and $n = 1/5$ for a TBL. Equating $\dot{m}_s$ to $\dot{m}_{cs}$ with $\ell = \ell_m$:

$$\ell_m = \left[\frac{d}{4\beta_n} \frac{\rho_{e,o}}{\rho_{w,o}} \frac{u_{e,o}}{u_w - u_{e,o}} \left(\frac{u_w - u_{e,o}}{\nu_{w,o}} \right)^n \right]^{\frac{1}{1-n}}$$

The rate of increase of mass between the shock and contact surface may be written

$$\dot{m} = \dot{m}_s - \dot{m}_{cs} \doteq \rho_{e,o} \pi d^2 \frac{d\ell}{dt} \qquad (2)$$

if $\rho_e \doteq \rho_{e,o}$. Introducing the similarity variables

$$X = \frac{x_s}{\eta \ell_m}$$

and

$$T = \frac{\ell}{\ell_m}$$

it is possible to write equation 2 in the form

$$T^{1-n} = 1 - \left(\frac{dT}{dX}\right)$$

Upon integrating this equation the following solutions are found:

$$X = -2[\ell n(1-T^{\frac{1}{2}}) + T^{\frac{1}{2}}] \text{ for an LBL}$$

$$X = -\frac{5}{4}\left[\ell n\left(\frac{1-T^{1/5}}{1+T^{1/5}}\right) + -2\tan^{-1}(T^{1/5}) + 4T^{1/5}\right] \text{for a TBL}$$

To obtain accurate estimations for ℓ_m most of the simplifications in the above analysis are eliminated in computing the values to be used for β_n. Mirels has carried out a detailed numerical analysis to determine β_n as a function of M_s for different values of Prandtl number (Pr), $\rho\mu$, and γ_1.

The LBL and TBL values for ℓ_m are shown in Table 4. The experimentally measured values of U_s (M_s) are used with the ideal shock tube equations in these calculations. If $\ell/\ell_m \ll 1$ then $t_s \doteq \frac{\eta}{\eta-1} \frac{\ell}{u_w}$. If $\ell/\ell_m = O(1)$ then $t_s \doteq \ell/u_w$. Based on the assumption that the shock moves with a constant velocity, Mirels develops an analytical expression for t_s which covers the entire range of ℓ/ℓ_m values. The test times computed in the present analysis follow this same course.

Values of the viscosity of gaseous helium at temperatures below 10°K are taken from References 27, 28, and 29.

C. 3. Wall Temperature Computations

Sturtevant and Okamura (Ref. 24) have calculated the LBL wall heat transfer q_w behind a shock wave. This analysis assumes that the gas is perfect, $Pr = 1$, $\rho\mu$ = constant, and that $T_w = T_1$. The last restriction can be dropped with no major changes so that it is possible to find $q_w = q_w(T_w)$.

The steady, two-dimensional ($d >> \delta$) boundary layer equations can be written for this case as

CONTINUITY $$\frac{\partial \rho u}{\partial x} + \frac{\partial \rho v}{\partial y} = 0$$

MOMENTUM $$\frac{\partial \rho u^2}{\partial x} + \frac{\partial \rho uv}{\partial y} = \frac{\partial \tau}{\partial y}$$

ENERGY $$\frac{\partial \rho uJ}{\partial x} + \frac{\partial \rho vJ}{\partial y} = \frac{\partial}{\partial y}(\tau u - q)$$

The flow picture and notation are seen in Figure 16.

Sturtevant and Okamura (S-O) characterize the boundary layer thickness as

$$\delta = \left(\frac{2 \nu_e x}{u_w + u_e} \right)^{\frac{1}{2}}$$

where x is the distance from the shock wave. They also define a boundary layer scaling function

$$\eta(x, y) = \left(\frac{u_w + u_e}{2 \nu_e x} \right)^{\frac{1}{2}} \int_o^y \frac{\rho}{\rho_e} dy$$

and a normalized stream function

$$f'(\eta) = \frac{u-u_e}{u_w-u_e}$$

Using the momentum equation and boundary conditions S-O numerically calculate $f'(\eta)$ for u_w/u_e between 0 and ∞.

If $T_w \neq T_1$ then the solution of the energy equation is

$$J \equiv C_p T + \tfrac{1}{2} u^2 = \alpha + \beta u$$

The values of α and β can be determined by evaluating J in the external flow and at the wall. It follows that

$$J = C_p T_w + \tfrac{1}{2} u_w^2 + \left[C_p(T_e-T_w) + \tfrac{1}{2}(u_e^2-u_w^2)\right] \frac{u_w-u}{u_w-u_e}$$

The wall shear τ_w and heat transfer q_w are

$$\tau_w = \mu_w \left(\frac{\partial u}{\partial y}\right)_w$$

$$q_w = -k_w \left(\frac{\partial T}{\partial y}\right)_w$$

Using the expression for J the heat transfer may be written as

$$q_w = \tau_w u_w \left[1 + \frac{C_p \Delta T}{u_w(u_w-u_e)}\right]$$

where $\Delta T = T_w - T_1$ (this is the S-O result for $\Delta T = 0$).

S-O derive the wall shear as

$$\tau_w = \rho_e \frac{\delta}{x} \left(\frac{u_w^2 - u_e^2}{2} \right) f''(0)$$

where f''(0) is a tabulated function approximately equal to -.6 for an arbitrary strength shock wave in helium.

The heat transferred to the wall raises the wall temperature such that

$$- q_w t = \rho_s C_s \delta_s \Delta T$$

where

$$\delta_s \doteq \left(\frac{k_s}{\rho_s C_s} t \right)^{\frac{1}{2}}$$

and

$$t = \frac{x}{u_w}$$

It is now possible to combine the equations and write an expression for ΔT:

$$\Delta T = \frac{\tau_w u_w}{\left(\frac{\rho_s C_s k_s u_w}{x} \right)^{\frac{1}{2}} + \frac{\tau_w C_p}{u_w (u_w - u_e)}}$$

For the 2.3°K case and 4.2°K case the computed values of ΔT are such that

$$\frac{C_p \Delta T}{u_w (u_w - u_e)} \ll 1$$

and the value of ΔT can be calculated using the equation

$$\Delta T \equiv T_w - T_1 \doteq (.3) \left(\frac{2u_w}{u_w + u_e} \right)^{\frac{1}{2}} \left(\frac{\rho_e \mu_e}{\rho_s C_s k_s} \right)^{\frac{1}{2}} (u_w^2 - u_e^2)$$

The computed values for T_w are given in Table 3.

Values of k_s and C_s for type 304 stainless steel are taken from Reference 30. The viscosity of helium gas used in these calculations is found in References 27-29.

C.4. Test Time as a Function of x_s and T_w

In order to interpret the experimental test time data in terms of LBL or TBL values, it is necessary to use x_s and T_w as adjustable parameters (the computations of the previous section give an estimate of T_w for an LBL). The theoretical curves and data for all four T_l cases are displayed in Figures 21-26. Values of x_s and T_w used in the body of this paper are selected from these figures on the basis of the best qualitative fit to the data.

APPENDIX D

DISCONTINUITIES OF FIRST AND SECOND SOUND IN LIQUID HELIUM II*

The conservation equations for LHe II can be written as:

MASS $$\frac{\partial \rho}{\partial t} + \vec{\nabla} \cdot \vec{j} = 0 \qquad (1)$$

MOMENTUM $$\frac{\partial \vec{j}}{\partial t} + \vec{\nabla} \cdot \vec{\vec{\pi}} = 0 \qquad (2)$$

ENERGY $$\frac{\partial E}{\partial t} + \vec{\nabla} \cdot \vec{Q} = 0 \qquad (3)$$

and the equation of motion for the superfluid component has the form:

SUPERFLUID MOTION $$\frac{\partial \vec{v}_s}{\partial t} + \vec{\nabla} \left(\Phi + \frac{v_s^2}{2} \right) = 0 \qquad (4)$$

where:

ρ = mass density

$\vec{j}$ = $\rho \vec{v}$ = mass flux = momentum density

$\vec{v}$ = particle velocity

$\vec{\vec{\pi}}$ = momentum flux

E = energy density

$\vec{Q}$ = energy flux

$\vec{v}_s$ = superfluid velocity

Φ = chemical potential / unit mass

Equations (1) - (4) are generally valid. The thermodynamic functions in general depend on pressure (p), temperature (T), and the relative velocity ($\vec{w}$) between the normal fluid and superfluid

* Based on the work of I. M. Khalatnikov (Ref. 37).

components. If the assumption of "small" relative velocity (small with respect to the undisturbed speed of second sound) is made, then considerable simplification is possible.

Consider the one-dimensional case of a discontinuity or "jump" propagating in LHe II. If the discontinuity moves with constant velocity $\vec{C}$ in the laboratory frame, then in a coordinate system moving with the discontinuity the flow is 'steady." In this steady frame equations (1)-(4) lead to jump conditions relating quantities on the two sides (1 and 2) of the jump:

$$[\vec{j}]_1^2 = 0 \tag{5}$$

$$[\vec{\vec{\pi}}]_1^2 = 0 \tag{6}$$

$$[\vec{Q}]_1^2 = 0 \tag{7}$$

$$\left[\Phi + \frac{v_s^2}{2}\right]_1^2 = 0 \tag{8}$$

With the approximation of small relative velocity $\vec{w}$, the jump conditions can be written to order w^2. The symbol $\sim$ over a thermodynamic function will denote its dependence on w.

$$(5) \Rightarrow \left[\rho_s \vec{v}_s + \rho_n \vec{v}_n\right]_1^2 = 0 \tag{9}$$

$$(6) \Rightarrow \left[p\vec{\vec{I}} + \rho_s \vec{v}_s \vec{v}_s + \rho_n \vec{v}_n \vec{v}_n\right]_1^2 = 0 \tag{10}$$

$$(7) \Rightarrow \left[\vec{j}\left(\tilde{\Phi} + \frac{v_s^2}{2}\right) + \tilde{\rho}\,\tilde{s}\,T\vec{v}_n + \rho_n(\vec{w}\cdot\vec{v}_n)\vec{v}_n\right]_1^2 = 0 \tag{11a}$$

$$(8) \Rightarrow \left[\tilde{\Phi} + \frac{v_s^2}{2}\right]_1^2 = 0 \qquad (12)$$

$$(9) \;\&\; (12) \Rightarrow \left[\tilde{\rho}\,\tilde{s}\,T\,v_n + \rho_n (w \cdot v_n) v_n\right]_1^2 = 0 \qquad (11b)$$

where:

ρ_s = superfluid density

ρ_n = normal fluid density

$\tilde{\rho} \equiv \rho_s + \rho_n$

$\vec{v}_n$ = normal fluid velocity

p = pressure

$\vec{j} = \rho_n \vec{v}_n + \rho_s \vec{v}_s = \tilde{\rho}\vec{v}$

$\tilde{s}$ = entropy/unit mass

T = temperature

$\vec{w} = \vec{v}_n - \vec{v}_s$

The chemical potential (correct to terms quadratic in w) can be expressed as:

$$\tilde{\Phi}(p, T, w) = \Phi(p, T) - \frac{\rho_n}{\rho}\,\frac{w^2}{2} \qquad (13)$$

The thermodynamic identity for $\Phi(p, T)$:

$$d\Phi = -s\,dT + (1/\rho)\,dp \qquad (14)$$

is also valid for $\tilde{\Phi}(p, T, w)$:

$$d\tilde{\Phi} = -\tilde{s}\,dT + (1/\tilde{\rho})\,dp \qquad (15)$$

Note that equation (13) implies:

$$d\tilde{\Phi} = d\Phi - \frac{w^2}{2}\left[\frac{\partial}{\partial T}\left(\frac{\rho_n}{\rho}\right)dT + \frac{\partial}{\partial p}\left(\frac{\rho_n}{\rho}\right)dp\right] \tag{16}$$

Combining (14) with (16):

$$d\tilde{\Phi} = \left[-s - \frac{w^2}{2}\frac{\partial}{\partial T}\left(\frac{\rho_n}{\rho}\right)\right]dT + \left[\frac{1}{\rho} - \frac{w^2}{2}\frac{\partial}{\partial p}\left(\frac{\rho_n}{\rho}\right)\right]dp \tag{17}$$

Comparing (14) to (15):

$$\tilde{s}(p, T, w) = s(p, T) + \frac{w^2}{2}\frac{\partial}{\partial T}\left(\frac{\rho_n}{\rho}\right) \tag{18}$$

$$\frac{1}{\tilde{\rho}(p, T, w)} = \frac{1}{\rho(p, T)} - \frac{w^2}{2}\frac{\partial}{\partial p}\left(\frac{\rho_n}{\rho}\right) \tag{19}$$

Consider the case of a discontinuity moving into undisturbed liquid (side 1) which is at rest in the laboratory frame. Let $\vec{C}$ be the velocity of the discontinuity with respect to the undisturbed liquid. The arrangement in the laboratory frame is as pictured:

SIDE 2		SIDE 1
$\vec{v}_{n2} = \vec{v}_n$		$\vec{v}_{n1} = 0$
$\vec{v}_{s2} = \vec{v}_s$	$\vec{C}$ →	$\vec{v}_{s1} = 0$
$\vec{v}_2 = \vec{v}$		$\vec{v}_1 = 0$
$\vec{w}_2 = \vec{w}$		$\vec{w}_1 = 0$

The same circumstances in the "steady discontinuity" frame appear as:

SIDE 2	SIDE 1
$\vec{v}_{n2} = \vec{C} - \vec{v}_n$	$\vec{v}_{n1} = \vec{C}$
$\vec{v}_{s2} = \vec{C} - \vec{v}_s$	$\vec{v}_{s1} = \vec{C}$
$\vec{v}_2 = \vec{C} - \vec{v}$	$\vec{v}_1 = \vec{C}$
$\vec{w}_2 = -\vec{w}$	$\vec{w}_1 = 0$

(20)

Let the thermodynamic functions and variables of side 1 have subscript o and those of side 2 have no subscript. Then:

$$\begin{aligned}
\rho_{s2} &= \rho_s & \rho_{s1} &= \rho_{so} \\
\rho_{n2} &= \rho_n & \rho_{n1} &= \rho_{no} \\
\rho_2 &= \tilde{\rho} & \rho_1 &= \rho_o \\
p_2 &= p & p_1 &= p_o \\
T_2 &= T & T_1 &= T_o \\
\Phi_2 &= \tilde{\Phi} & \Phi_1 &= \Phi_o \\
s_2 &= \tilde{s} & s_1 &= s_o
\end{aligned} \tag{21}$$

Using (20) and (21) in equations (9), (10), (11b) and (12), the jump conditions become:

$$\rho_o C = \tilde{\rho}(C-v) \tag{22}$$

$$p_o + \rho_o C^2 = p + \tilde{\rho}(C-v)^2 + \frac{\rho_s \rho_n}{\tilde{\rho}} w^2 \tag{23}$$

$$\Phi_o + \frac{C^2}{2} = \tilde{\Phi} + \tfrac{1}{2}\left[C - v + \frac{\rho_n}{\tilde{\rho}} w\right]^2 \tag{24}$$

$$\rho_o s_o T_o C = \tilde{\rho}\,\tilde{s}\,T\left[C - v - \frac{\rho_s}{\tilde{\rho}} w\right] - \rho_n w\left[C - v - \frac{\rho_s}{\tilde{\rho}} w\right]^2 \tag{25}$$

Using (22) it is possible to eliminate (C-v) from the remaining conditions. Similarly, equations (13), (18), and (19) can be used to eliminate $\tilde{\Phi}$, $\tilde{s}$, and $\tilde{\rho}$ respectively. Then to order w^2 (23), (24), and (25) take the form:

$$(p-p_o) - \frac{\rho_o C^2}{\rho}[\rho-\rho_o] + \rho_o w^2\left[\frac{\rho_s \rho_n}{\rho_o \rho} - \frac{\rho_o C^2}{2}\frac{\partial}{\partial p}\left(\frac{\rho_n}{\rho}\right)\right] = 0 \tag{26}$$

$$(\Phi - \Phi_o) - \tfrac{1}{2}\frac{C^2}{\rho^2}(\rho^2 - \rho_o^2) + \frac{\rho_o \rho_n}{\rho^2} C w - w^2\left[\frac{\rho_n \rho_s}{2\rho^2} + \frac{\rho_o^2 C^2}{2\rho}\frac{\partial}{\partial p}\left(\frac{\rho_n}{\rho}\right)\right] = 0 \tag{27}$$

$$\rho_o C[Ts - T_o s_o] - w\left[s\,T\,\rho_s + \frac{\rho_o^2}{\rho^2}\rho_n C^2\right] + \rho_o w^2 C\left[\frac{T}{2}\frac{\partial}{\partial T}\left(\frac{\rho_n}{\rho}\right) + 2\frac{\rho_s \rho_n}{\rho^2}\right] = 0 \tag{28}$$

Define ΔT as $(T - T_o)$ and Δp as $(p - p_o)$. Then expand ρ, ρ_n, ρ_s, Φ, and s in Taylor's series in p and T. The expansions of $\rho_n(p, T)$ and $\rho_s(p, T)$ are straightforward. For LHe II $\rho(p, T)$ has negligible dependence on temperature since the expansion coefficient $-\frac{1}{\rho}\left(\frac{\partial \rho}{\partial T}\right)_p$ is generally small. Hence:

$$\rho(p, T) \doteq \rho(p) = \rho_o + \left(\frac{\partial \rho}{\partial p}\right)_o \Delta p + \left(\frac{\partial^2 \rho}{\partial p^2}\right)_o \frac{\Delta p^2}{2} + O(\Delta p^3)$$

Neglecting the expansion coefficient for LHe also leads to a simplification in the Taylor's expansion for $s(p, T)$:

$$s(p, T) = s_o + \left(\frac{\partial s}{\partial p}\right)_T \Delta p + \left(\frac{\partial s}{\partial T}\right)_p \Delta T + \ldots$$

but

$$ds = \frac{1}{T}\, dh - \frac{1}{\rho T}\, dp$$

$$= \frac{1}{T}\left(\frac{\partial h}{\partial T}\right) dT + \frac{1}{T}\left[-\frac{1}{\rho} + \left(\frac{\partial h}{\partial p}\right)\right] dp$$

$$= \left(\frac{ds}{\partial T}\right) dT + \left(\frac{\partial s}{\partial p}\right) dp$$

(where h is the enthalpy/unit mass)

Hence

$$\frac{\partial^2 s}{\partial p\, \partial T} = \frac{\partial^2 s}{\partial T\, \partial p}$$

implies that

$$\frac{\partial}{\partial p}\left[\frac{1}{T}\left(\frac{\partial h}{\partial T}\right)\right] = \frac{\partial}{\partial T}\left[-\frac{1}{\rho T} + \frac{1}{T}\left(\frac{\partial h}{\partial p}\right)\right]$$

$$\frac{1}{T}\,\frac{\partial^2 h}{\partial T\, \partial p} = -\frac{1}{T^2}\left[-\frac{1}{\rho} + \left(\frac{\partial h}{\partial p}\right)\right] +$$

$$+ \frac{1}{T}\left[\frac{1}{\rho^2}\left(\frac{\partial \rho}{\partial T}\right) + \frac{\partial^2 h}{\partial p\, \partial T}\right]$$

Thus:

$$\left[-\frac{1}{\rho} + \frac{\partial h}{\partial p}\right] = \frac{\partial s}{\partial p} = \frac{T}{\rho^2}\left(\frac{\partial \rho}{\partial T}\right)$$

Therefore it is consistent to neglect the dependence of the entropy on pressure if the dependence of the density on temperature is neglected:

$$s(p, T) \doteq s(T) = s_o + \left(\frac{\partial s}{\partial T}\right)_o \Delta T +$$

$$+ \left(\frac{\partial^2 s}{\partial T^2}\right) \frac{\Delta T^2}{2} + O\left(\Delta T^3\right)$$

In the expansion of $\Phi(p, T)$:

$$\Phi(p, T) = \Phi_o + \left(\frac{\partial \Phi}{\partial p}\right)_o \Delta p + \left(\frac{\partial \Phi}{\partial T}\right)_o \Delta T + \left(\frac{\partial^2 \Phi}{\partial p^2}\right)_o \frac{\Delta p^2}{2} + \left(\frac{\partial \Phi}{\partial T^2}\right) \frac{\Delta T^2}{2} + O(\Delta p^3, \Delta T^3)$$

but note that equation (14) can be used to determine the coefficients in this equation. Thus:

$$\Phi(p, T) = \Phi_o + \left(\frac{1}{\rho_o}\right) \Delta p + (-s_o) \Delta T + \left[-\frac{1}{\rho_o^2} \left(\frac{\partial \rho}{\partial p}\right)_o\right] \frac{\Delta p^2}{2} + \left[-\left(\frac{\partial s}{\partial T}\right)_o\right] \frac{\Delta T^2}{2} + O(\Delta p^3, \Delta T^3)$$

Using these expansions, equations (26), (27), and (28) can be evaluated out to quadratic terms in Δp, ΔT, and w:

$$\Delta p\left[1 - C^2 \left(\frac{\partial \rho}{\partial p}\right)_o\right] + \Delta p^2\left[\frac{C^2}{\rho_o} \left(\frac{\partial \rho}{\partial p}\right)_o^2 - \frac{C^2}{2} \left(\frac{\partial^2 \rho}{\partial p^2}\right)_o\right] + w^2 \left[\frac{\rho_{so} \rho_{no}}{\rho_o} - \frac{\rho_o^2 C^2}{2} \frac{\partial}{\partial p} \left(\frac{\rho_n}{\rho}\right)_o\right] = 0 \qquad (29)$$

$$\Delta p\left[\frac{1}{\rho_o} - \frac{C^2}{\rho_o} \left(\frac{\partial \rho}{\partial p}\right)_o\right] + \Delta T[-s_o] + w\left[\frac{\rho_{no}}{\rho_o} C\right] + \Delta p^2\left[\frac{-1}{2\rho_o^2} \left(\frac{\partial \rho}{\partial p}\right)_o - \frac{C^2}{2\rho_o} \left(\frac{\partial^2 \rho}{\partial p^2}\right)_o + \frac{3C^2}{2\rho_o^2} \left(\frac{\partial \rho}{\partial p}\right)_o^2\right] + \Delta T^2\left[-\frac{1}{2} \left(\frac{\partial s}{\partial T}\right)_o\right] + w^2 \left[-\frac{\rho_{no} \rho_{so}}{2\rho_o^2} - \frac{\rho_o C^2}{2} \frac{\partial}{\partial p} \left(\frac{\rho_n}{\rho}\right)_o\right] + w \Delta p\left[\frac{C}{\rho_o} \left(\frac{\partial \rho_n}{\partial p}\right)_o - \frac{2 \rho_{no} C}{\rho_o^2} \left(\frac{\partial \rho}{\partial p}\right)_o\right] + w \Delta T\left[\frac{C}{\rho_o} \left(\frac{\partial \rho_n}{\partial T}\right)_o\right] = 0 \qquad (30)$$

$$\Delta T\left[\rho_o C s_o + \rho_o C T_o \left(\frac{\partial s}{\partial T}\right)_o\right] +$$

$$+ w\left[- T_o \rho_{so} s_o - \rho_{no} C^2\right] +$$

$$+ \Delta T^2\left[\frac{\rho_o C T_o}{2}\left(\frac{\partial^2 s}{\partial T^2}\right)_o + \rho_o C\left(\frac{\partial s}{\partial T}\right)_o\right] +$$

$$+ w^2\left[\frac{\rho_o C T_o}{2}\frac{\partial}{\partial T}\left(\frac{\rho_n}{\rho}\right)_o + \frac{2\rho_{so}\rho_{no}}{\rho_o} C\right] +$$

$$+ w\Delta p\left[2\frac{\rho_{no} C^2}{\rho_o}\left(\frac{\partial \rho}{\partial p}\right)_o +\right.$$

$$\left. - T_o s_o \left(\frac{\partial \rho_s}{\partial p}\right)_o - C^2\left(\frac{\partial \rho_n}{\partial p}\right)_o\right] +$$

$$+ w\Delta T\left[- T_o \rho_{so}\left(\frac{\partial s}{\partial T}\right)_o - T_o s_o\left(\frac{\partial \rho_s}{\partial T}\right)_o +\right.$$

$$\left. - C^2\left(\frac{\partial \rho_n}{\partial T}\right)_o - s_o \rho_{so}\right] = 0 \qquad (31)$$

(From this point the subscript "o" is dropped).

The jump conditions [equations (29), (30), and (31)] may now be linearized by dropping all quadratic terms.

From equation (29):

$$\Delta p\left[1 - C^2\left(\frac{\partial \rho}{\partial p}\right)\right] = 0 \qquad (32)$$

Hence for $\Delta p \neq 0$:

$$C^2 = C_{10}^2 = \left(\frac{\partial \rho}{\partial p}\right)^{-1} = \frac{\partial p}{\partial \rho} \qquad (33a)$$

or

$$C_{10} = \left(\frac{\partial p}{\partial \rho}\right)^{\frac{1}{2}} \qquad (33b)$$

This solution for the velocity corresponds to ordinary pressure or sound waves in LHe II and is denoted "first sound." For consistency in the three linearized equations, ΔT and w must be of higher order than Δp for first sound.

From equations (30) and (31):

$$\Delta p\left[\frac{1}{\rho} - \frac{C^2}{\rho}\left(\frac{\partial \rho}{\partial p}\right)\right] + \Delta T[-s] + w\left[\frac{\rho_n}{\rho} C\right] = 0 \tag{34}$$

$$\Delta T\left[\rho\, Cs + \rho C\, T\left(\frac{\partial s}{\partial T}\right)\right] + w\left[-Ts\,\rho_s - C^2 \rho_n\right] = 0 \tag{35}$$

If Δp is negligible with respect to ΔT and w in these last two equations then it is possible to solve for another velocity when $\Delta T \neq 0$ and $w \neq 0$:

$$C_{20}^2 = \left(\frac{\rho_s}{\rho_n}\right) s^2 \left(\frac{\partial s}{\partial T}\right)^{-1} = \left(\frac{\rho_s}{\rho_n}\right) s^2 \left(\frac{\partial T}{\partial s}\right) \tag{36a}$$

or

$$C_{20} = \left(\frac{\rho_s}{\rho_n}\right)^{\frac{1}{2}} s \left(\frac{\partial T}{\partial s}\right)^{\frac{1}{2}} \tag{36b}$$

Using this velocity in equation (34) (dropping the Δp term) there is a relationship between w and ΔT which corresponds to equation (36):

$$w = \left[\left(\frac{\rho}{\rho_n}\right) \frac{s}{C_{20}}\right] \Delta T \tag{37}$$

This velocity solution (C_{20}) is unique to LHe II and the corresponding propagation of temperature or relative velocity is denoted "second sound." All three linearized equations are consistent for second sound if Δp is of higher order than w or ΔT.

D.1. Pressure Discontinuities

In equation (29) neglect w^2 with respect to Δp and Δp^2. Then (29) is approximately:

$$\Delta p\left[1 - C^2\left(\frac{\partial \rho}{\partial p}\right)\right] + \Delta p^2\left[\frac{C^2}{\rho}\left(\frac{\partial \rho}{\partial p}\right)^2 - \frac{C^2}{2}\left(\frac{\partial^2 \rho}{\partial p^2}\right)\right] = 0$$

Hence
$$C_1^2 = \frac{1}{\left(\frac{\partial \rho}{\partial p}\right) - \Delta p\left[\frac{1}{\rho}\left(\frac{\partial \rho}{\partial p}\right)^2 - \frac{1}{2}\left(\frac{\partial^2 \rho}{\partial p^2}\right)\right]}$$

Consistent to order Δp:

$$C_1^2 = C_{10}^2\left\{1 + \Delta p\left[\frac{1}{\rho}\frac{\partial \rho}{\partial p} - \frac{1}{2}C_{10}^2\frac{\partial}{\partial p}\left(\frac{1}{C_{10}^2}\right)\right]\right\} \tag{38}$$

where C_{10}^2 is defined in equation (33a). Equation (38) is equivalent to:

$$C_1^2 = C_{10}^2\left[1 + \Delta p\frac{\partial}{\partial p}\ell n(\rho C_{10})\right] \tag{39}$$

It is possible to eliminate Δp from the correction term by making the acoustic approximation (momentum balance):

$$\Delta p \doteq \rho C_{10} v$$

Then equation (39) becomes:

$$C_1^2 = C_{10}^2\left[1 + v\frac{\partial}{\partial p}(\rho C_{10})\right] \tag{40a}$$

or

$$C_1 = C_{10}\left[1 + \frac{v}{2}\frac{\partial}{\partial p}(\rho C_{10})\right] \tag{40b}$$

Using equation (39) for C in the jump conditions it is possible to verify that for first sound w and ΔT are of higher order than Δp (w and $\Delta T \sim O(\Delta p^3)$).

D.2. Temperature Discontinuities

Assume that Δp is of higher order than w and ΔT in the jump conditions. Then from equation (29):

$$\Delta p = \frac{-\left[\frac{\rho_s \rho_n}{\rho} - \frac{\rho^2 C^2}{2} \frac{\partial}{\partial p}\left(\frac{\rho_n}{\rho}\right)\right]}{\left[1 - C^2\left(\frac{\partial \rho}{\partial p}\right)\right]} w^2 \qquad (41)$$

Substituting this value of Δp into equations (30) and (31) there are two equations for w, ΔT, and C. Eliminating w from these two equations results in a single equation relating C_2 and ΔT (valid to order ΔT^2):

$$\left(-\frac{3}{2}\frac{\rho_n \rho_s}{\rho^2}\right)\left(-T\frac{\rho_n}{2\rho}\right)\left(3\frac{\rho_s^2}{\rho} sT - \frac{\rho_n \rho_s}{\rho} C^2 - C^2 T \frac{\partial \rho_n}{\partial T}\right) \cdot$$

$$\cdot \left[\left(-s^2 \rho_s + \rho_n C^2 \frac{\partial s}{\partial T}\right) \Delta T + \right.$$

$$\left. + (s\rho_s)\left(\frac{s}{2} \frac{\partial T}{\partial s} \frac{\partial^2 s}{\partial T^2} - 3\frac{\partial s}{\partial T} + \frac{3}{2} \frac{\rho s}{\rho_s \rho_n} \frac{\partial \rho_n}{\partial T}\right) \Delta T^2\right] = 0 \qquad (42)$$

where the approximations $C \doteq C_{20}$ and $\frac{\partial \rho}{\partial T} = \frac{\partial \rho_s}{\partial T} + \frac{\partial \rho_n}{\partial T} \doteq 0$ have been made in determining the ΔT^2 coefficient. From (42) it can be shown that <u>if</u>:

$$\rho_n \neq 0, \text{ and } \rho_s \neq 0, \text{ and } T \neq 0 ,$$

and

$$C^2 \neq \frac{3 \rho_s^2 s T}{\rho_n \rho_s + \rho T\left(\frac{\partial \rho_n}{\partial T}\right)}$$

<u>then</u> to order ΔT^2:

$$\left[- s^2 \rho_s + \rho_n C^2 \left(\frac{\partial s}{\partial T}\right) \right] +$$

$$+ (s\rho_s)\left[\frac{s}{2}\left(\frac{\partial T}{\partial s}\right)\left(\frac{\partial^2 s}{\partial T^2}\right) - 3\left(\frac{\partial s}{\partial T}\right) + \frac{3}{2}\frac{\rho s}{\rho_n \rho_s}\left(\frac{\partial \rho_n}{\partial T}\right)\right] \Delta T = 0$$

Hence:

$$C_2^2 = C_{20}^2 \left\{1 + \Delta T\left[-\frac{1}{2}\left(\frac{\partial T}{\partial s}\right)\left(\frac{\partial^2 s}{\partial T^2}\right) + \right.\right.$$

$$\left.\left. + \frac{3}{2}\left(\frac{\partial s}{\partial T}\right) - \frac{3}{2}\frac{\rho}{\rho_n \rho_s}\left(\frac{\partial \rho_n}{\partial T}\right)\right]\right\} \qquad (43)$$

where C_{20} is given by equation (36b). Equation (43) is equivalent to:

$$C_2^2 = C_{20}^2\left[1 + \Delta T \frac{\partial}{\partial T} \ell n \left(C_{20}^3 \frac{\partial s}{\partial T}\right)\right] \qquad (44a)$$

or

$$C_2 = C_{20}\left[1 + \frac{\Delta T}{2} \frac{\partial}{\partial T} \ell n \left(C_{20}^3 \frac{\partial s}{\partial T}\right)\right] \qquad (44b)$$

It is consistent to replace ΔT in the correction term of (44b) by the corresponding w term found in equation (37):

$$C_2 = C_{20}\left[1 + \frac{w}{2} \frac{\rho_n}{\rho} \frac{C_{20}}{s} \frac{\partial}{\partial T} \ell n \left(C_{20}^3 \frac{\partial s}{\partial T}\right)\right] \qquad (44c)$$

APPENDIX E

FLOW FIELD CALCULATIONS

It is possible to calculate the flow field values created when a gasdynamic shock wave reflects from a liquid. The analysis presented here is restricted by the following assumptions:

a) the flow field is one-dimensional

b) the gas is ideal

c) the pressure discontinuities of the liquid are governed by the equations of Khalatnikov

d) first sound waves are not affected by second sound waves

e) the effects of condensation, evaporation, and gas density gradients at the liquid-gas interface are neglected

f) dissipative mechanisms are neglected .

The notation indicated in Figure 38 will be used. The region number is the subscript for the variables and velocities within that region (first and second sound velocities use subscripts 1 and 2 respectively).

The strength of the incident shock wave is used as input to the calculations. Consequently the flow field in regions 0, 1, and 2 is known.

E. 1. Reflected Gas Shock and Incident First Sound

The jump conditions for the reflected shock are

$$\rho_2 [U_R + u_2] = \rho_5 [U_R + u_5]$$

$$p_5 - p_2 = \rho_2 [U_R + u_2][u_2 - u_5]$$

$$h_5 - h_2 = U_R (u_2 - u_5) + \tfrac{1}{2}(u_2^2 - u_5^2)$$

For an ideal gas $p_5 = \rho_5 R T_5$

and $h_5 = C_p T_5$

The conservation of mass and momentum across the incident first sound wave can be expressed as

$$\rho_6 [C_1(0) - v_6] = \rho_o [C_1(0)]$$

$$\Delta p_I = p_6 - p_o = \rho_o [C_1(0)][v_6]$$

Applying the results of Khalatnikov for a pressure discontinuity

$$C_1(0) = C_{10}(0)\left[1 + \tfrac{1}{2} \Delta p_I \frac{\partial}{\partial p} \ell n (\rho C_{10})\right]$$

where $C_{10}(0) = C_{10}(p_o, T_o)$

The boundary conditions at the liquid-gas interface require that:

$$u_5 = v_6 = \text{interface velocity}$$

and $p_5 = p_6$.

There are now eight equations for the eight unknowns: U_R, ρ_5, u_5, p_5, h_5, T_5, ρ_6, and $C_1(0)$. The system can be solved in this form after a great deal of algebra. A simpler approach can be followed with an iterative scheme. Solve the reflected shock with $u_5 = 0$. The calculated p_5 can be used with the liquid equations to determine u_5. This value of u_5 can then be used to calculate new gas values. This iteration produces rapidly converging flow field values.

E.2. The Contact Surface-Reflected Shock Interaction

When the reflected shock meets the contact surface a shock wave is transmitted through the contact surface (Fig. 44). The wave which is reflected from this interaction can be either a shock wave or an expansion fan. To determine the nature of this reflected wave a calculation of the transmitted shock is made assuming that the velocity behind this shock is u_5. The calculated pressure behind the shock p_T is compared to p_5. If $p_T/p_5 = 1$ no wave is reflected; if $p_T/p_5 < 1$ the reflected wave is an expansion; if $p_T/p_5 > 1$ the reflected wave is a shock. Once the nature of the reflected wave is known, the proper equations can be used and the system solved for all flow quantities. The boundary conditions at the contact surface require continuity of the particle velocity and the pressure.

E. 3. Reflected First Sound

The first sound wave reflects off a solid end wall. The boundary condition at the wall requires that v_7 vanish. Consequently the mass and momentum conservation equations can be written as

$$\rho_7 [C_1(6)] = \rho_6 [C_1(6) + u_5]$$

$$\Delta p_R = p_7 - p_6 = \rho_6 [C_1(6) + u_5][u_5]$$

The Khalatnikov first sound velocity becomes

$$C_1(6) = C_{10}(6)\left[1 + \tfrac{1}{2} \Delta p_R \frac{\partial}{\partial p} \ell n(\rho C_{10})\right]$$

where

$$C_{10}(6) = C_{10}(p_6, T_6) \doteq C_{10}(p_6, T_o)$$

These three equations allow a solution for the three unknowns: ρ_7, $C_1(6)$, and p_7.

E.4. Rereflected First Sound and the Transmitted Gas Shock

When the reflected first sound wave reaches the liquid free surface an unusual situation occurs. The liquid pressure is more than twice that of the gas. Consequently a shock wave is transmitted into the gas, a centered expansion fan travels back into the liquid, and the free surface moves away from the end wall. This is directly analogous to the ideal shock tube: the gas acts as the low pressure test gas, the liquid as the high pressure driver gas, and the free surface as the massless piston.

The conservation equations for the transmitted gas shock are

$$\rho_5[U_T + u_5] = \rho_9[U_T - u_9]$$

$$p_9 - p_5 = \rho_5[U_T + u_5][u_5 + u_9]$$

$$h_9 - h_5 = U_T[u_5 + u_9] + \tfrac{1}{2}[u_5^2 - u_9^2]$$

For an ideal gas

$$h_9 = C_p T_9$$

and

$$p_9 = \rho_9 R T_9$$

The leading characteristic of the rereflected first sound wave moves with the acoustic velocity of region 7, hence $C_1(7) = C_{10}(7)$. The velocity of the trailing characteristic is $C_1(8') = C_{10}(8) - v_8$. As before $C_{10}(7) = C_{10}(p_7, T_7) \doteq C_{10}(p_7, T_o)$ and $C_{10}(8) = C_{10}(p_8, T_8) \doteq C_{10}(p_8, T_o)$.

Along a characteristic which traverses the expansion fan

$$\frac{dp}{dv} = - \rho C_{10}$$

Consequently

$$\int_7^8 \frac{d p}{\rho(p) C_{10}(p)} = -\int_7^8 dv = -v_8$$

If the equation of state of the liquid is known, it is possible to evaluate this integral analytically or numerically.

As seen in Figures 28 and 29 a good approximation for LHe is that

$$\rho(p) \doteq \alpha_1 + \beta_1 p$$

$$C_{10}(p) \doteq \alpha_2 + \beta_2 p$$

where $\alpha_1, \alpha_2, \beta_1$, and β_2 are constants. Using these expressions the integral can be solved exactly giving a very good approximation for v_8.

A simpler approach is to estimate v_8 as

$$v_8 \doteq \frac{p_7 - p_8}{\rho_7 C_{10}(7)} \doteq \frac{p_7 - p_5}{\rho_7 C_{10}(7)}$$

The boundary conditions at the gas-liquid interface require

$$u_9 = v_8 = \text{interface velocity}$$

and

$$p_9 = p_8$$

Using the approximate value of v_8 the gas equations can be solved and p_8 calculated. This value of p_8 can be used in place of p_5 to obtain a better value of v_8. Accurate flow field values can be calculated this way in two iterations.

E. 5. The Second Sound Waves

In order to simplify the calculations it is desirable to treat the second sound waves as waves of infinitesimal amplitude. The data can then be compared to the computed wave lines to determine whether the observed waves move faster or slower.

The velocity of second sound is a function of pressure (Fig. 30) and consequently the wave velocity in region n is approximated as

$$C_{20}(n) \equiv C_{20}(p_n, T_n) \doteq C_{20}(p_n, T_o)$$

The values of $C_{20}(p_n, T_o)$ are taken from Reference 54.

It is important to consider the particle velocities given to the liquid by the first sound waves. These velocities are not small compared to the velocity of second sound. They must be added as vectors to the second sound velocity in the region. Hence

$$C_2(n) = C_{20}(p_n, T_o) \pm v_n .$$

E.6. The First Sound-Second Sound Interaction

Dessler (Ref. 48) has considered the interaction of first and second sound in LHe II. Another approach is presented here.

Consider a second sound wave which collides with a large amplitude first sound (compression) wave. Let the subscripts I, R, and T denote quantities pertaining to the incident, reflected, and transmitted second sound waves. The subscripts 1 and 2 refer to first and second sound. Let C and v denote wave and particle velocities. C_h is the specific heat of the liquid. The problem is treated as one-dimensional.

Assume that the first sound wave: (a) is unaffected by the interaction and (b) does not create or destroy heat energy. If the total heat of the incident wave is conserved then

$$Q_I = Q_R + Q_T$$

or

$$\Delta T_I[\rho_I C_{hI}(C_{2I} + v)] = \Delta T_R[\rho_R C_{hR}(C_{2R} - v)] +$$

$$+ \Delta T_T[\rho_T C_{hT}(C_{2T} + v)]$$

If, in addition, the heat flux of the incident wave is conserved, then

$$q_I = q_R + q_T$$

or

$$\rho_I C_{hI} C_{2I} \Delta T_I = \rho_R C_{hR} C_{2R} \Delta T_R + \rho_T C_{hT} C_{2T} \Delta T_T$$

Assume that

$$\rho_R \doteq \rho_T \doteq \rho_I\left(1 + \frac{\Delta\rho}{\rho}\right)$$

$$C_{hR} \doteq C_{hT} \doteq C_{hI}\left(1 + \frac{\Delta C_h}{C_h}\right)$$

$$C_{2I} = C_2$$

$$C_{2R} = C_2' + v$$

$$C_{2T} = C_2'' - v$$

$$C_2' \doteq C_2'' \doteq C_2\left(1 + \frac{\Delta C_2}{C_2}\right)$$

where $\Delta\rho$, ΔC_h, and ΔC_2 are small changes due to the pressure jump across the first sound wave. If

$$R \equiv \frac{\Delta T_R}{\Delta T_I}$$

and

$$T \equiv \frac{\Delta T_T}{\Delta T_I}$$

then it is possible to show that

$$T = \left(1 + \tfrac{1}{2}\frac{v}{C_2}\right)\left[1 + \frac{\Delta\rho}{\rho} + \frac{\Delta C_h}{C_h} + \frac{\Delta C_2}{C_2}\right]^{-1}$$

$$R = \left(\tfrac{1}{2}\frac{v}{C_2}\right)\left[1 + \frac{\Delta\rho}{\rho} + \frac{\Delta C_h}{C_h} + \frac{\Delta C_2}{C_2}\right]^{-1}$$

$$Q_T = \left[\frac{1 + \tfrac{1}{2}\frac{v}{C_2}}{1 + \frac{v}{C_2}}\right] Q_I$$

$$Q_R = \left[\frac{\tfrac{1}{2}\frac{v}{C_2}}{1 + \frac{v}{C_2}}\right] Q_I$$

$$q_T = (1 + \frac{1}{2}\frac{v}{C_2})(1 - \frac{v}{C_2})q_I$$

$$q_R = (1 + \frac{v}{C_2})(\frac{1}{2}\frac{v}{C_2})q_I$$

Since $C_1 > C_2 + v$ both the transmitted and reflected waves will propagate <u>behind</u> the first sound wave. The reflected wave is reflected in the sense that it travels back into the fluid through which the incident wave passed. The transmitted wave moves through new fluid. In laboratory coordinates both waves will move in the same direction if $v > C_2$.

In the $p_1 = 3$ torr case v/C_2 is roughly 1/2 for the incident second sound-reflected first sound interaction. With the proper values of $\frac{\Delta\rho}{\rho}$, $\frac{\Delta C_h}{C_h}$, and $\frac{\Delta C_2}{C_2}$ for the pressure jump it follows that

$$T = 1.1$$

and

$$R = .24$$

REFERENCES

1. Vielle, M. P., Comptes Rendus de L'Academie des Sciences 129, 1228 (1899).
2. Warren, W. R., and Harris, C. J., Proc. 7th Int. Shock Tube Symposium, Univ. of Toronto, Toronto, Canada (June 1969).
3. Bennett, F. D., Aero. Eng. Rev., Oct. 1957, pp. 63-8.
4. Goodyer, M. J., and Kilgore, R. A., paper presented at the AIAA 7th Aerodynamic Testing Conference, Palo Alto, Calif., Sept. 13-15, 1972.
5. Yoder, M. J., Ph. D. Thesis, University of Michigan (1971).
6. Rupert, V. C., Ph. D. Thesis, California Institute of Technology (1972).
7. Liepmann, H. W., Cummings, J. C., and Rupert, V. C., Phys. Fluids 16, 332 (1973).
8. Bowman, R. M., Ph. D. Thesis, California Institute of Technology (1966).
9. Duff, R. E., Phys. Fluids 2, 207 (1959).
10. Glass, I. I., and Patterson, G. N., J. Aeronaut. Sci., 22, 73 (1955).
11. Roshko, A., Phys. Fluids 3, 835 (1960).
12. Mirels, H., Phys. Fluids 6, 1201 (1963).
13. Mirels, H., AIAA J. 2, 84 (1964).
14. Arave, R. J., Boeing Report No. D2-22291 (1963).

REFERENCES (Cont'd)

15. Hirschfelder, J. O., Curtiss, C. F., and Bird, R. B., Molecular Theory of Gases and Liquids, John Wiley and Sons, Inc., New York (1964).

16. The "1958 He^4 Scale of Temperatures", N.B.S. Monograph 10 (1960).

17. White, G. K., Experimental Techniques in Low Temperature Physics, John Wright and Sons Ltd., Bristol (1968).

18. Dimotakis, P. E., Ph. D. Thesis, California Institute of Technology (1972).

19. A Compendium of Properties of Materials at Low Temperature, edited by V. J. Johnson and R. B. Stewart, WADD Tech. Report No. 60-56 (1960-1).

20. White, D. R., J. Fluid Mech. 4, 585 (1958).

21. Roshko, A., and Smith, J. A., AIAA J. 2, 186 (1964).

22. Hartunian, R. A., Russo, A. L., Marrone, P. V., C.A.L. Report No. AD-1118-A-3 (1959).

23. Liepmann, H. W., and Fila, G. H., NACA Tech. Report No. 890 (1947).

24. Sturtevant, B., and Okamura, T. T., Phys. Fluids 12, 1723 (1969).

25. Clement, J. R., and Quinell, E. H., Rev. Sci. Instr. 23, 213 (1952).

26. Schulte, E. H., Cryogenics 6, 321 (1966).

27. Van Itterbeek, A., et al., Physica 19, 1158 (1953).

28. Coremans, J. M. J., et al., Physica 24, 557 (1958).

REFERENCES (Cont' d)

29. Becker, E. W., et al., Z. Phys. 137, 126 (1954).

30. Thermophysical Properties of Matter, edited by Y. S. Touloukian and C. Y. Ho, Plenum Press (1970).

31. London, F., Nature 141, 643 (1938); Physics Rev. 54, 947 (1938).

32. Tisza, L., Nature 141, 913 (1938).

33. Landau, L., J. Phys. USSR 5, 71 (1941).

34. Landau, L., J. Phys. USSR 11, 91 (1947).

35. Onsager, L., Il Nuovo Cimento 6, Suppl. 2, 249 (1949).

36. Feynman , R. P., Progress in Low Temperature Physics, edited by C. J. Gorter, Amsterdam: North Holland Publishing Co. (1955).

37. Khalatnikov, I. M., Zh. Eksp. Teor. Fiz. 23, 253 (1952).

38. Khalatnikov, I. M., Introduction to the Theory of Superfluidity, translated by Pierre C. Hohenberg, W. A. Benjamin, Inc., New York (1965).

39. Osborne, D. V., Proc. Phys. Soc. (London) A64, 114 (1951).

40. Dessler, A. J., and Fairbank, W. M., Phys. Rev. 104, 6 (1956).

41. Gulyaev, A. I., Zh. Eksp. Teor. Fiz. 57, 59 (1969).

42 Gulyaev, A. I., Zh. Eksp. Teor. Fiz. Pis. Red 11, 332 (1970).

43. Preshkov, V. P., Vetchinkin, A. N., and Elkonin, B. V., Cryogenics 9, 133 (1969).

REFERENCES (Cont' d)

44. Blair, D. G., and Matheson, C. C., Cryogenics 10, 513 (1970).

45. Van Itterbeek, A., and De Laet, W., Physica 24, 59 (1958).

46. Sturtevant, B., and Slachmuylders, E., Phys. Fluids 7, 1201 (1964).

47. Cole, R. H., Underwater Explosions, Princeton University Press, Princeton, New Jersey (1948).

48. Dessler, A. J., Phys. Fluids 2, 5 (1959).

49. Landau, L. D., and Lifshitz, E. M., Fluid Mechanics, Pergamon Press (1959).

50. Jacucci, G., and Signorelli, Phys. Letters 26A, 5 (1967).

51. Hofman, A., Keck, K., and Schubert, G. V., Z. Physik 231, 177 (1970).

52. Fritz, G. F., and Pollack, G. L., Phys. Rev. A. 2, 2560 (1970).

53. Kapitza, P. L., J. Phys., Moscow 4, 181 (1941).

54. Maurer, R. D., and Herlin, M. A., Phys. Rev. 81, 444 (1951).

Test gas: helium Driver gas: helium T_4: 300°K

T_1 (°K)	p_1 (torr)	Diaphragm Pressure Ratio	Observed $\overline{U}_s \pm$ R. M. S. (m/sec)	Ideal U_s (m/sec)	$\frac{\overline{U}_{s_{obs}}}{U_{s_{ideal}}}$	$\overline{M}_{s_{obs}}$	No. of Data Runs
300	25	3.3×10^1	1716	1920	.89	1.69	1
300	9.0	7.0×10^1	1952	2135	.91	1.92	3
300	5.0	1.3×10^2	2109	2320	.91	2.08	1
300	3.0	2.6×10^2	2160	2500	.86	2.13	1
300	1.0	7.2×10^2	2318	2760	.84	2.28	2
300	0.3	2.6×10^3	2420	3005	.81	2.38	1
77	9.0	1.3×10^2	1598 ± 18	1662	.96	3.09	9
77	3.0	3.8×10^2	1892 ± 7	1988	.95	3.66	5
77	1.0	1.1×10^3	2150 ± 22	2300	.93	4.16	8
77	0.5	2.3×10^3	2243 ± 21	2484	.90	4.34	3
77	0.1	1.1×10^4	2443 ± 29	2845	.86	4.73	7
77	.05	2.3×10^4	2544 ± 34	3007	.85	4.92	4
77	.01	1.1×10^5	2643 ± 88	3287	.80	5.11	6

Table 1. Comparison of Observed Shock Wave Velocities with Theoretical Predictions

T_1 (^oK)	p_1 (torr)	Diaphragm Pressure Ratio	Observed $\bar{U}_s \pm$ R. M. S. (m/sec)	Ideal U_s (m/sec)	$\frac{\bar{U}_{s_{obs}}}{U_{s_{ideal}}}$	$\bar{M}_{s_{obs}}$	No. of Data Runs
4.2	5.0	2.5×10^2	856 ± 19	918	.93	7.11	14
4.2	1.0	1.3×10^3	1370 ± 41	1387	.99	11.4	21
4.2	0.5	2.5×10^3	1579 ± 20	1590	.99	13.1	12
4.2	0.3	4.2×10^3	1752 ± 19	1761	.99	14.6	4
4.2	0.1	1.3×10^4	2021 ± 60	2073	.97	16.8	12
4.2	.05	2.5×10^4	2186 ± 44	2267	.96	18.2	15
4.2	.03	4.2×10^4	2311 ± 67	2404	.96	19.2	4
4.2	.01	1.3×10^5	2499 ± 44	2677	.93	20.7	13
2.3	3.0	4.5×10^2	872 ± 13	907	.96	9.78	8
2.3	0.5	2.7×10^3	1454 ± 30	1426	1.02	16.3	11
2.3	0.1	1.3×10^4	1939 ± 39	1911	1.01	21.7	12
2.3	.01	1.3×10^5	2538 ± 28	2544	1.00	28.5	8
2.3	.003	4.5×10^5	2875 ± 85	2821	1.02	32.2	15
1.46	.0015	9.7×10^5	2907 ± 40	2887	1.01	40.4	2

Table 1. (cont'd)

Table 2. Modified Mirel's Criterion for Boundary Layer Transition

Mirel's Criterion: $dp_1 \leq .5$ LBL

$dp_1 \sim 1.5$ Transition

$dp_1 \geq 5$ TBL

Modified Criterion: $\alpha dp_1 \leq .5$ LBL

$\alpha dp_1 \sim 1.5$ Transition

$\alpha dp_1 \geq 5$ TBL

where $\alpha \equiv \left(\frac{\rho_1}{\rho_o}\right)\left(\frac{a_1}{a_o}\right)\left(\frac{\mu_o}{\mu_1}\right) \doteq \left(\frac{T_o}{T_1}\right)^{1.1}$

d = shock tube diameter in inches

p_1 = test pressure in centimeters of mercury

subscript o: room temperature

subscript 1: test gas temperature

T_1 (°K)	Transition p_1 (torr)	LBL p_1 (torr)	TBL p_1 (torr)
300	15	5	50
77	3.4	1.1	11
4.2	1.4	.05	.46
2.3	.07	.02	.24

Table 3. Calculated Wall Temperatures for a Laminar Boundary Layer

T_1 (°K)	p_1 (torr)	T_w (°K)
4.2	5.0	7.2
"	1.0	9.6
"	0.3	9.6
"	0.1	8.2
"	.03	8.0
"	.01	6.6
2.3	3.0	5.7
"	0.5	7.5
"	0.1	7.7
"	.01	5.7
"	.003	5.0

Table 4. Maximum Separation Distance Between Shock Wave and Contact Surface

T_1 (°K)	T_w (°K)	p_1 (torr)	LBL ℓ_m (cm)	TBL ℓ_m (cm)
298	298	9.0	60.4	43.6
"	"	5.0	31.8	31.3
"	"	3.0	18.4	26.5
"	"	2.0	11.6	22.6
"	"	1.0	5.7	17.8
"	"	0.5	2.9	14.4
"	"	0.3	1.7	12.4
77.2	77.2	9.0	183	26.6
"	"	3.0	54.8	18.1
"	"	1.0	17.5	14.2
"	"	0.5	8.5	11.8
"	"	0.1	1.6	7.2
"	"	.05	.8	6.0
"	"	.01	.2	3.9
4.2	4.2	5.0	2343	40.3
"	"	1.0	384	22.4
"	"	0.3	96.6	17.0
"	"	0.1	30.4	11.7
"	"	.05	15.2	10.0
"	"	.03	9.5	9.8
"	"	.01	2.9	6.5
4.2	5.5	5.0	1380	35.4
"	"	1.0	226	19.7
"	"	0.3	57.1	14.8
"	"	0.1	17.9	10.2
"	"	.05	9.0	8.8
"	"	.03	5.6	8.6
"	"	.01	1.7	5.7

Table 4. (Cont'd)

T_l (°K)	T_w (°K)	p_l (torr)	LBL ℓ_m (cm)	TBL ℓ_m (cm)
4.2	10.0	5.0	476	27.1
"	"	1.0	78	15.1
"	"	0.3	19.7	11.4
"	"	0.1	6.2	7.9
"	"	.05	3.1	6.8
"	"	.03	1.9	6.6
"	"	.01	.6	4.4
2.3	2.3	3.0	3229	44.3
"	"	0.5	388	23.1
"	"	0.1	69.1	13.4
"	"	.01	5.3	7.8
"	"	.003	1.4	4.6
2.3	4.2	3.0	967	32.7
"	"	0.5	116	17.1
"	"	0.1	20.7	10.0
"	"	.01	1.6	5.7
"	"	.003	.4	3.4
2.3	5.5	3.0	570	28.7
"	"	0.5	68.3	14.9
"	"	0.1	12.2	8.7
"	"	.01	.9	5.0
"	"	.003	.2	3.0
2.3	10.0	3.0	197	22.0
"	"	0.5	23.6	11.5
"	"	0.1	4.2	6.7
"	"	.01	.3	3.9
"	"	.003	.1	2.3

Table 5. Comparison of Observed Incident Shock Velocities with Theoretical Predictions

Observed values are based on a first order polynomial fit to the (χ, τ) data.

T_1 (°K)	2.26	2.02	1.91	1.71	1.46
p_1 (torr)	47	25	18	9	3
p_4/p_1	36	67	93	187	560
Observed $\overline{U}_s$ (m/sec)	316	377	415	552	756
$\overline{U}_{s_{obs}}/U_{s_{ideal}}$	.85	.83	.82	.88	.92
Observed $\overline{M}_s$	3.7	4.6	5.1	7.2	10.6
Number of (χ, τ) values	88	14	51	31	106
τ value at $\chi = 0$	.09	-.11	-.67	-.60	-.03
R.M.S. τ deviation	±3.4	±0.6	±0.9	±0.7	±0.9

Table 6. Theoretical Flow Field Values

(Calculated with the Observed $\overline{M}_s$)

$T_1 \doteq T_o$	(^oK)	2.26	2.02	1.91	1.71	1.46
$p_1 \doteq p_o$	(torr)	47	25	18	9	3
$p_5 = p_6$	(atm.)	4.4	4.2	3.6	3.7	3.5
p_7	(atm.)	9.4	8.9	7.6	7.8	7.4
$p_8 = p_9$	(atm.)	5.0	4.6	3.9	4.0	3.7
T_2	(^oK)	12	14	15	24	44
T_5	(^oK)	24	32	35	57	120
U_R	(m/sec)	160	184	198	248	361
U_T	(m/sec)	290	334	348	447	648
$u_5 = v_6$	(m/sec)	12.0	11.5	10.1	10.3	9.9
$v_8 = u_9$	(m/sec)	9.6	9.6	8.6	9.0	8.9
$C_1(0)$	(m/sec)	244	247	248	251	252
$C_1(6)$	(m/sec)	265	265	262	266	265
$C_1(7)$	(m/sec)	291	286	282	286	285
$C_1(8')$	(m/sec)	251	252	250	254	255
$C_2(6)$	(m/sec)	-	25.8	27.6	29.9	29.2
$C_2(7)$	(m/sec)	-	~9	15.8	18.5	18.6
$C_2(8)$	(m/sec)	-	~4	8.8	10.5	10.4

Table 7. Comparison of Observed Flow Velocities with Theoretical Predictions

Observed values are based on a first order polynomial fit to the (χ,τ) data.

$T_1 \doteq T_o$	(^oK)	2.26	2.02	1.91	1.71	1.46
$p_1 \doteq p_o$	(torr)	47	25	18	9	3
$\overline{U}_R$ Observed	(m/sec)	187	208	246	290	363*
	$\frac{\overline{U}_{R_{obs}}}{\overline{U}_{R_{ideal}}}$	1.17	1.13	1.24	1.09	1.01
	τ value at $\chi = 0$	.96	-.11	.98	.50	-.24
	R. M. S. τ deviation	±5.4	±0.7	±2.0	±1.6	±1.0
	No. of (χ,τ) values	56	10	42	28	34
$\overline{C}_1(0)$ Observed	(m/sec)	254	264	263	258	$\frac{268}{266}$**
	$\frac{\overline{C}_{1(0)_{obs}}}{\overline{C}_{1(0)_{ideal}}}$	1.04	1.07	1.06	1.02	$\frac{1.06}{1.06}$
	τ value at $\chi = 0$	.72	.47	.22	.14	$\frac{-.02}{.59}$
	R. M. S. τ deviation	±1.7	±0.4	±1.3	±0.7	$\frac{\pm 0.7}{\pm 0.9}$
	No. of (χ,τ) values	73	8	42	50	$\frac{18}{111}$

*Using only those (χ,τ) data for which $\chi \geq -.7$ (see Fig. 44)

**Upper values represent results from the side mounted detectors; lower values correspond to results from the top mounted detectors

Table 7. (cont'd)

$T_1 \doteq T_o$ (°K)	1.91	1.71	1.46	
$p_1 \doteq p_o$ (torr)	18	9	3	
	data from both types of detectors		side mounted detector data	top mounted detector data
$\overline{C}_2(6)$ Observed (m/sec)	34.3	38.0	28.8	39.1
$\frac{\overline{C}_2(6)_{obs}}{\overline{C}_2(6)_{ideal}}$	1.24	1.27	.99	1.34
τ value at $\chi = 0$	+14	+9	-3	+11
R. M. S. τ deviation	±10	±8	±2	±7
No. of (χ, τ) values	29	24	10	73
$\overline{C}_2(8)$ Observed (m/sec)	26.7	53.2	2.3	61.3
$\frac{\overline{C}_2(8)_{obs}}{\overline{C}_2(8)_{ideal}}$	3.04	5.06	.23	5.90
τ value at $\chi = 0$	+18	+40	-890	+57
R. M. S. τ deviation	±6	±9	±1	±14
No. of (χ, τ) values	7	8	3	15

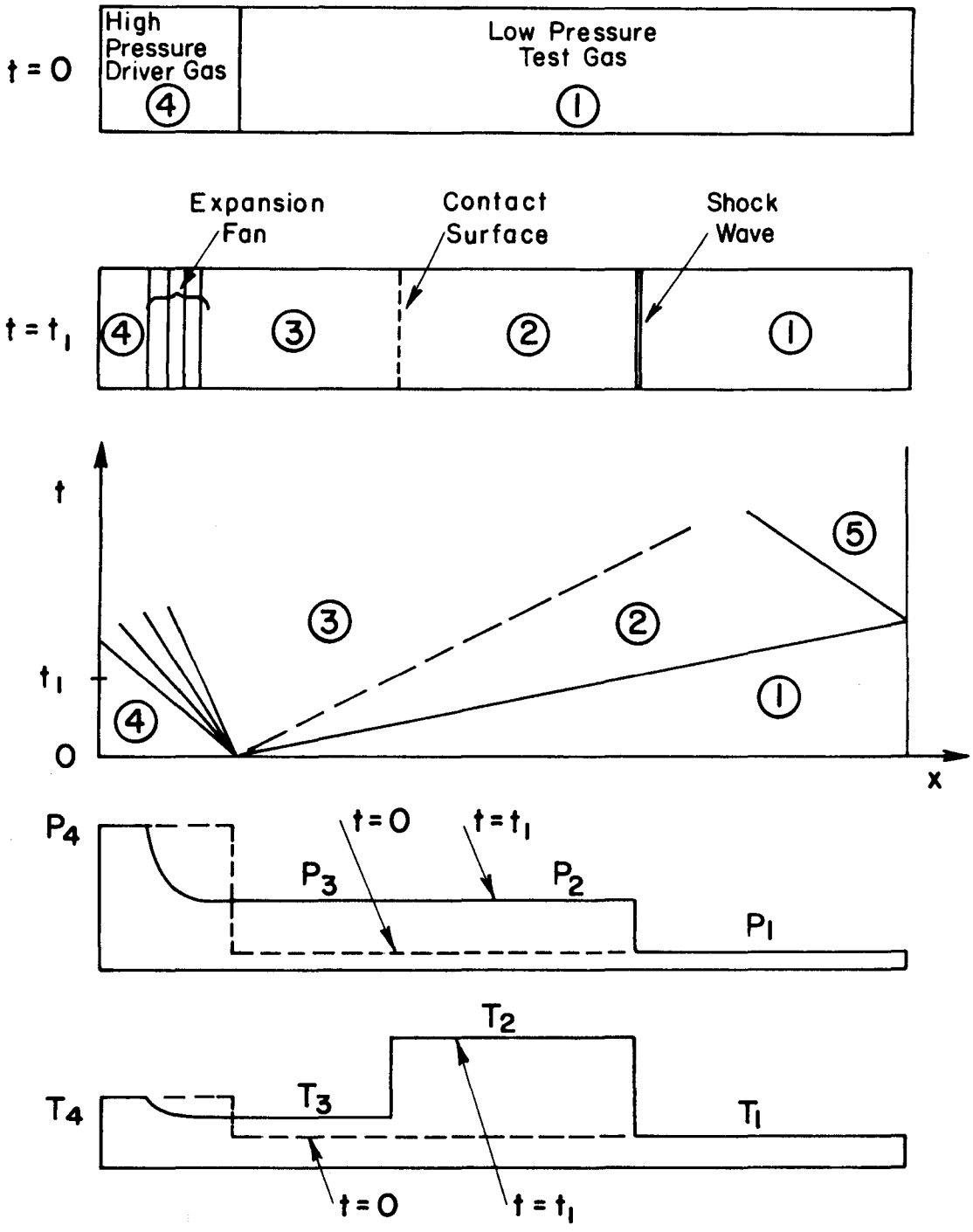

Figure 1. Ideal Shock Tube - Perfect Gas:

Notation and Concepts

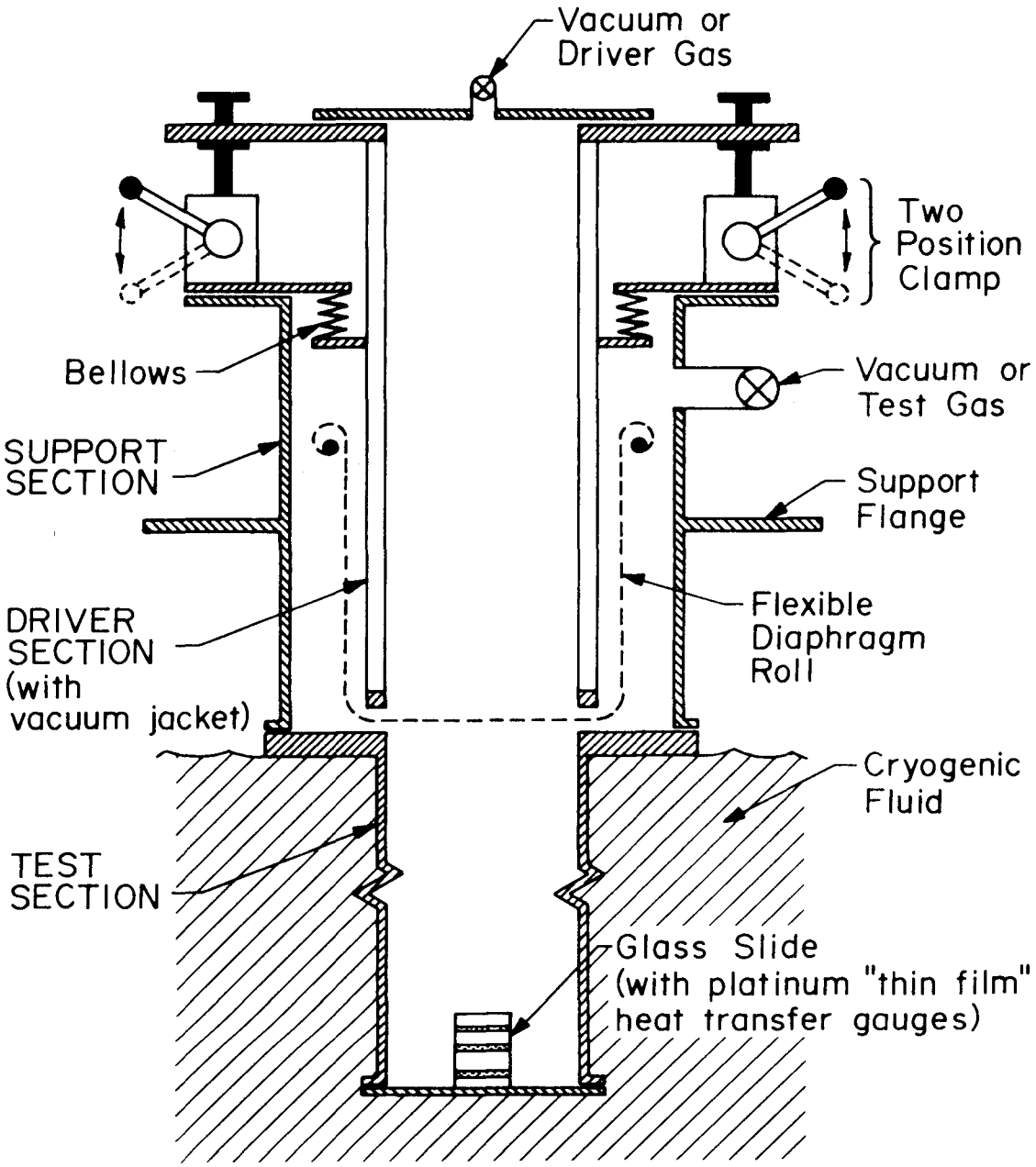

Figure 2. Schematic Drawing of the Cryogenic Shock Tube

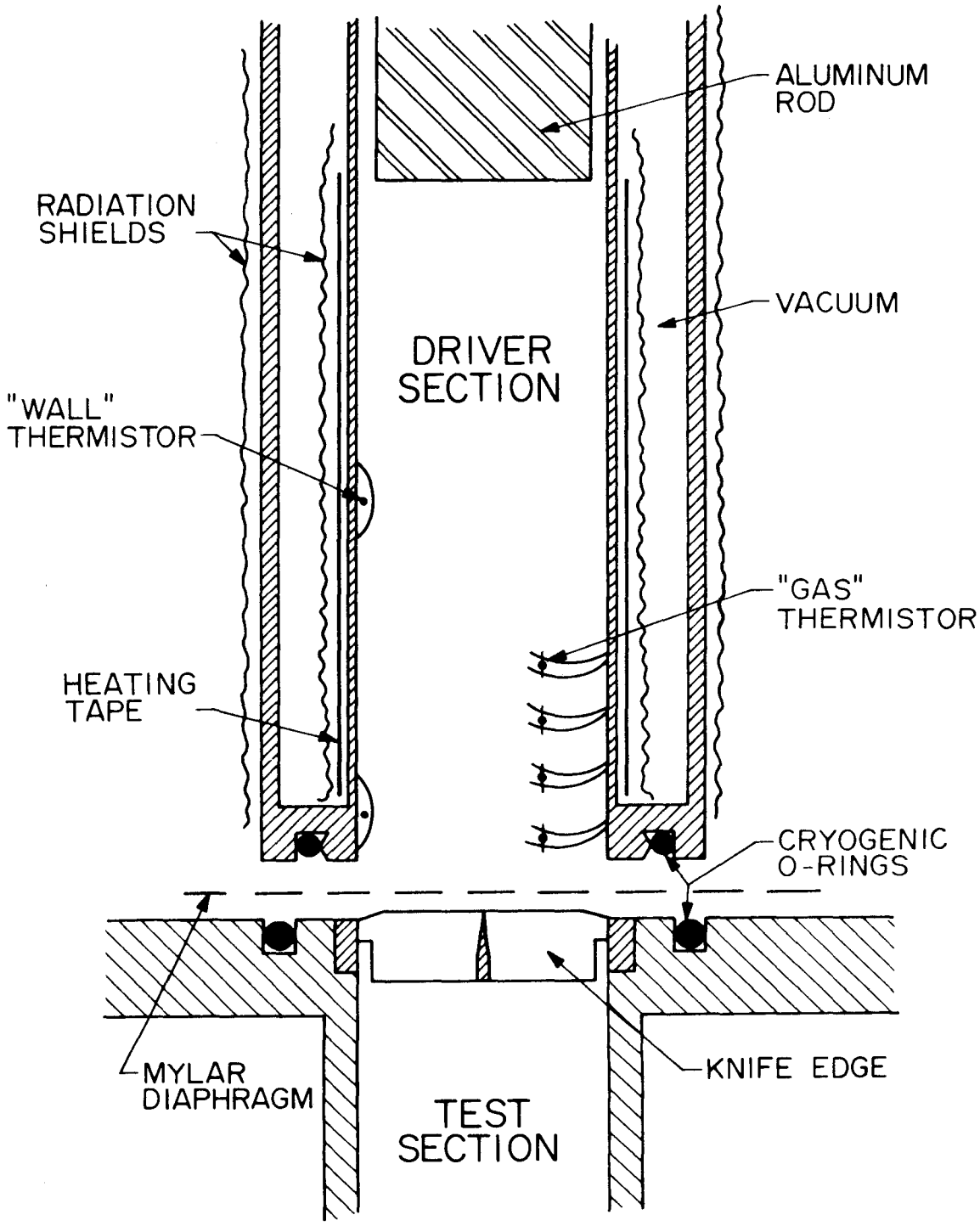

Figure 3. Detail of the Driver and Test Sections

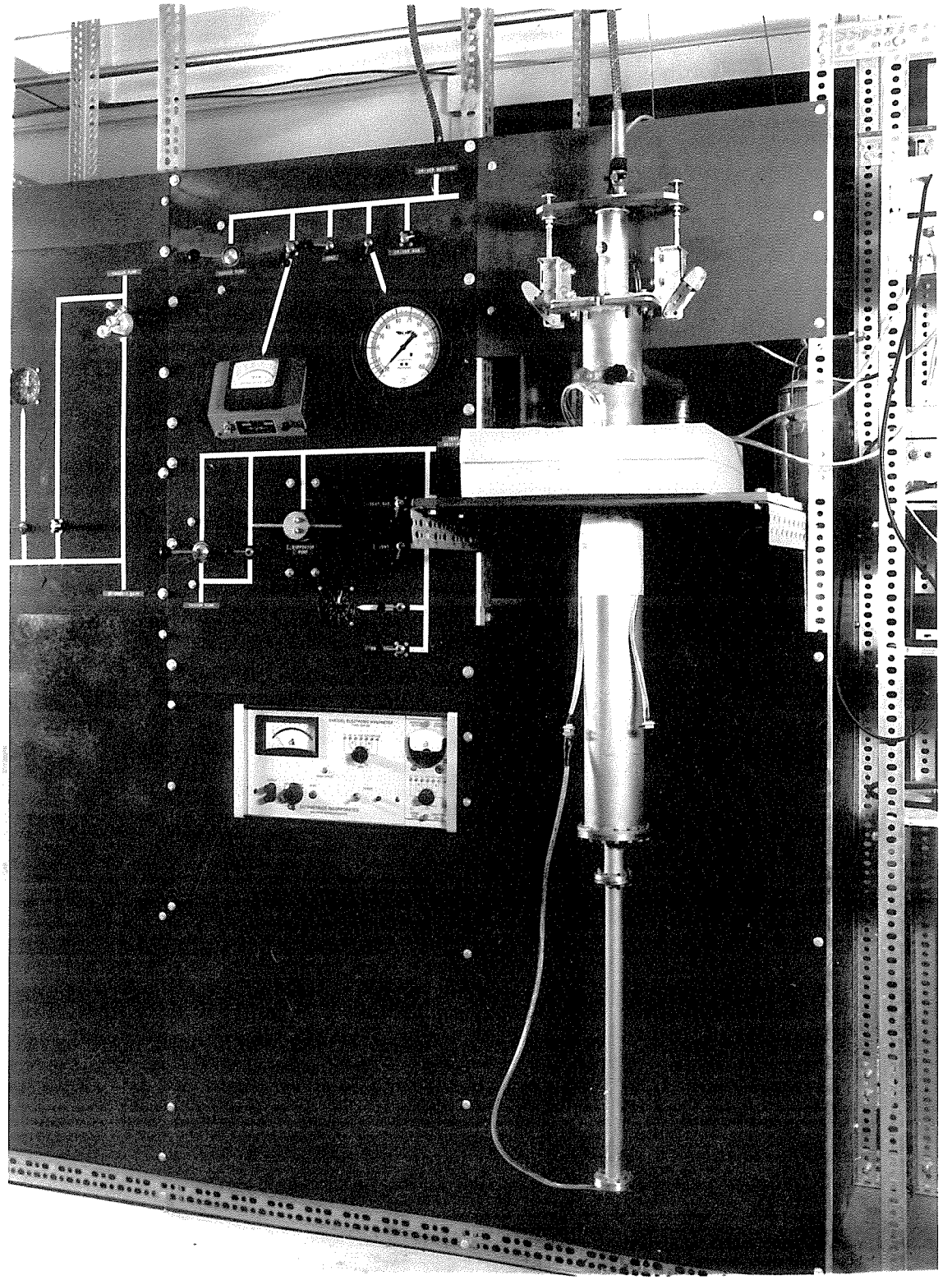

Figure 4. Cryogenic Shock Tube

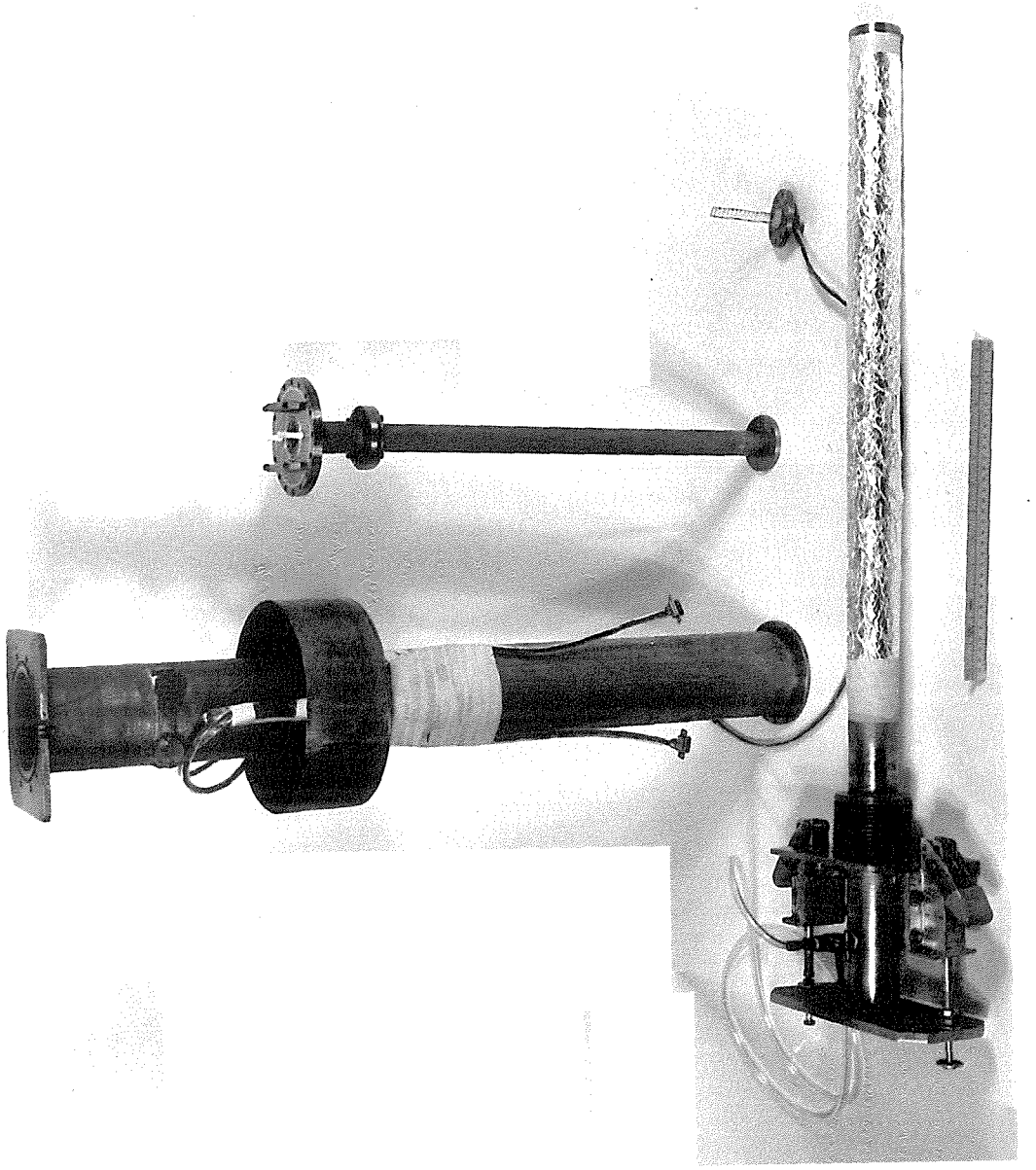

Figure 5. Disassembled Cryogenic Shock Tube

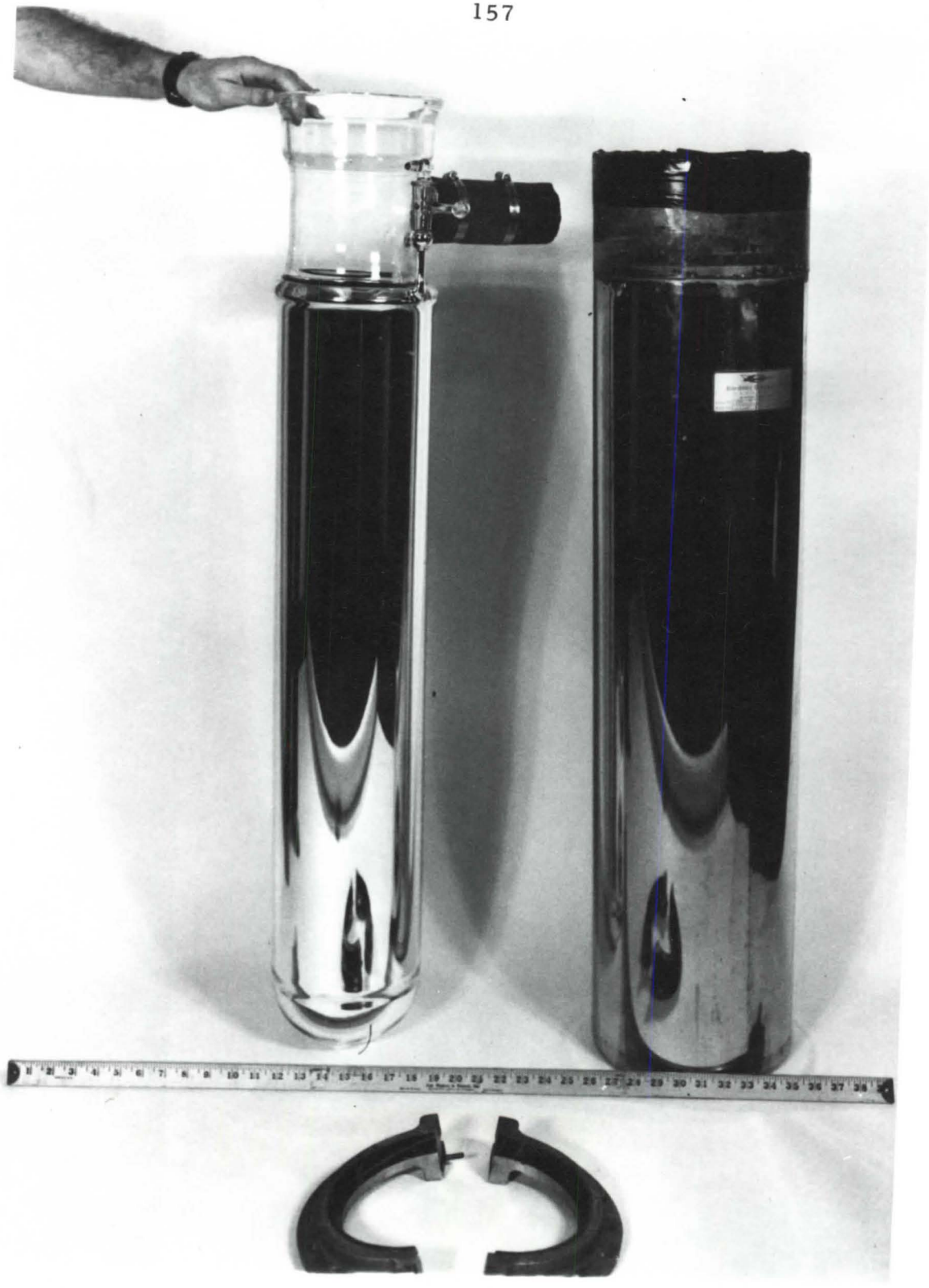

Figure 6. LHe Dewar, LN_2 Dewar, and Two-piece Collar

GLASS SLIDE WITH PLATINUM FILMS

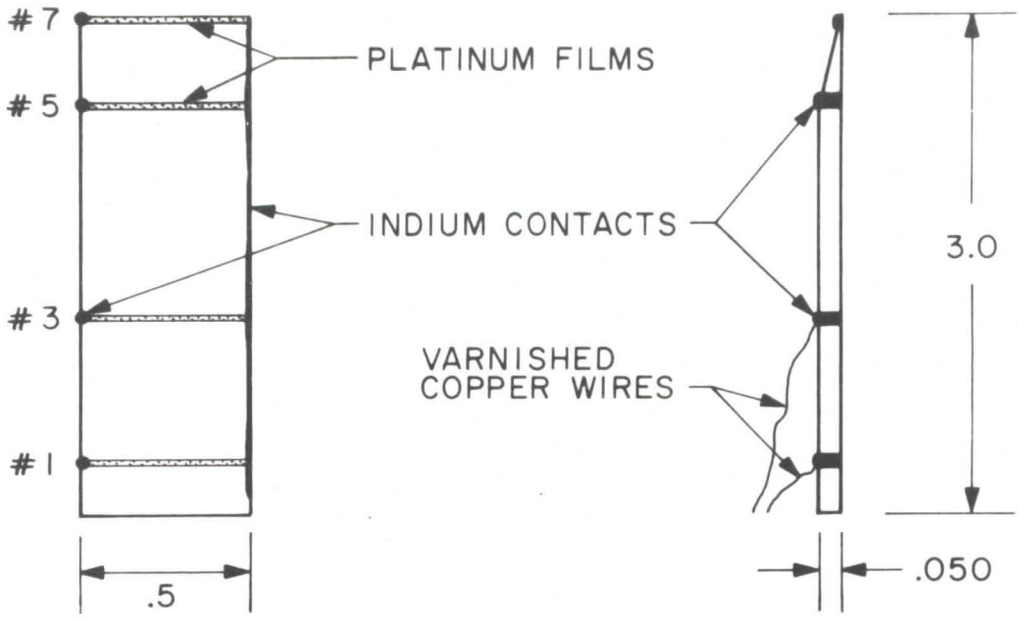

TYPICAL FILM RESPONSE

SWEEP TRIGGER: #7
UPPER BEAM: #5
LOWER BEAM: #1
0.5 volt/cm
5 μsec/cm

TEST GAS: He
T_1 = 4.2 °K
P_1 = 1.0 torr

DRIVER GAS: He
T_4 = 300 °K
P_4 = 25 psia

M_s = 12

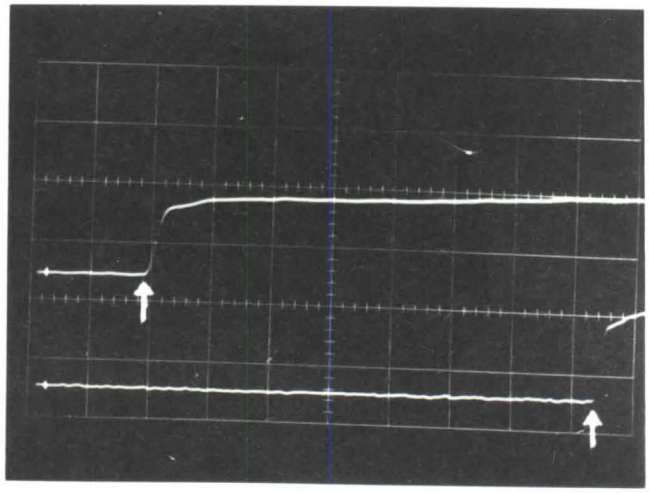

Figure 7. Glass Slide with Film Gauges; Typical Film Response

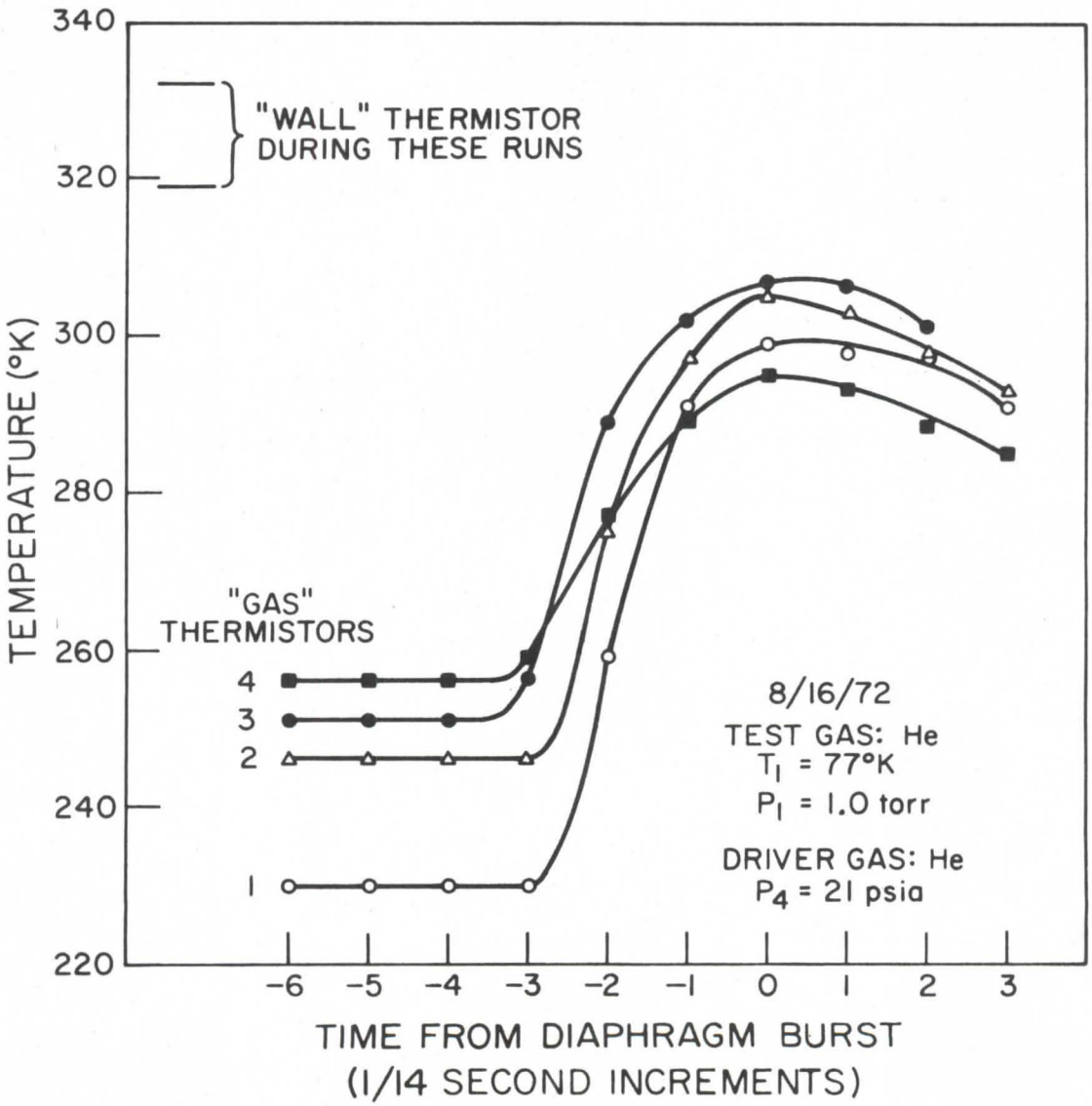

Figure 8. Driver Gas Temperature for $T_1 = 77^{\circ}K$

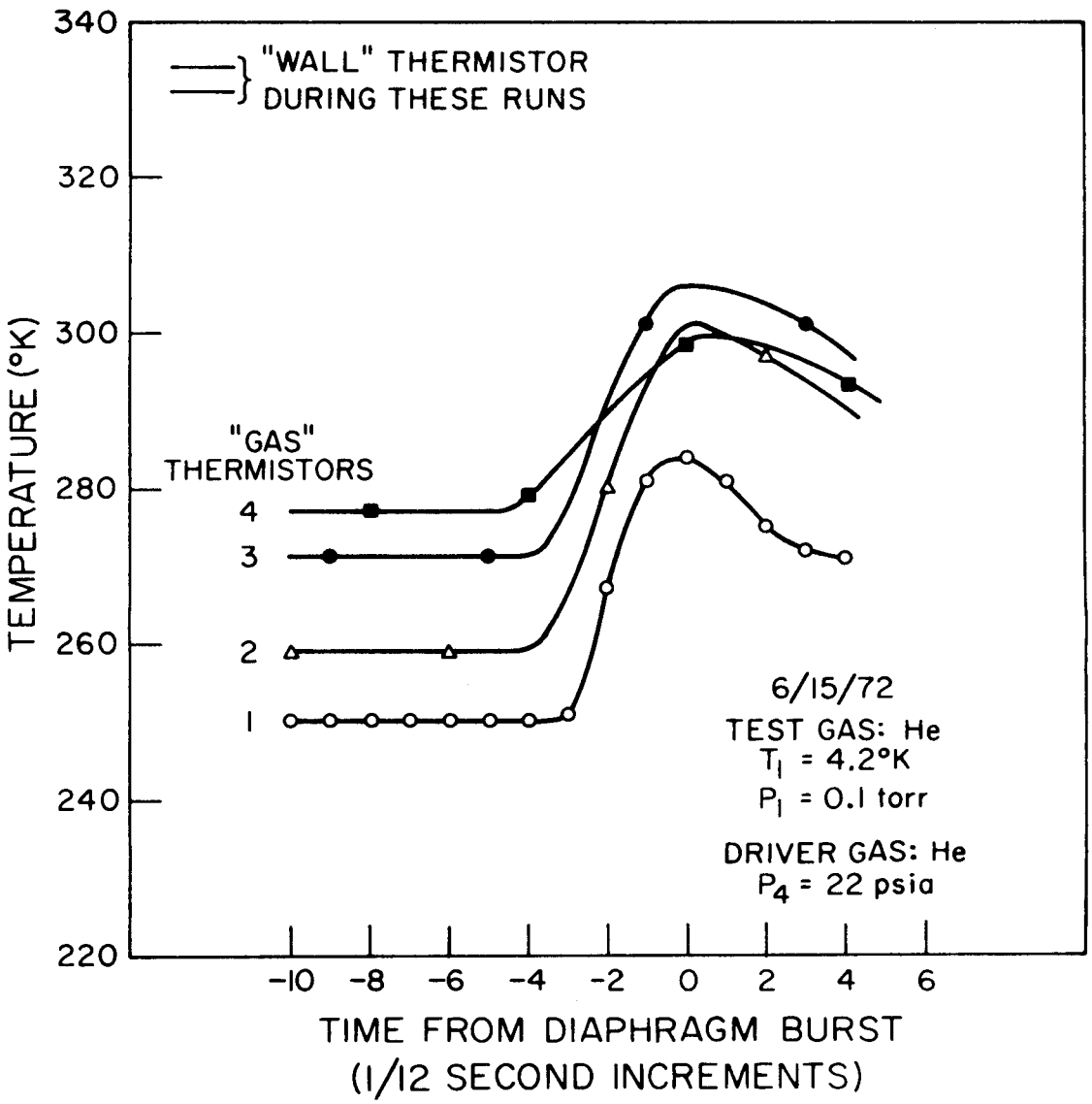

Figure 9. Driver Gas Temperature for $T_1 = 4.2^{\circ}K$

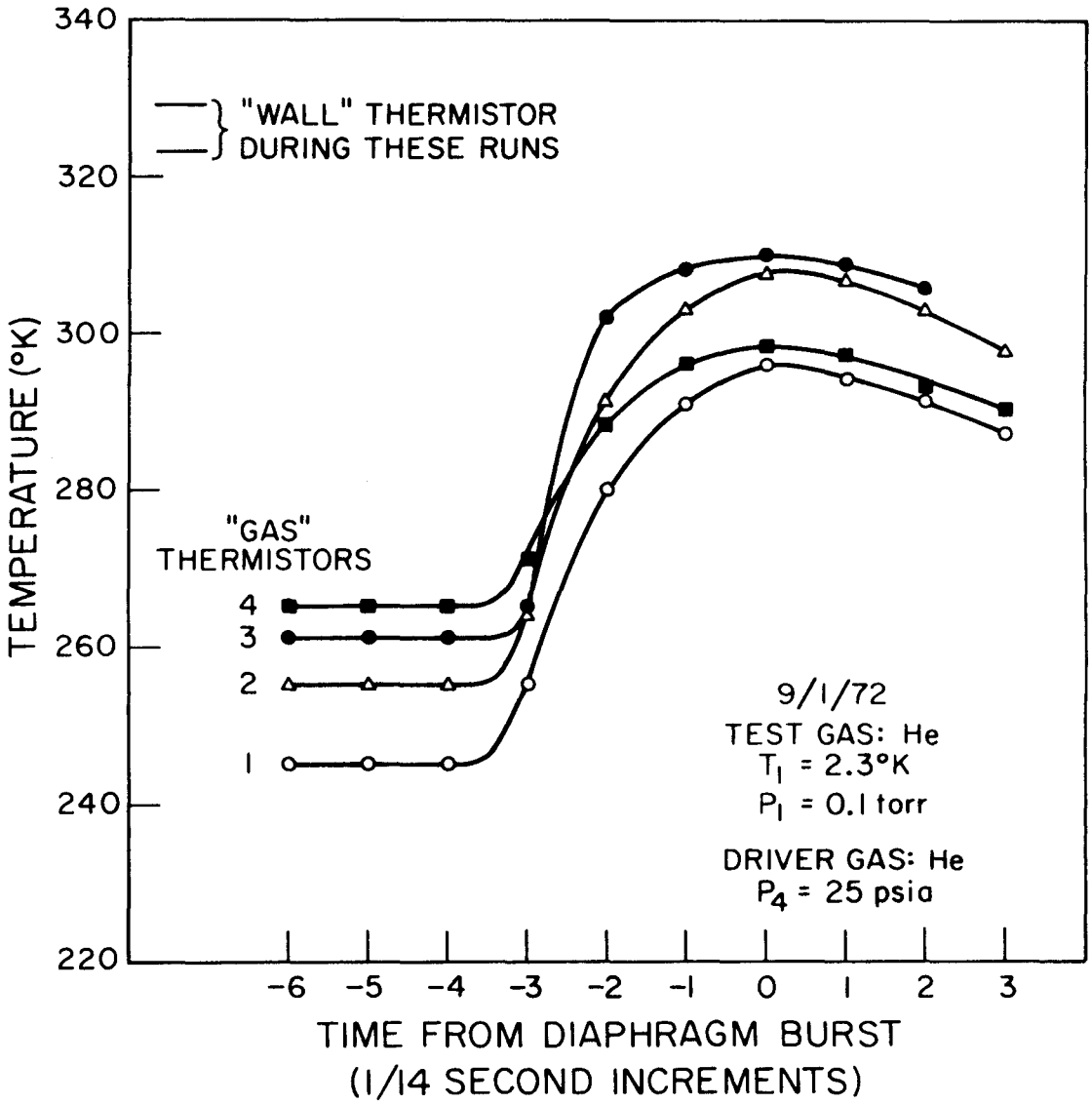

Figure 10. Driver Gas Temperature for $T_1 = 2.3^{\circ}K$

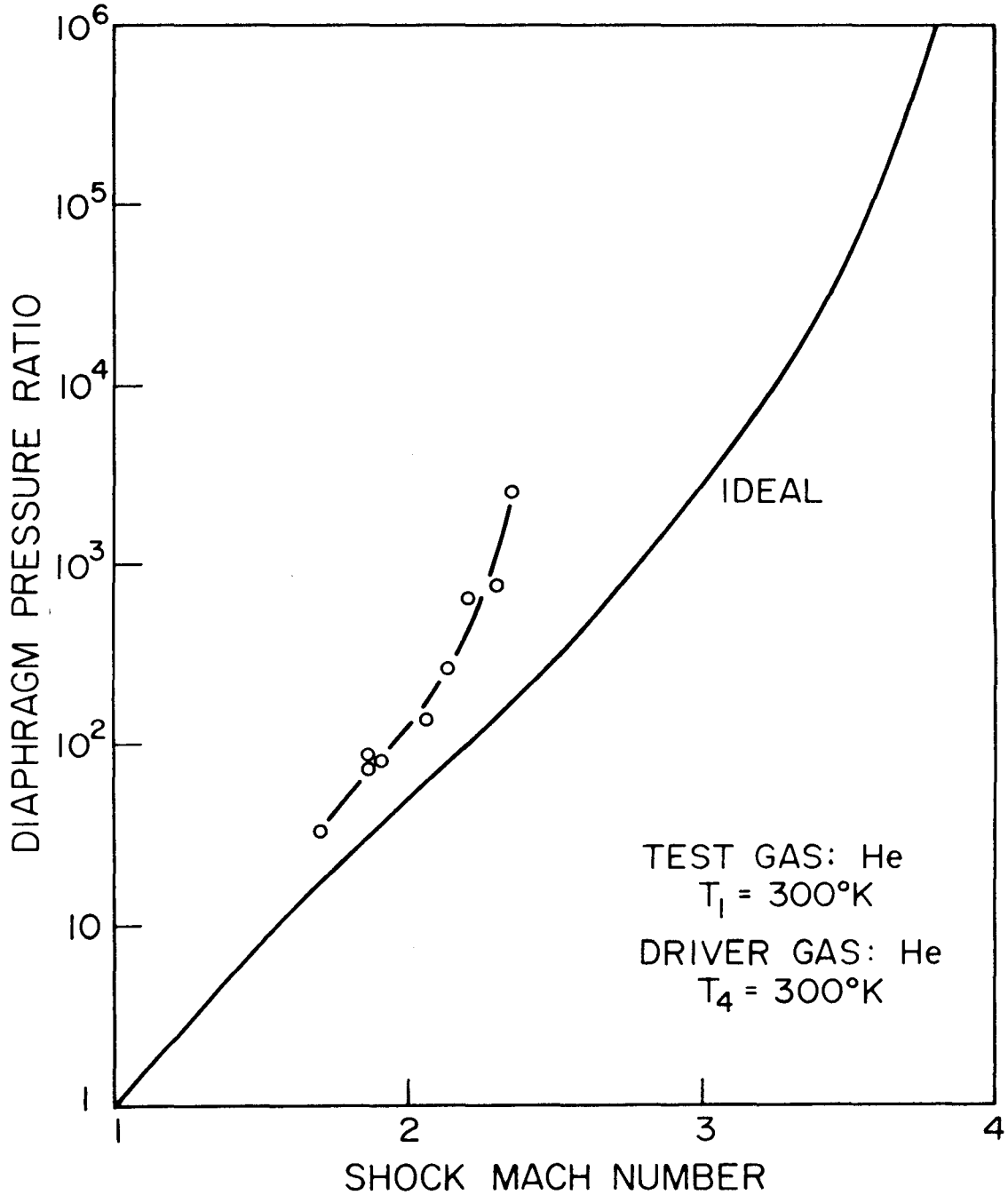

Figure 11. Shock Mach Numbers for $T_1 = 300^{\circ}K$

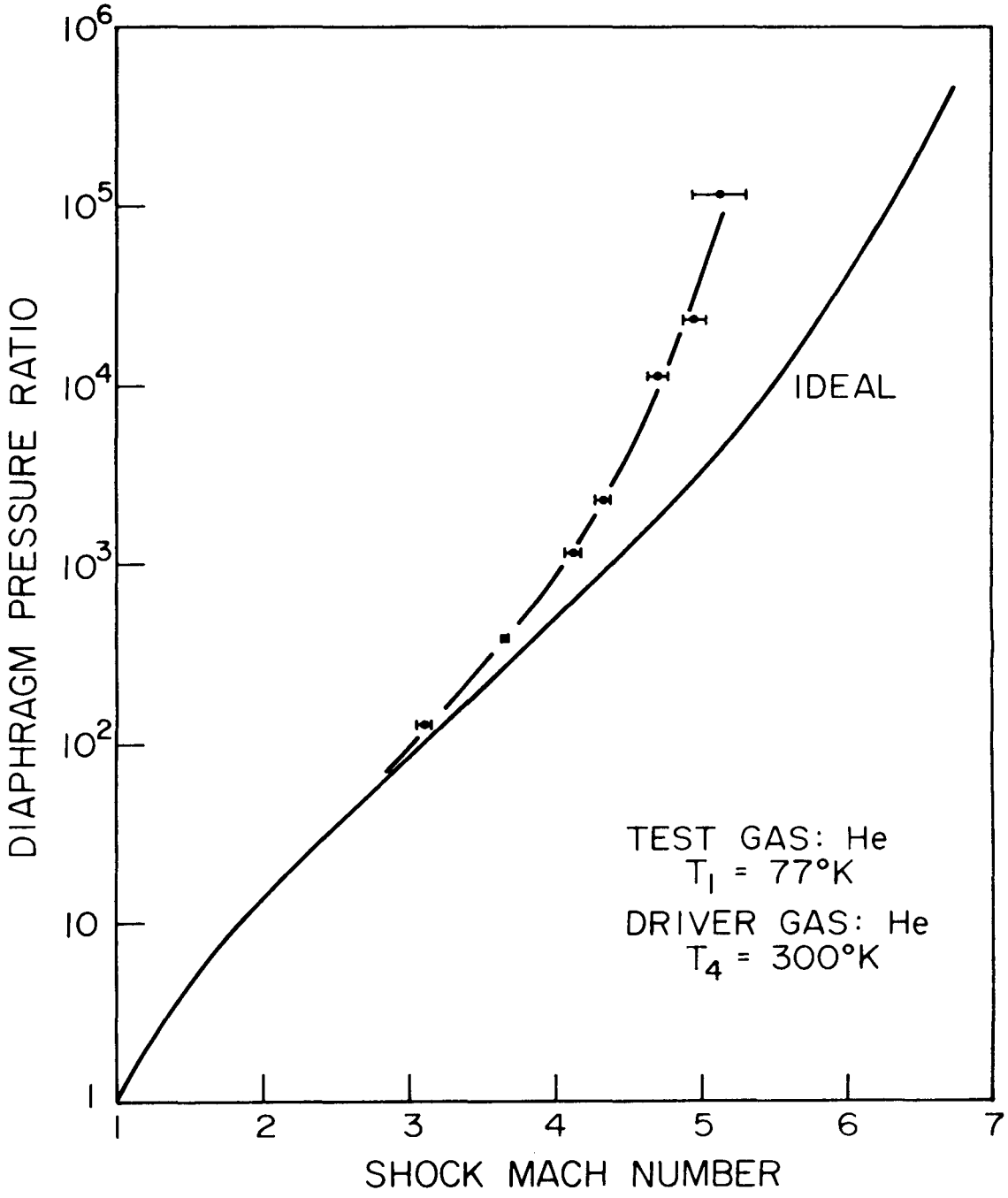

Figure 12. Shock Mach Numbers for $T_1 = 77^{O}K$

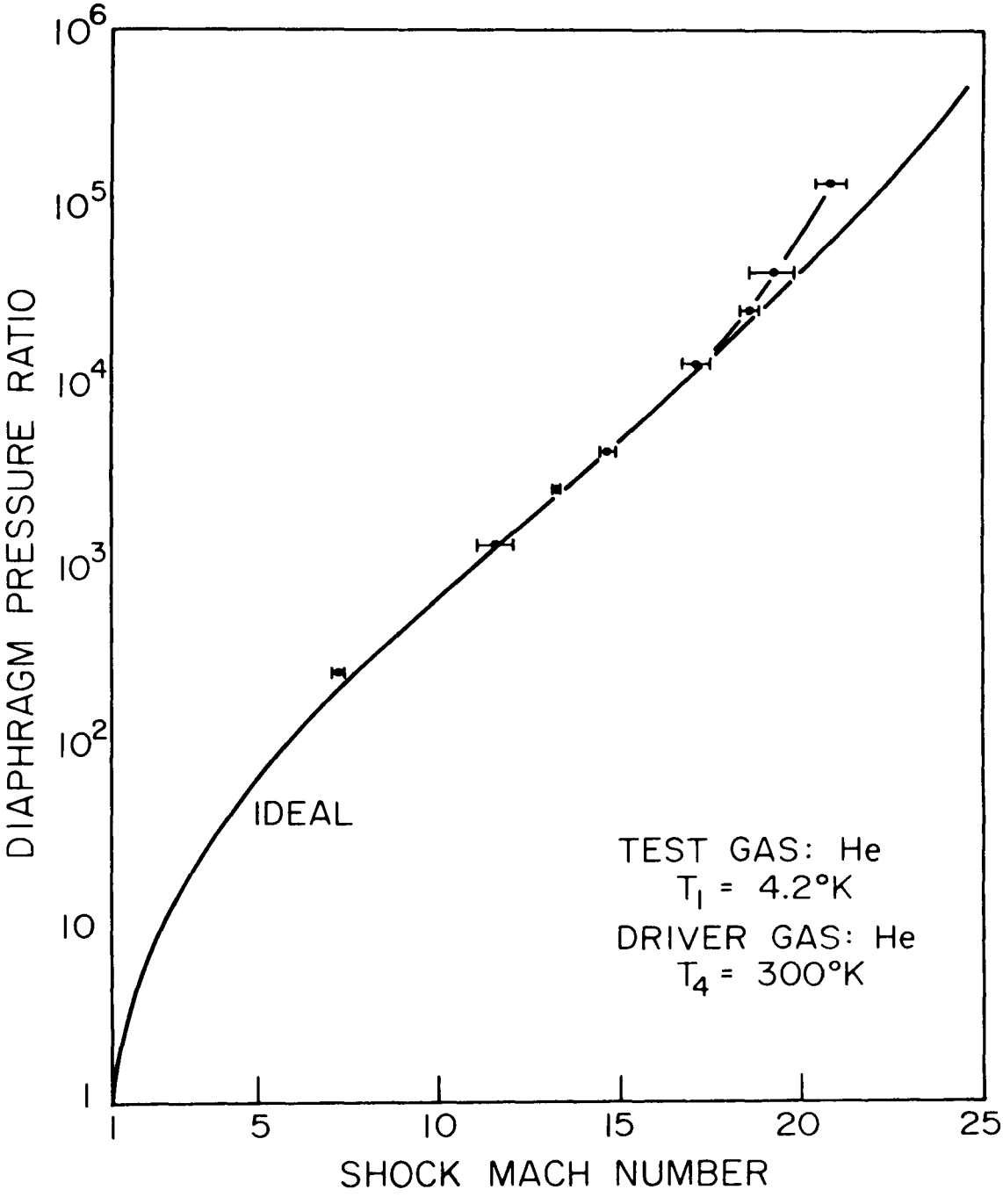

Figure 13. Shock Mach Numbers for $T_1 = 4.2^{\circ}K$

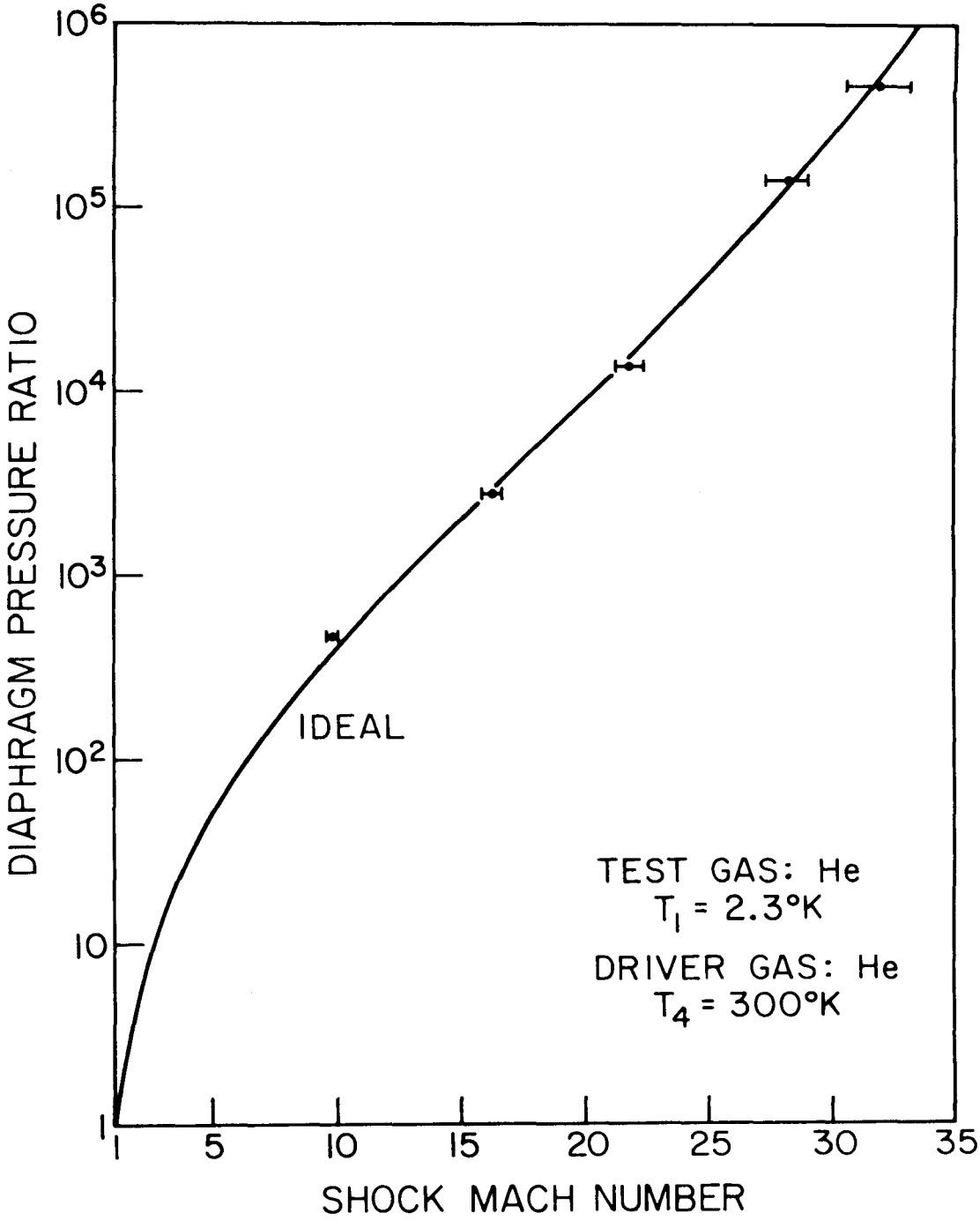

Figure 14. Shock Mach Numbers for $T_1 = 2.3^{\circ}K$

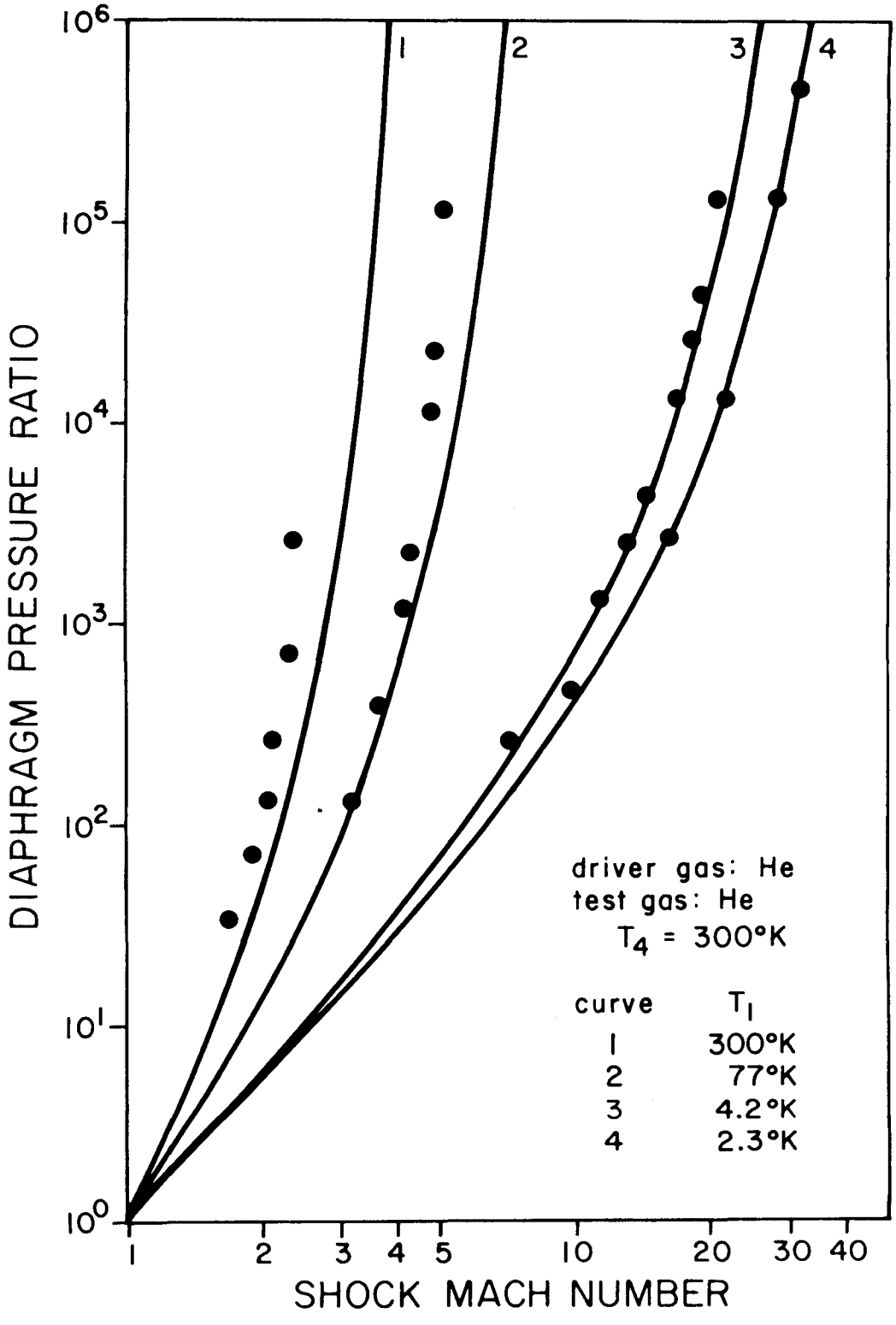

Figure 15. Comparison of Shock Mach Numbers with Theoretical Predictions for All T_1 Cases

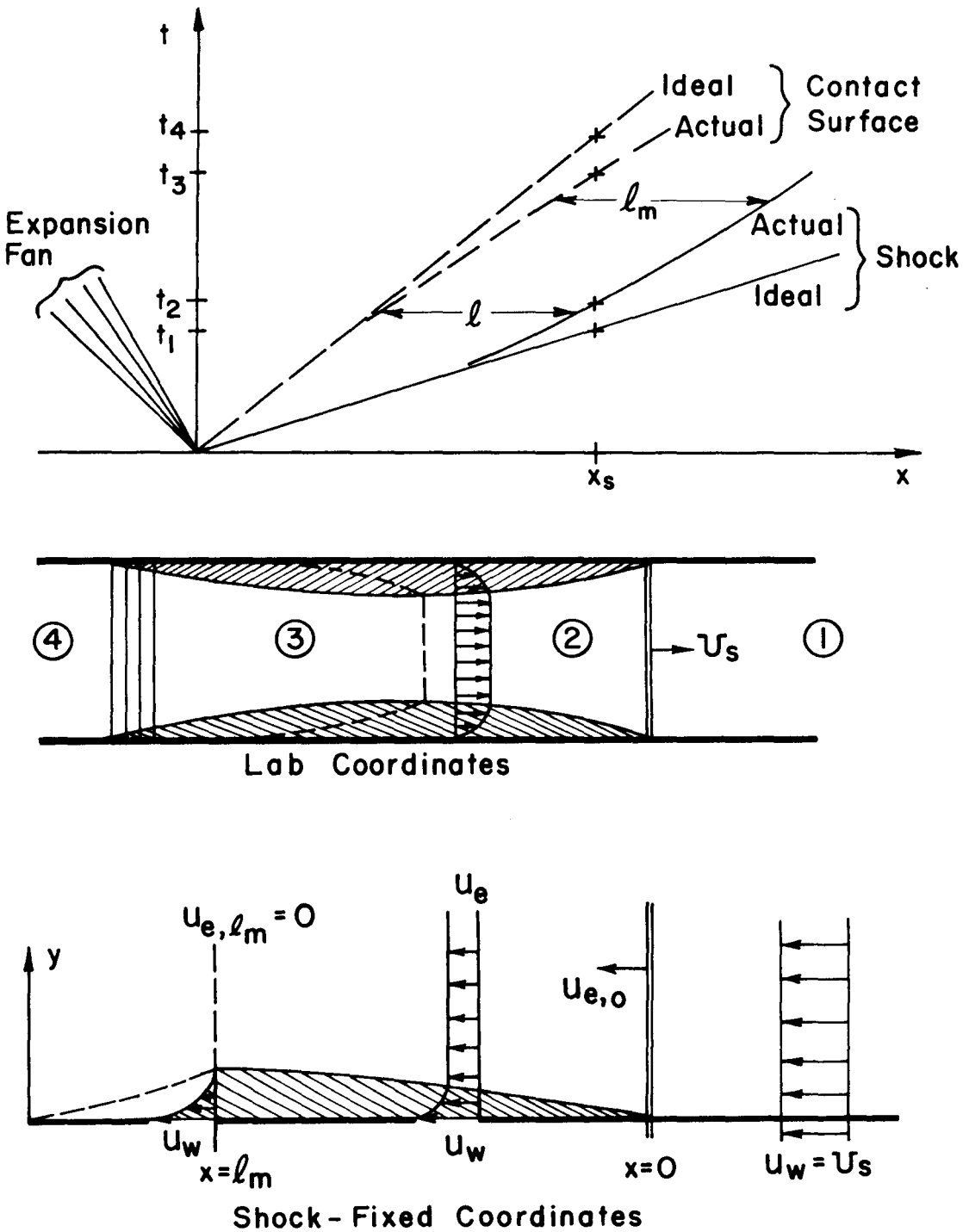

Figure 16. Shock Tube Boundary Layer: Notation and Concepts

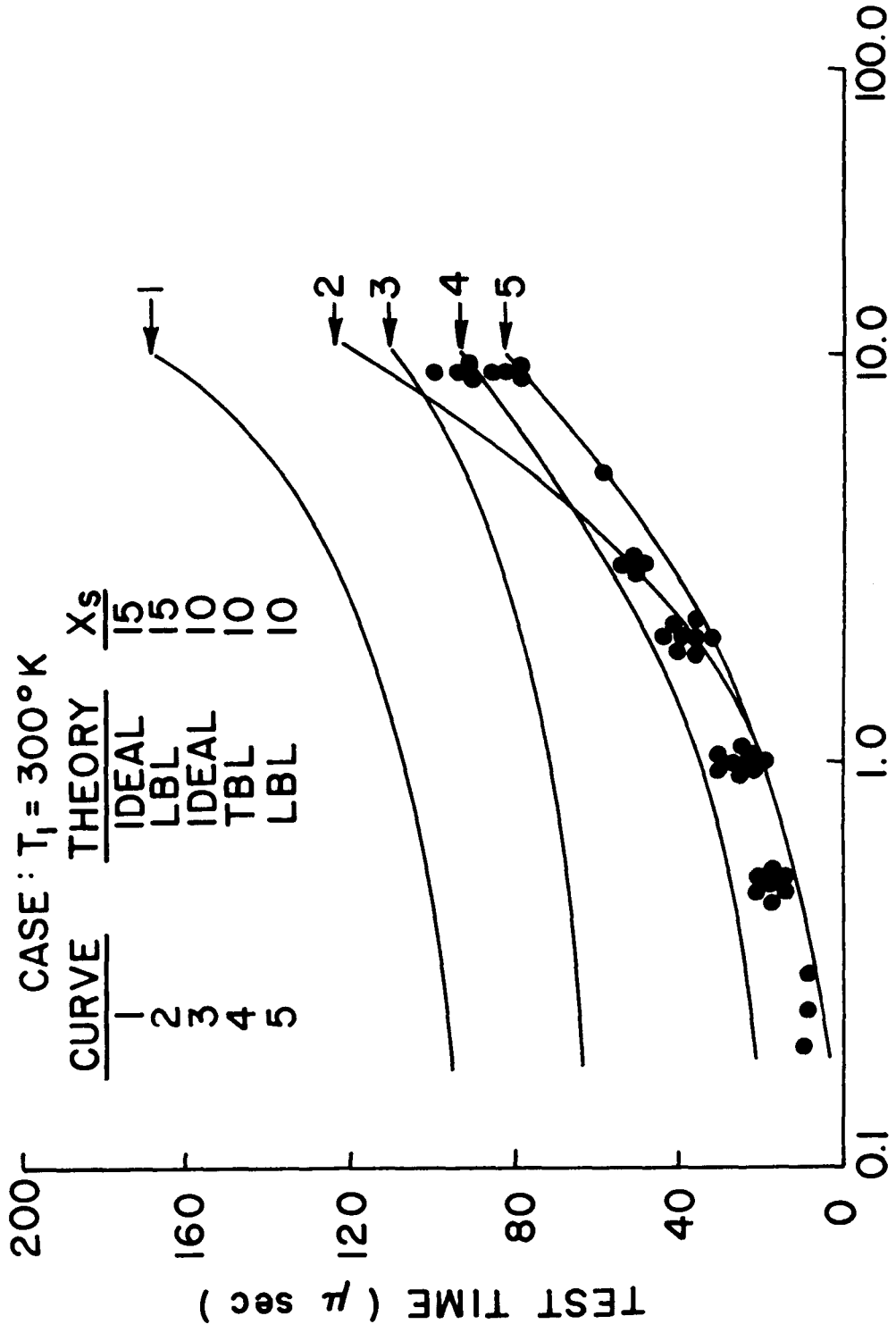

Figure 17. Test Times for $T_1 = 300^{\circ}K$

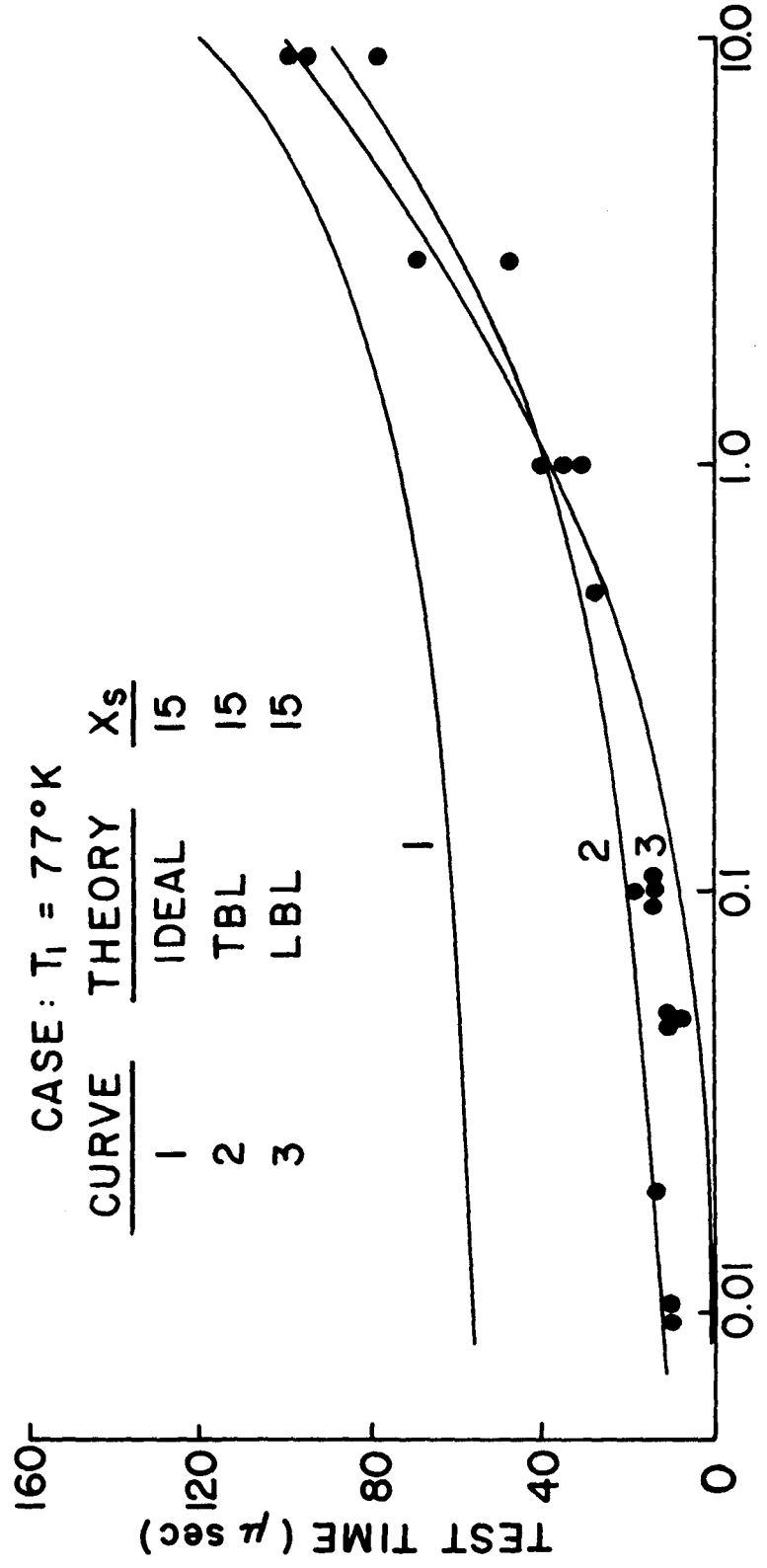

Figure 18. Test Times for T_1 = 77°K

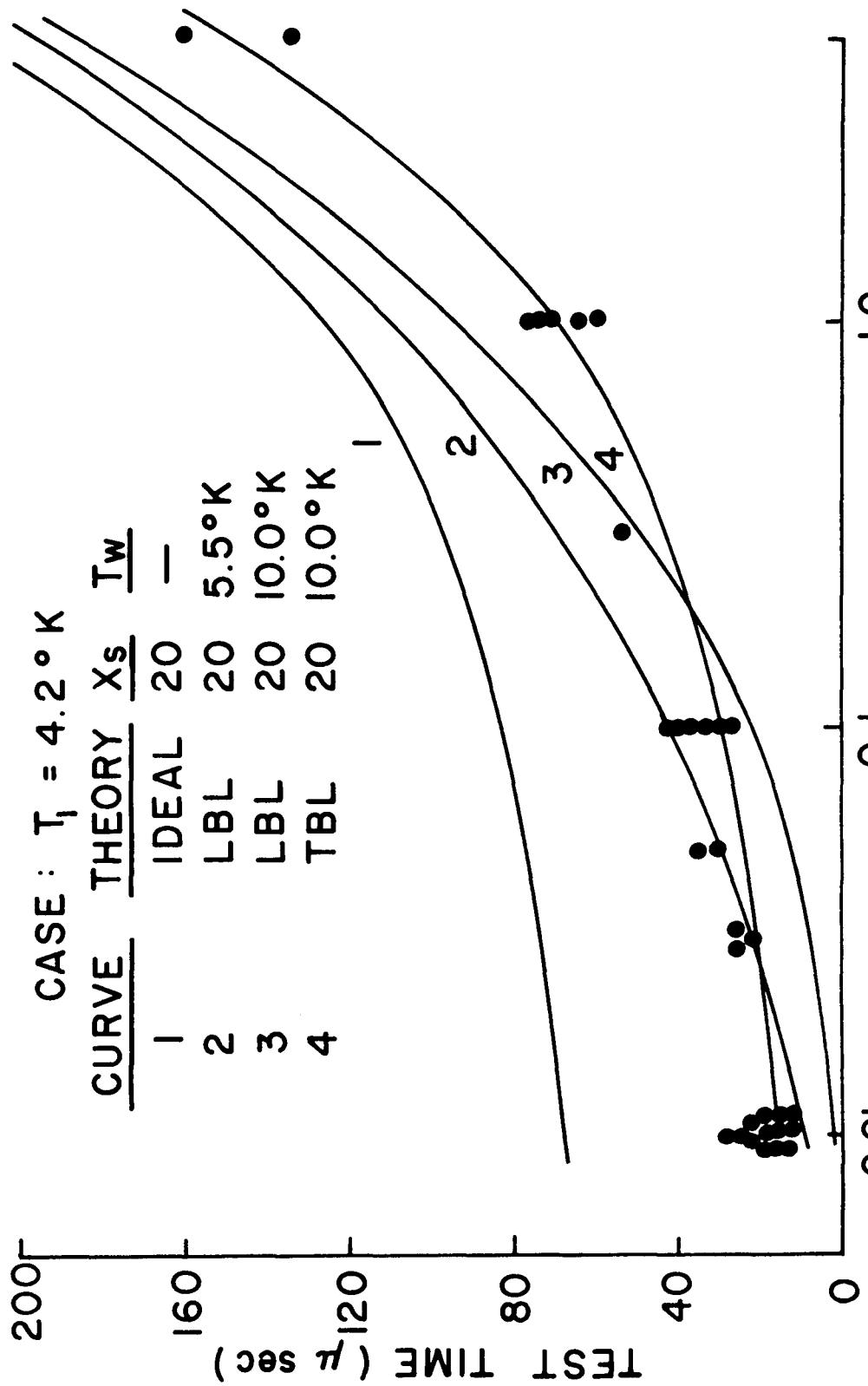

Figure 19. Test Times for $T_1 = 4.2^{\circ}K$

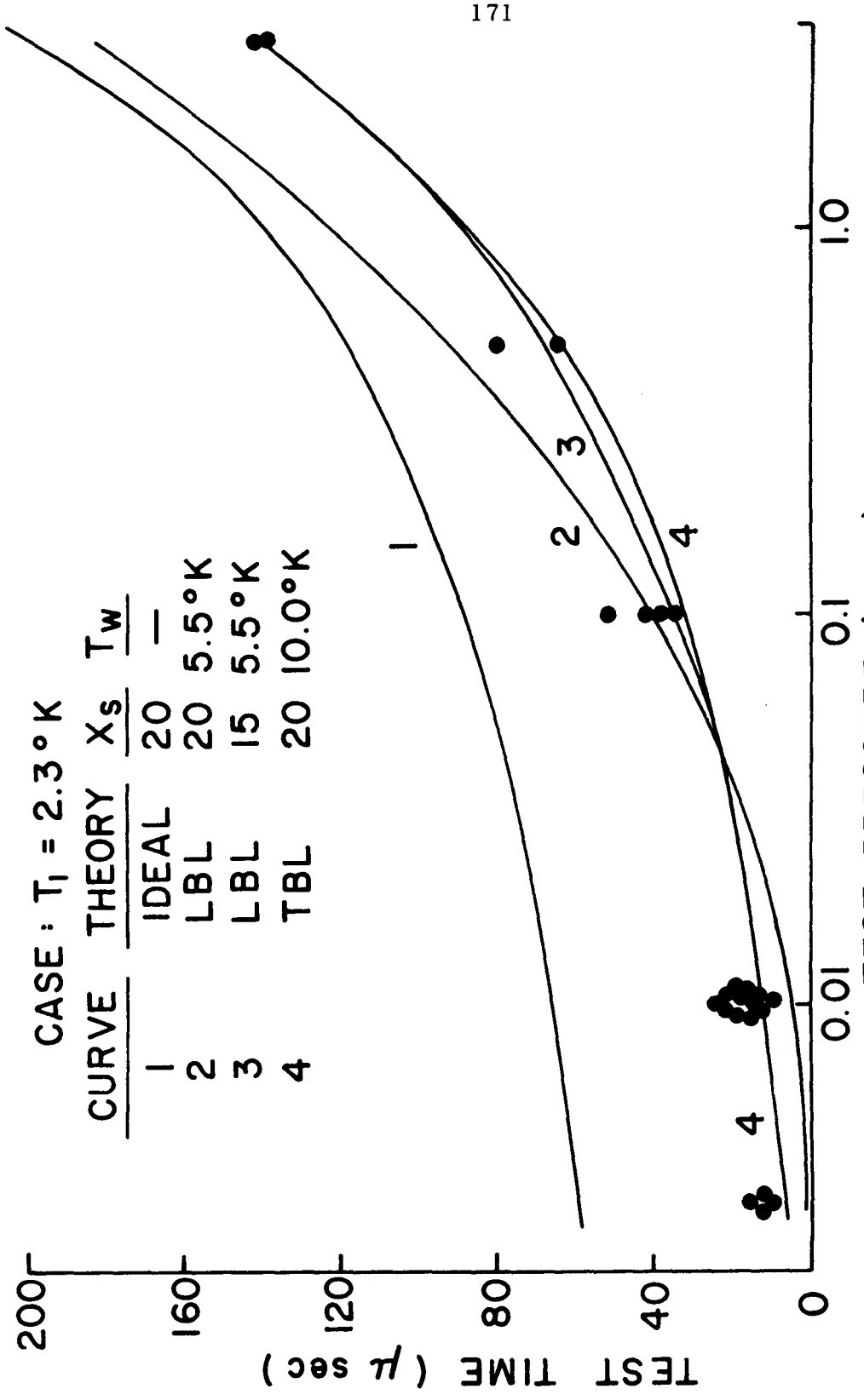

Figure 20. Test Times for T_1 = 2.3°K

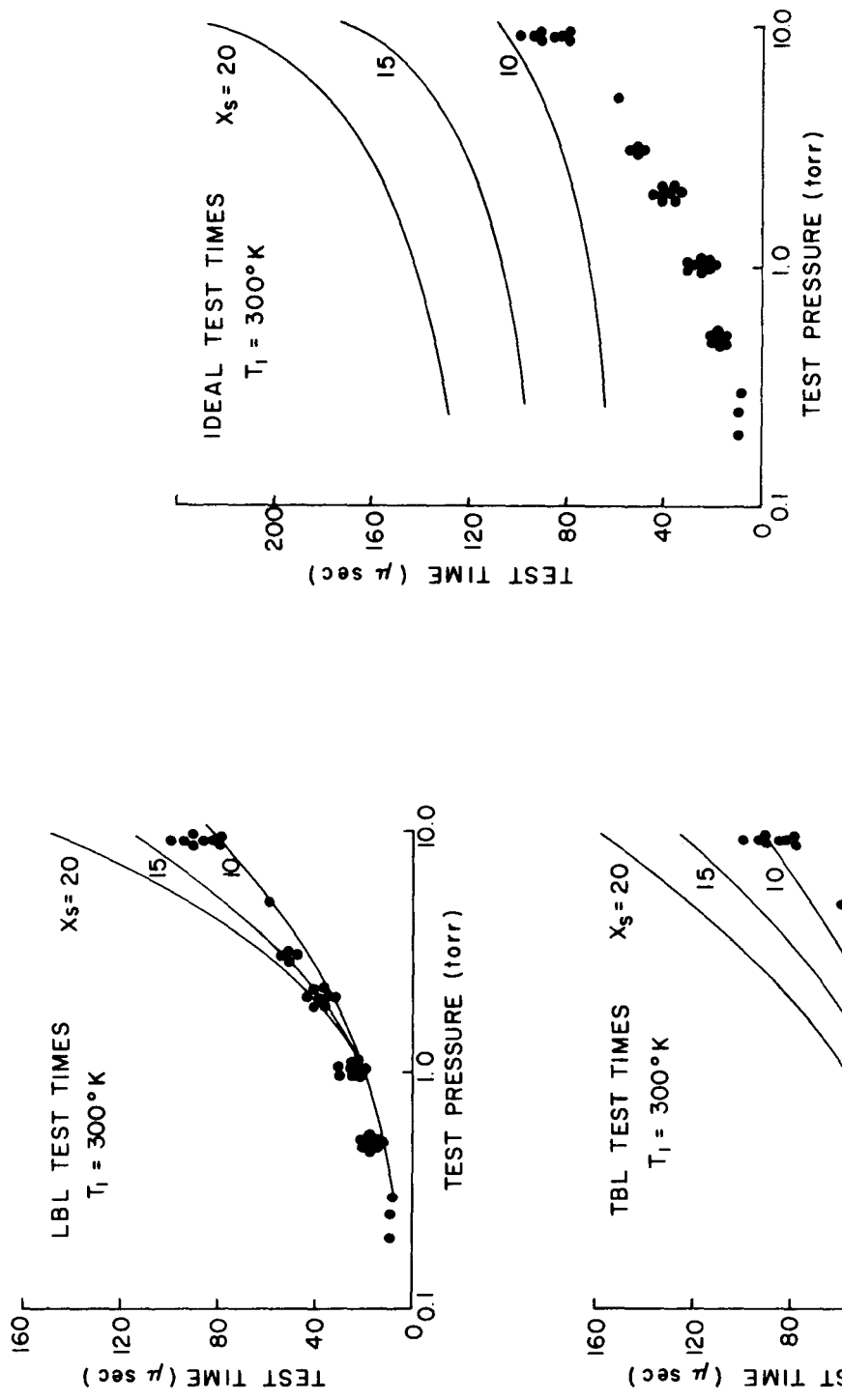

Figure 21. Comparison of Test Time Data with Theoretical Predictions for $T_1 = 300^0K$

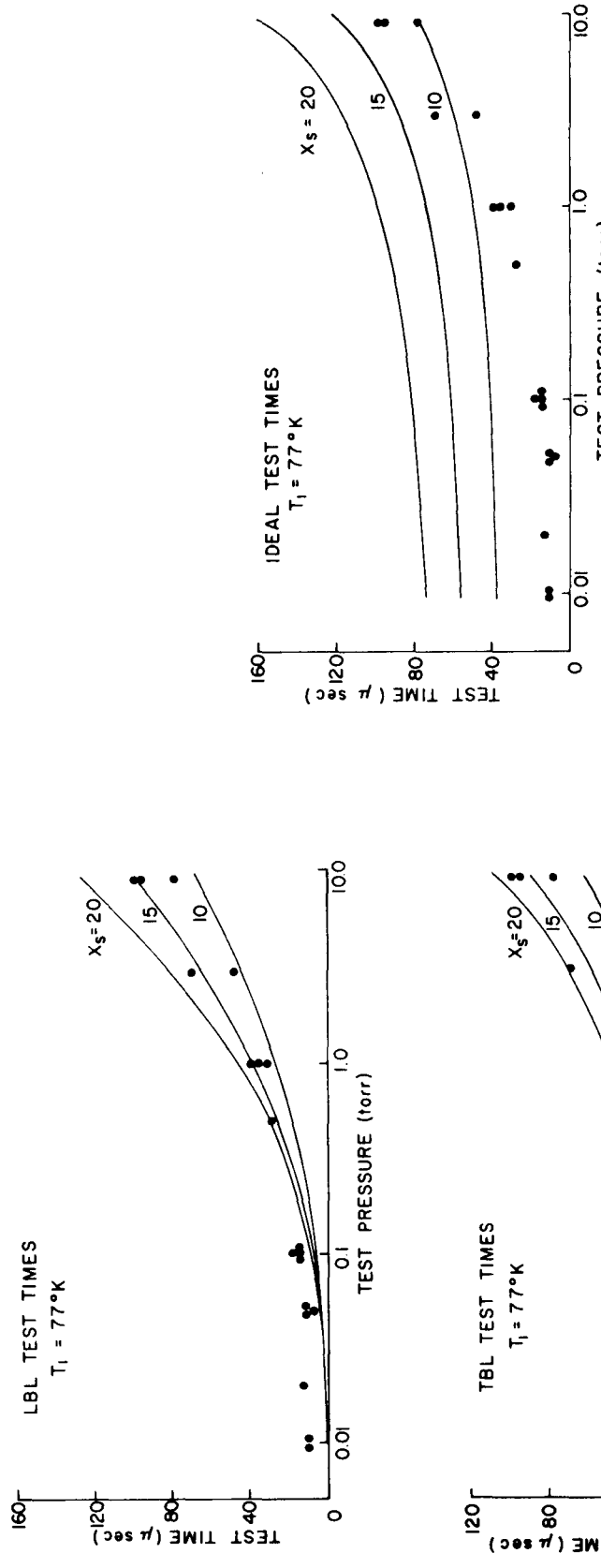

Figure 22. Comparison of Test Time Data with Theoretical Predictions for $T_1 = 77^{\circ}K$

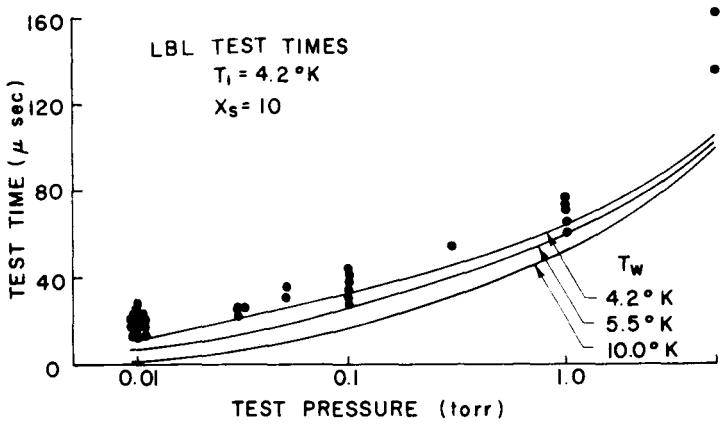

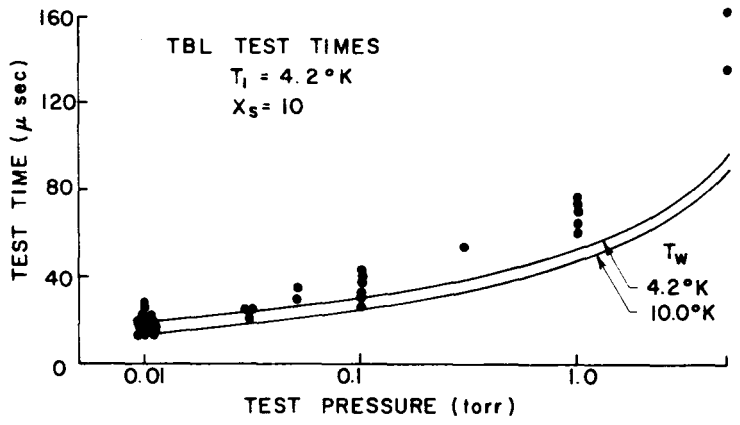

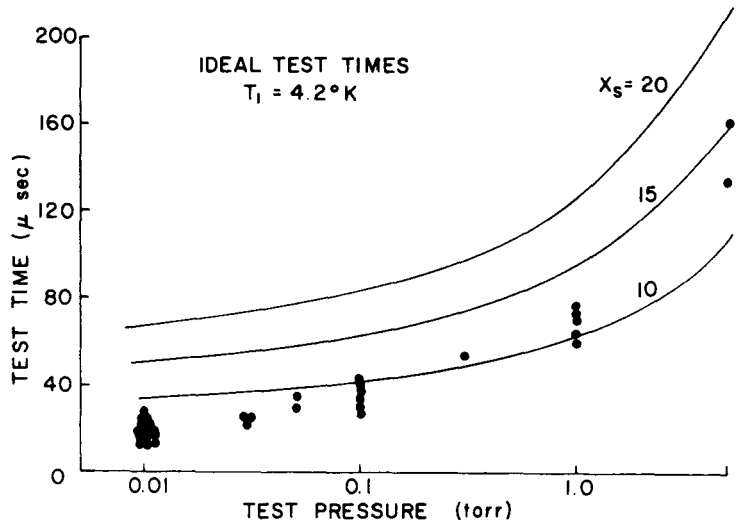

Figure 23. Comparison of Test Time Data with Theoretical Predictions for $T_1 = 4.2^{\circ}K$ ($x_s = 10$)

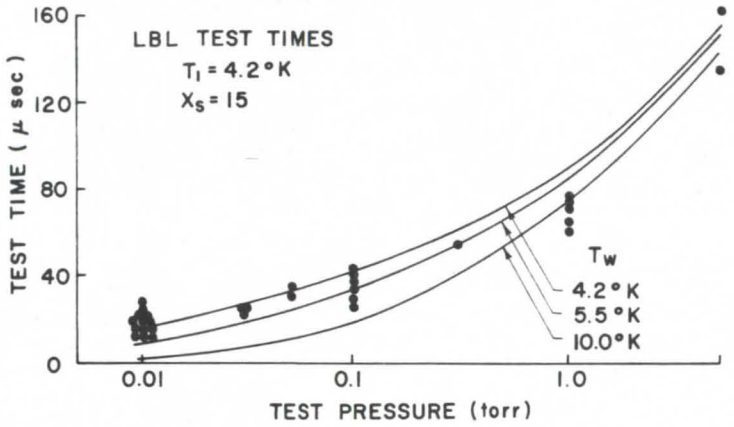

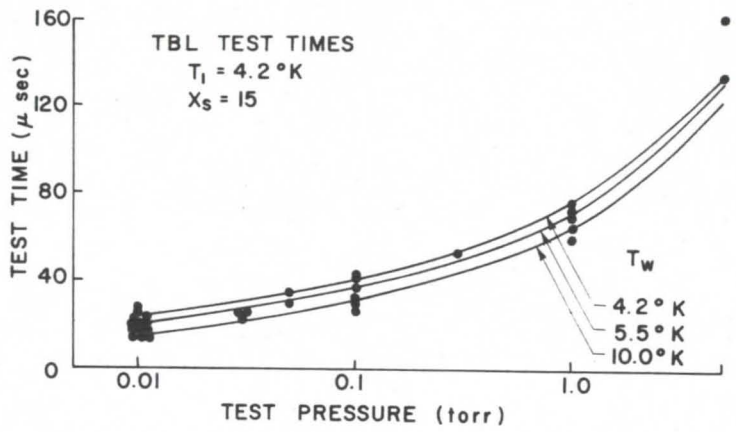

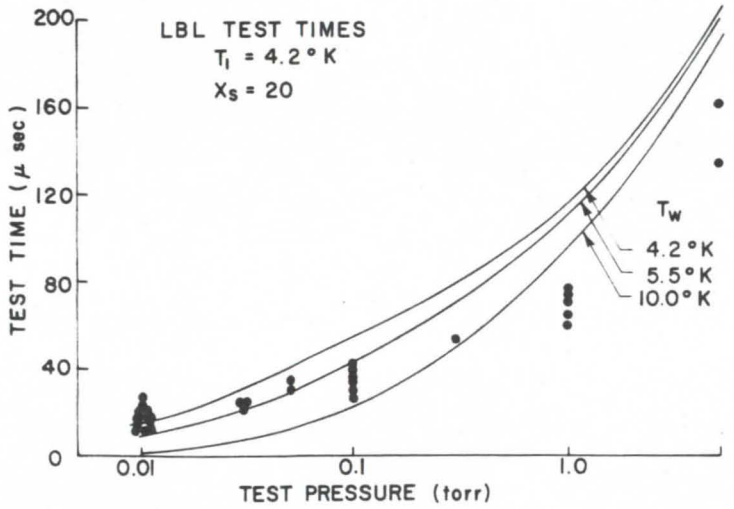

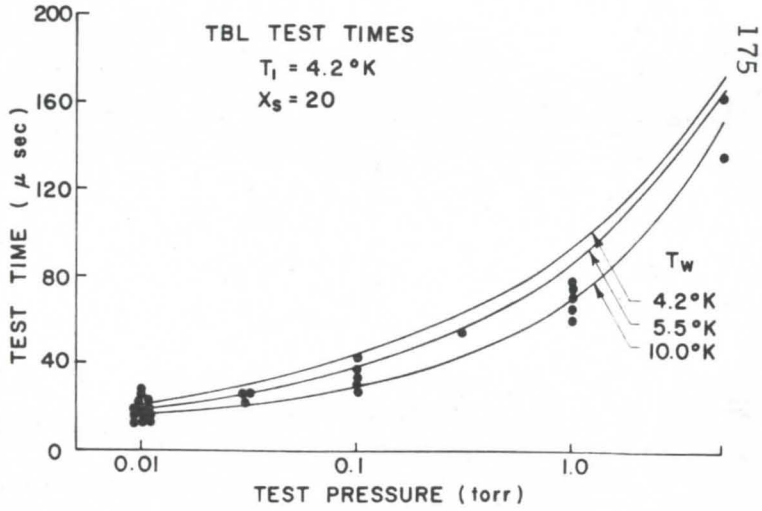

Figure 24. Comparison of Test Time Data with Theoretical Predictions for $T_1 = 4.2^{\circ}K$ (x_s = 15, 20)

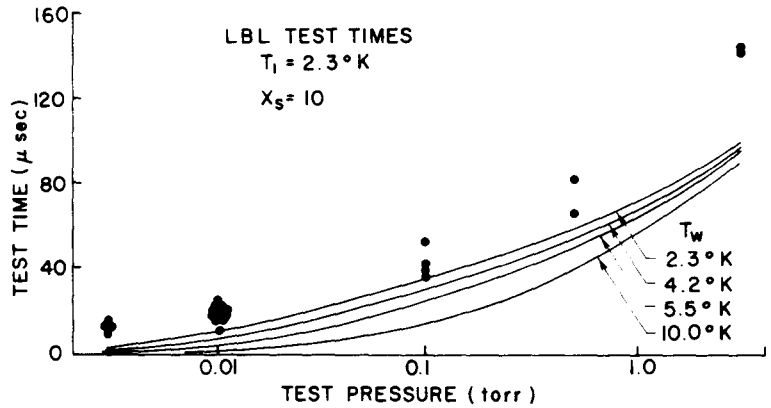

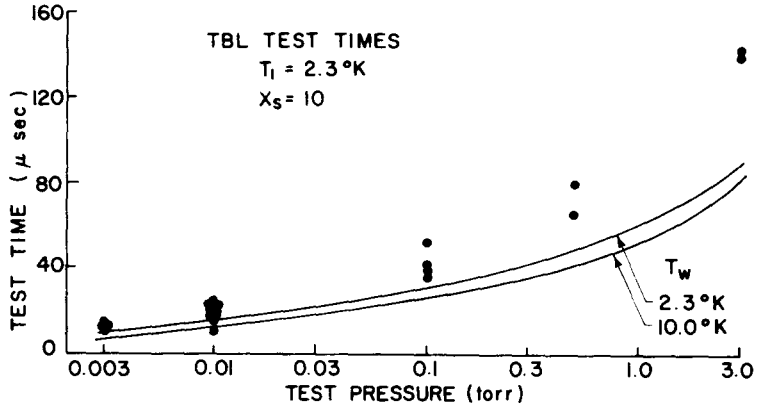

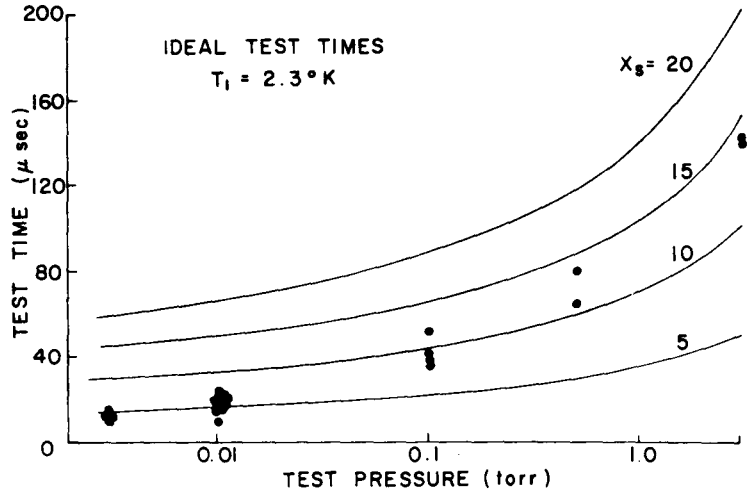

Figure 25. Comparison of Test Time Data with Theoretical Predictions for $T_1 = 2.3^{\circ}K$ ($x_s = 10$)

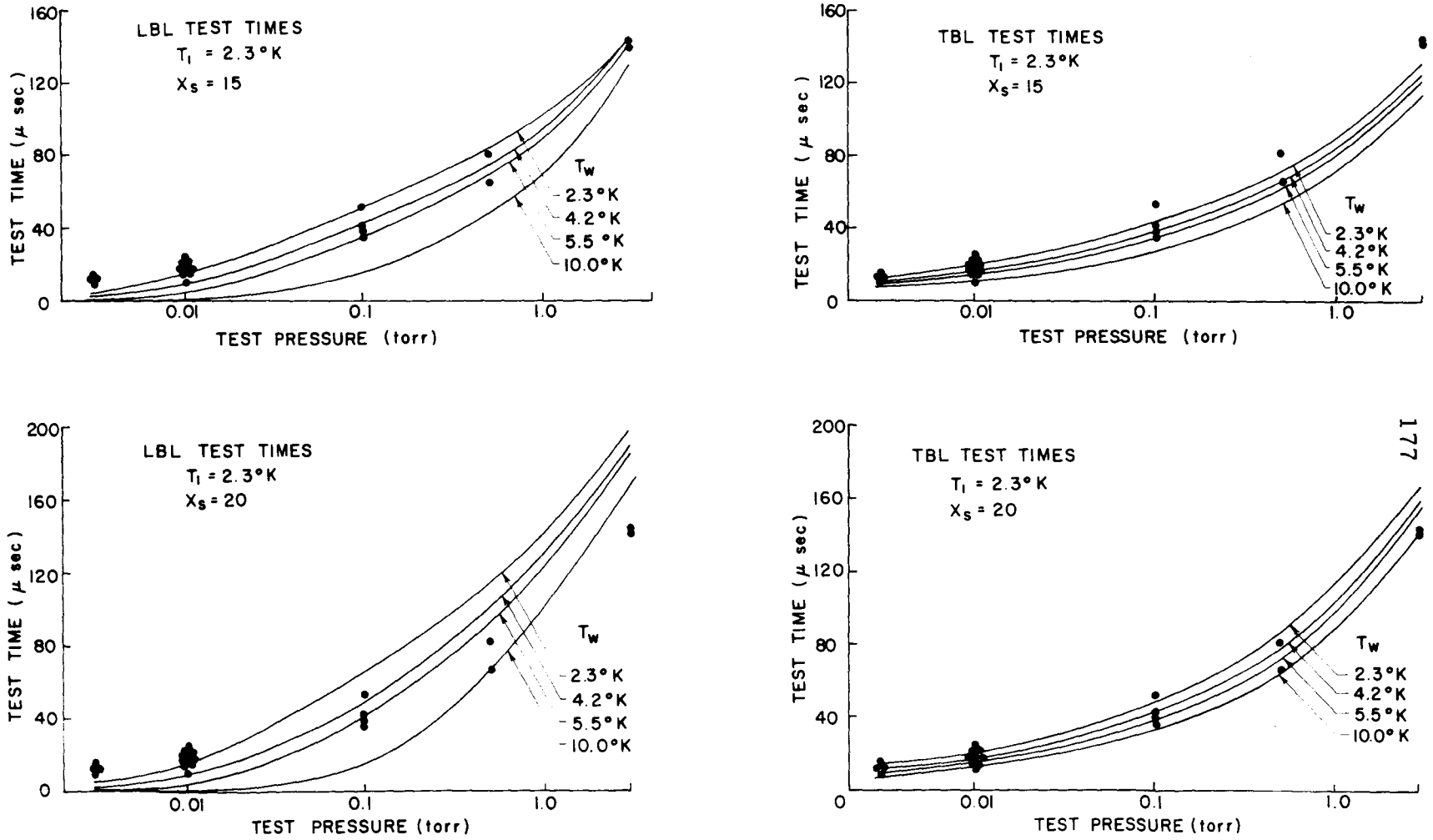

Figure 26. Comparison of Test Time Data with Theoretical Predictions for $T_1 = 2.3^{\circ}K$ (x_s = 15, 20)

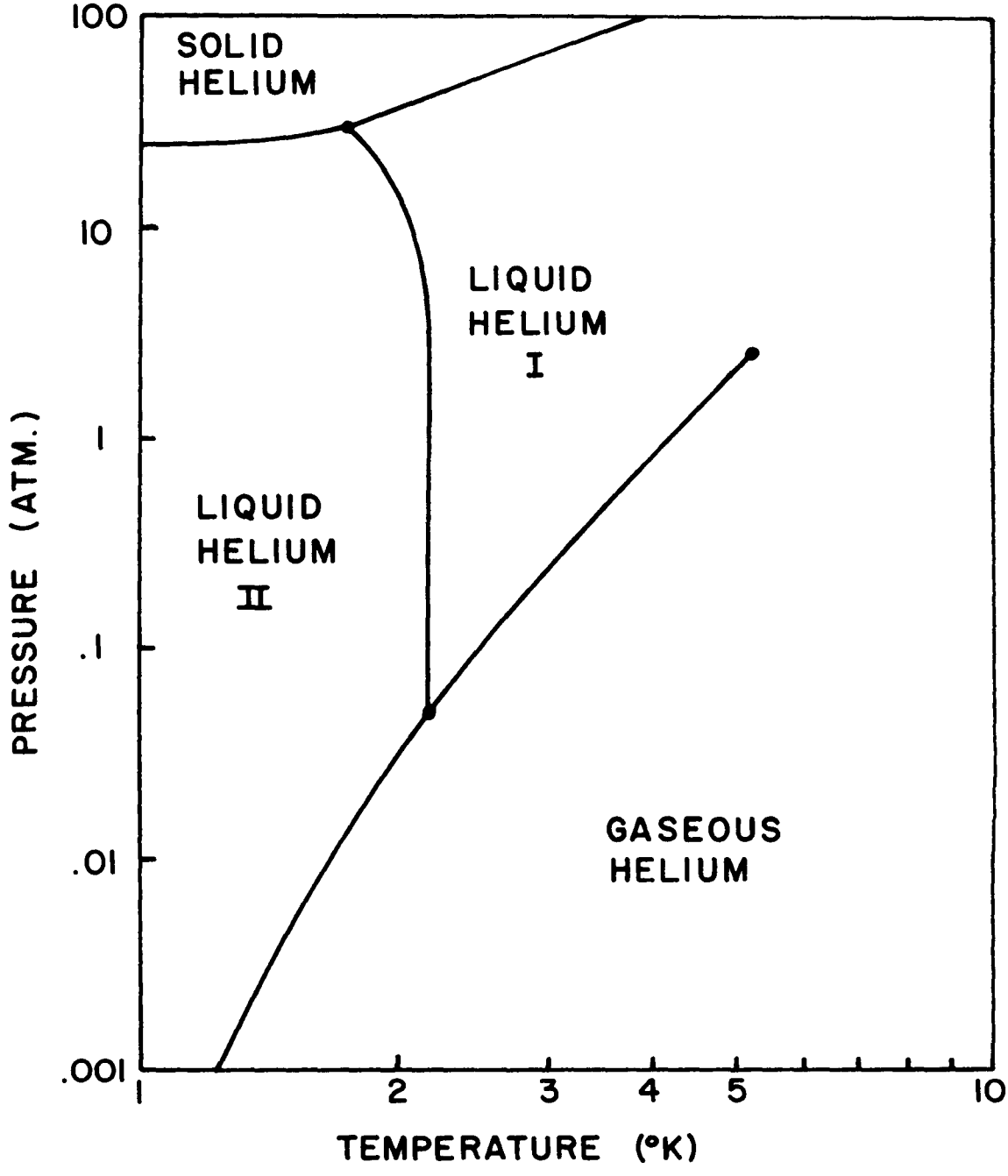

Figure 27. Pressure-Temperature Diagram for Helium

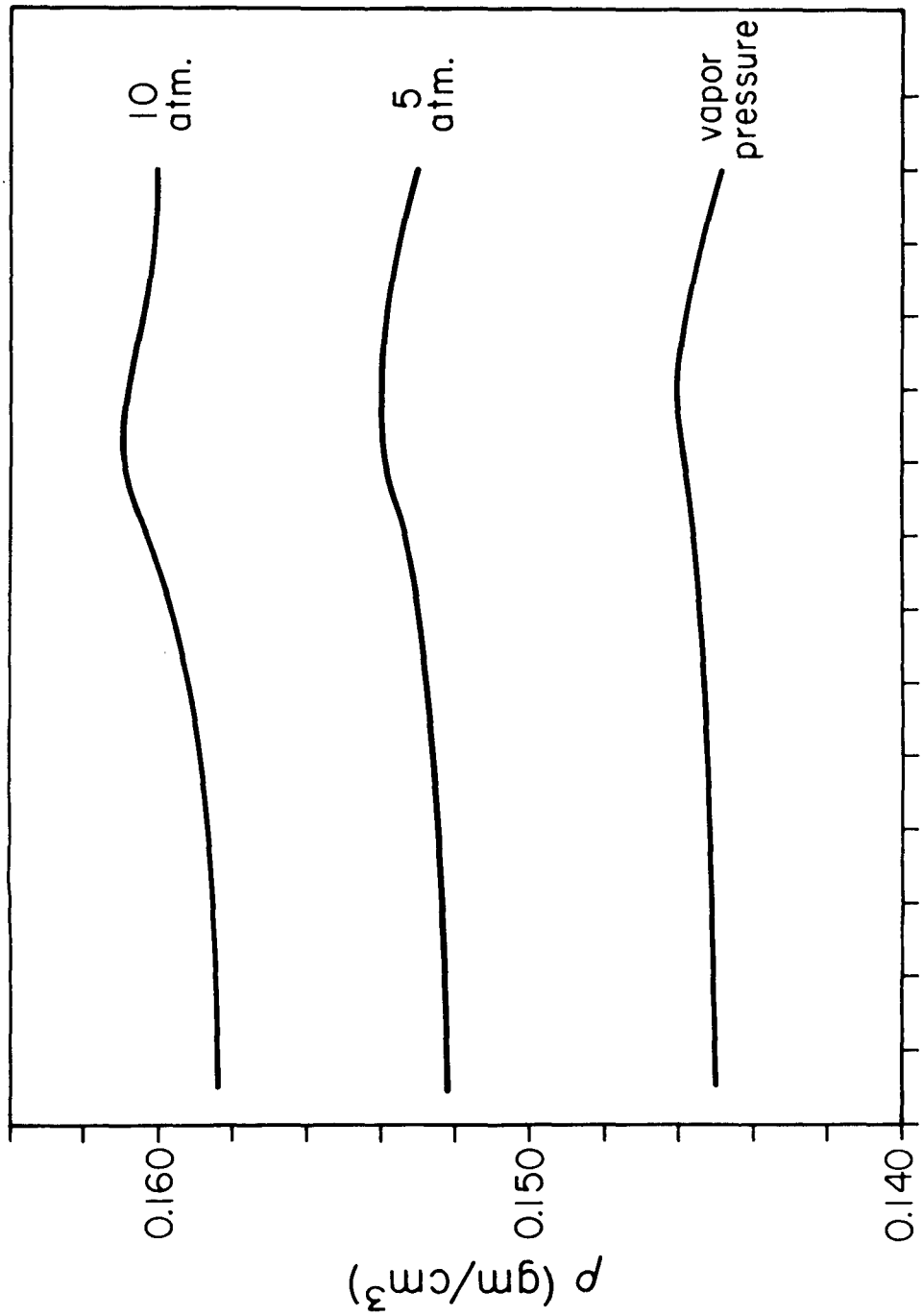

Figure 28. Variation of the Density of LHe with Temperature and Pressure

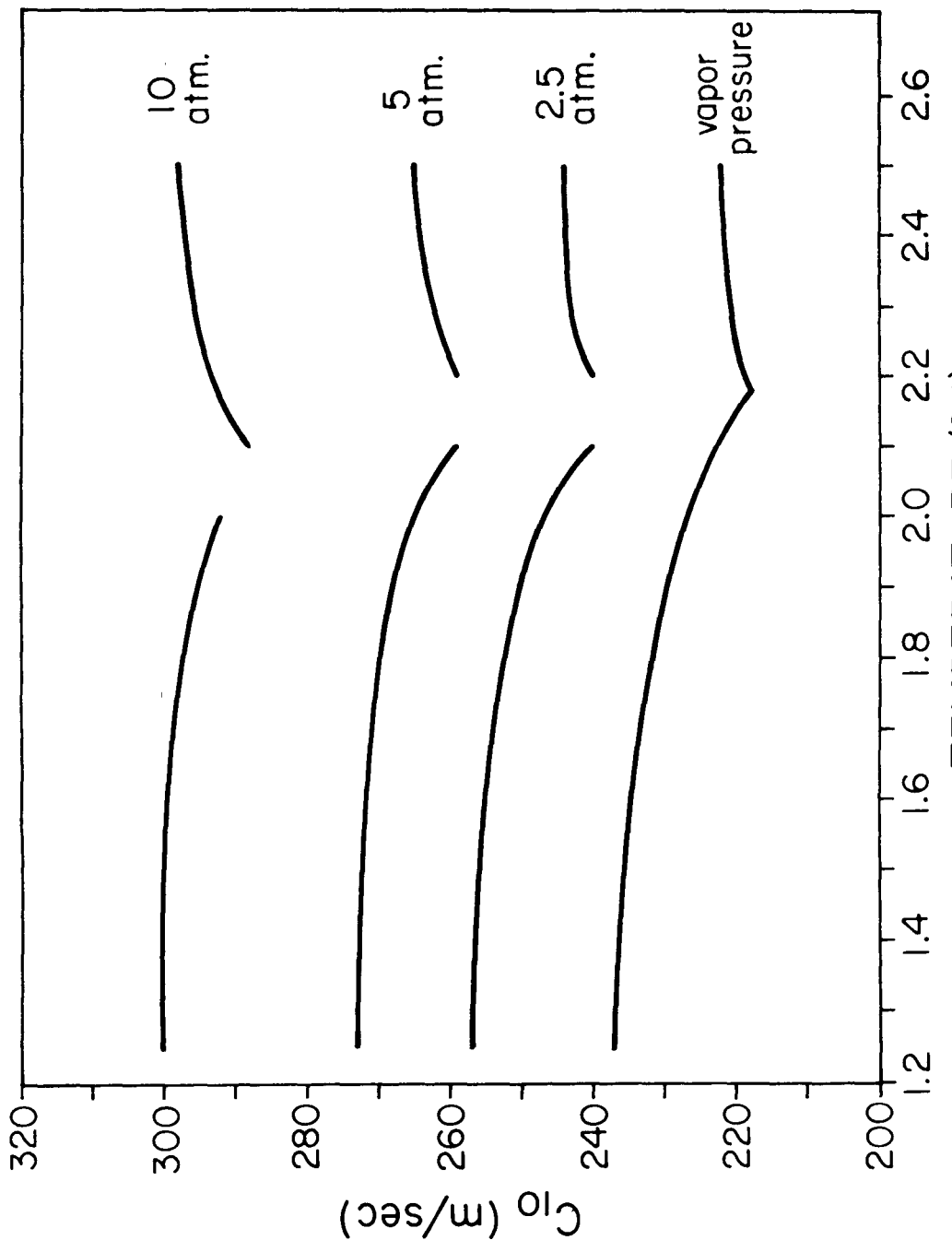

Figure 29. Variation of the Velocity of First Sound with Temperature and Pressure

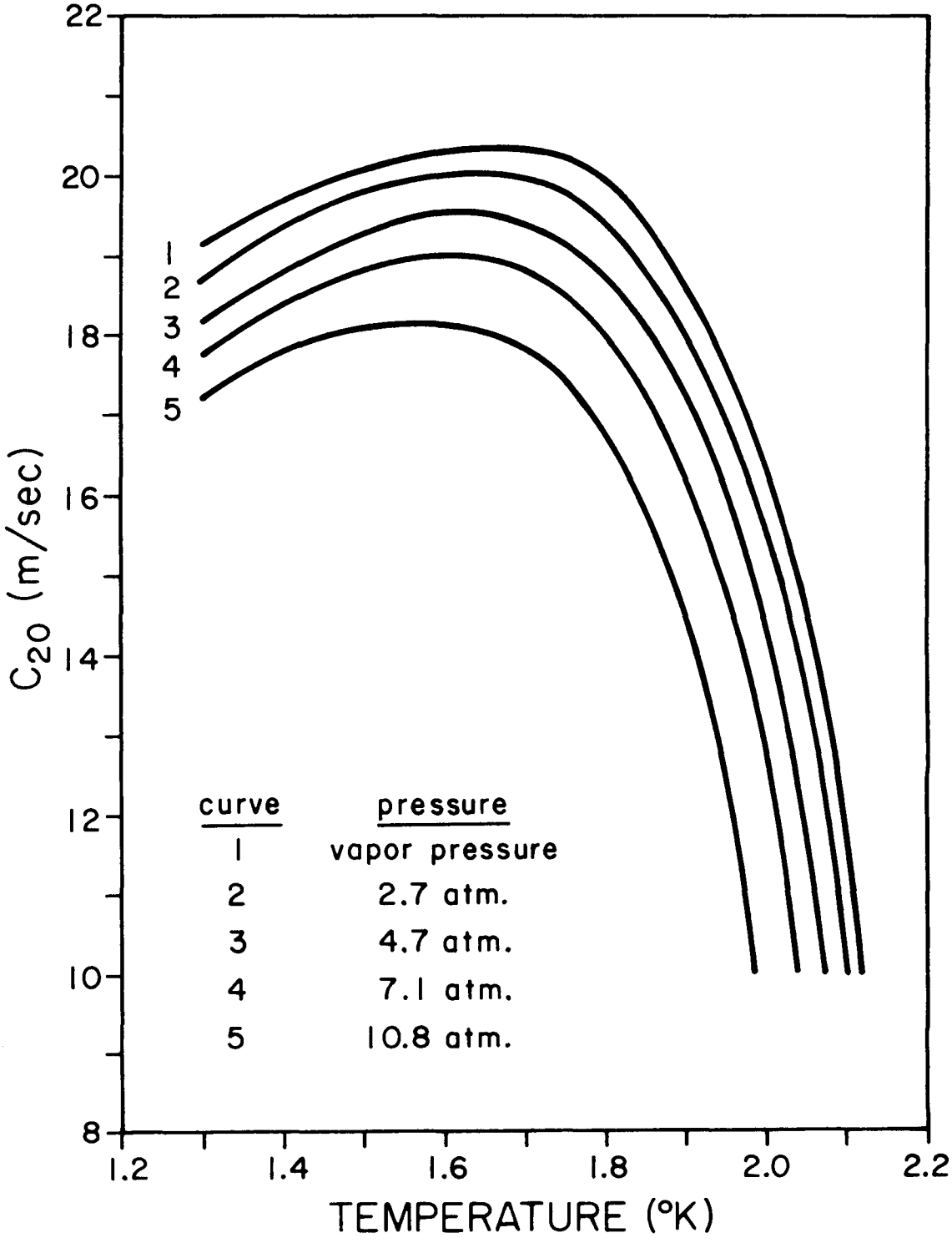

Figure 30. Variation of the Velocity of Second Sound with Temperature and Pressure

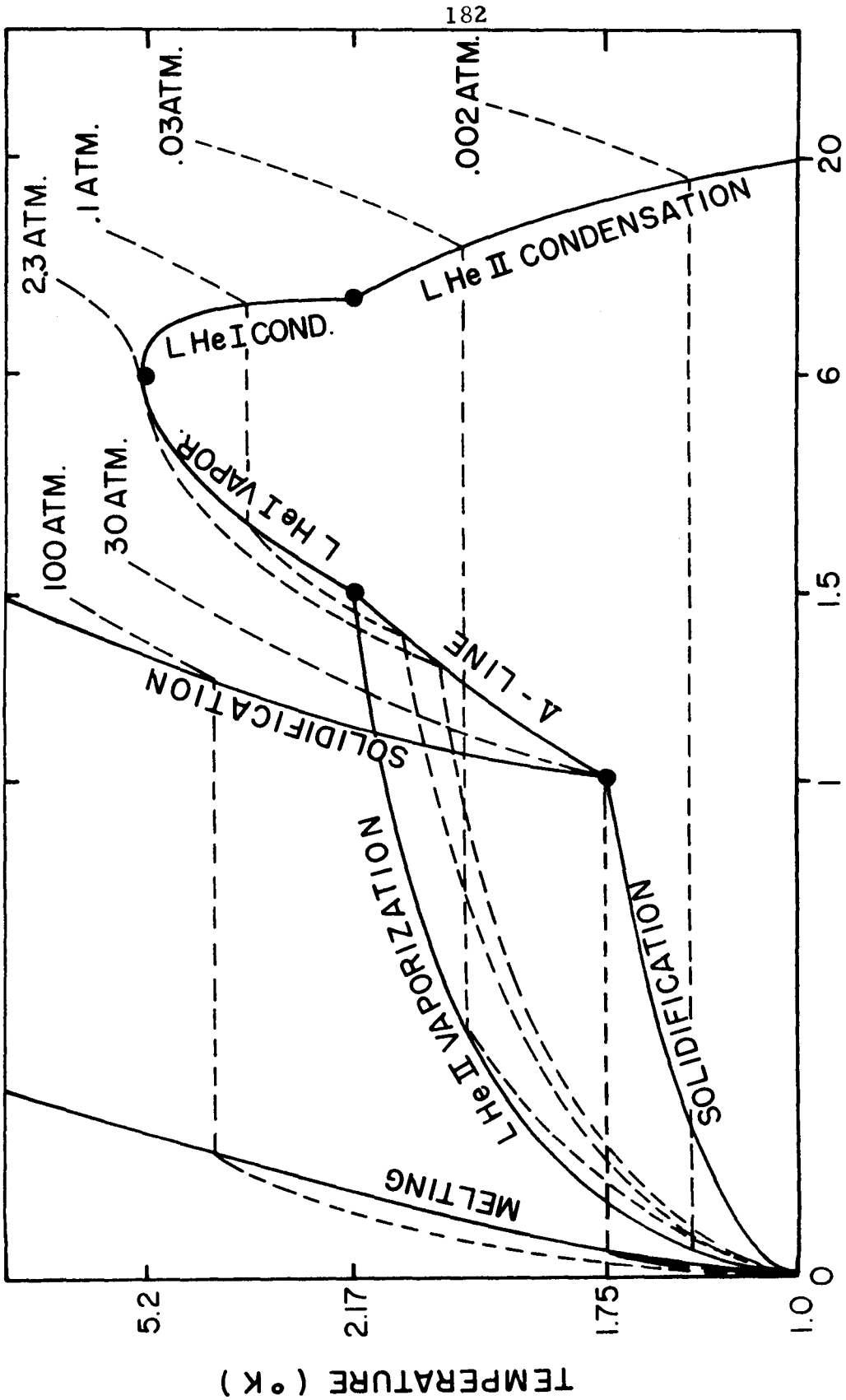

Figure 31. Temperature-Entropy Diagram for Helium (Not to Scale)

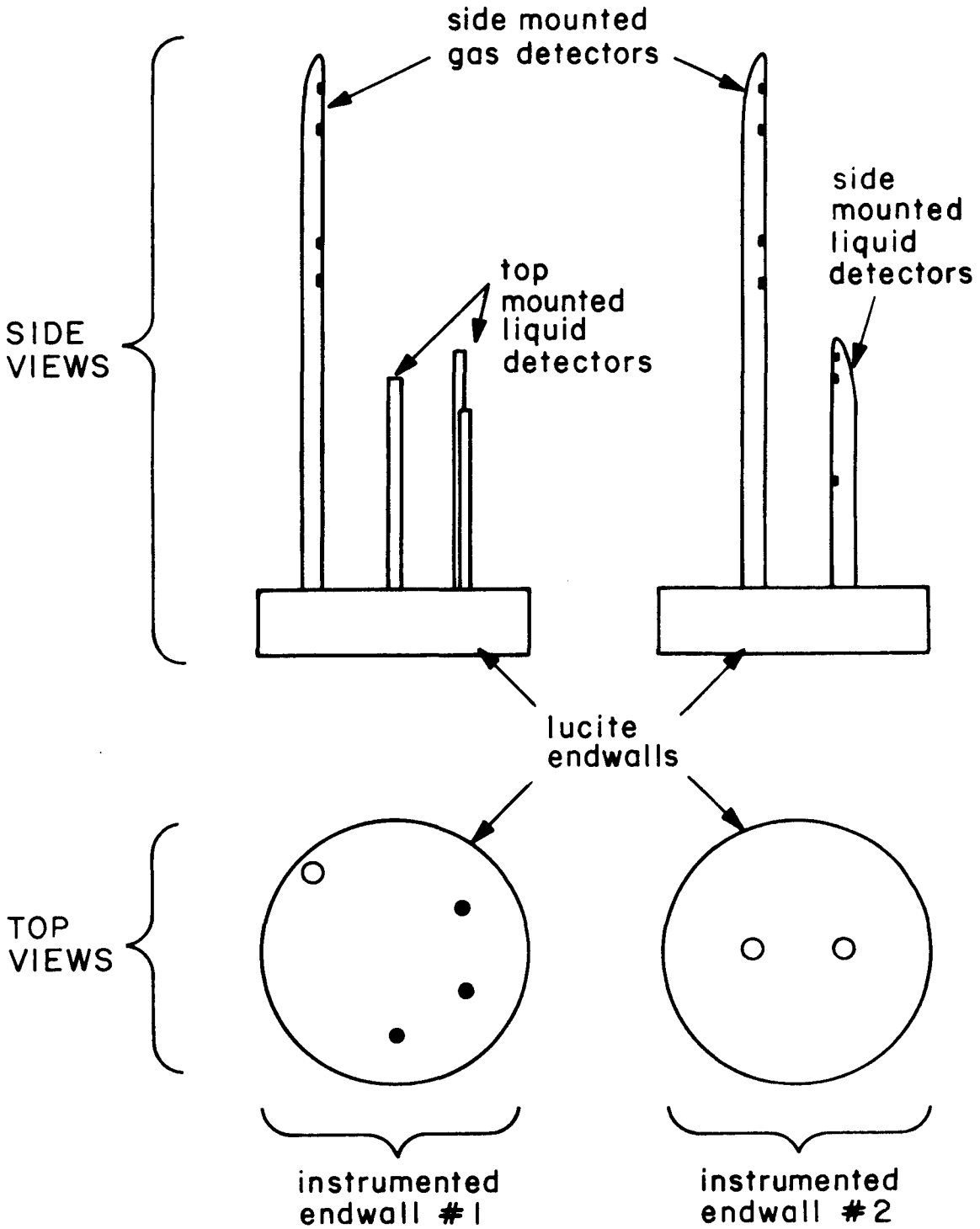

Figure 32. Instrumented Endwalls: Gas and Liquid Detectors

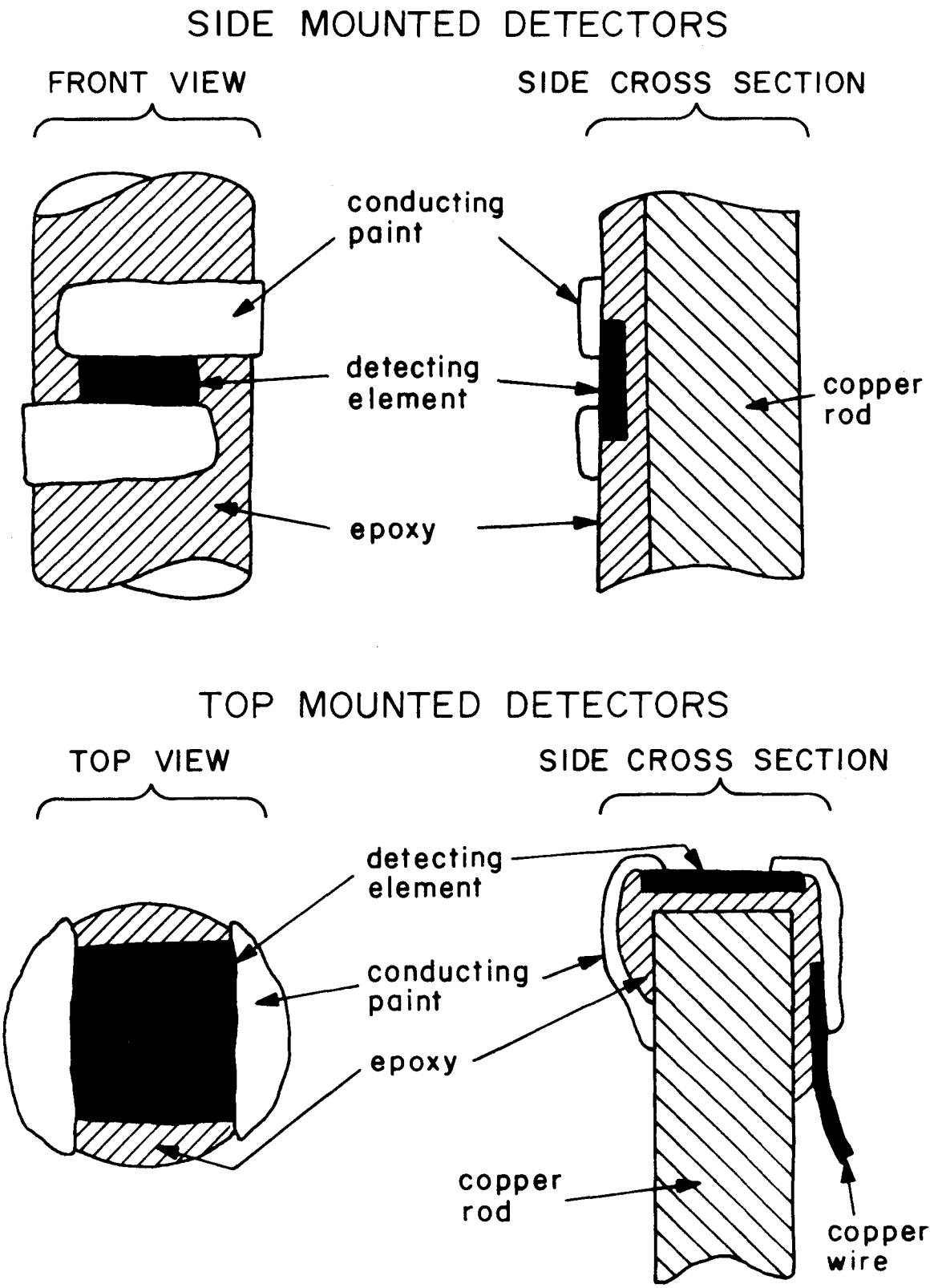

Figure 33. Construction of the Detectors

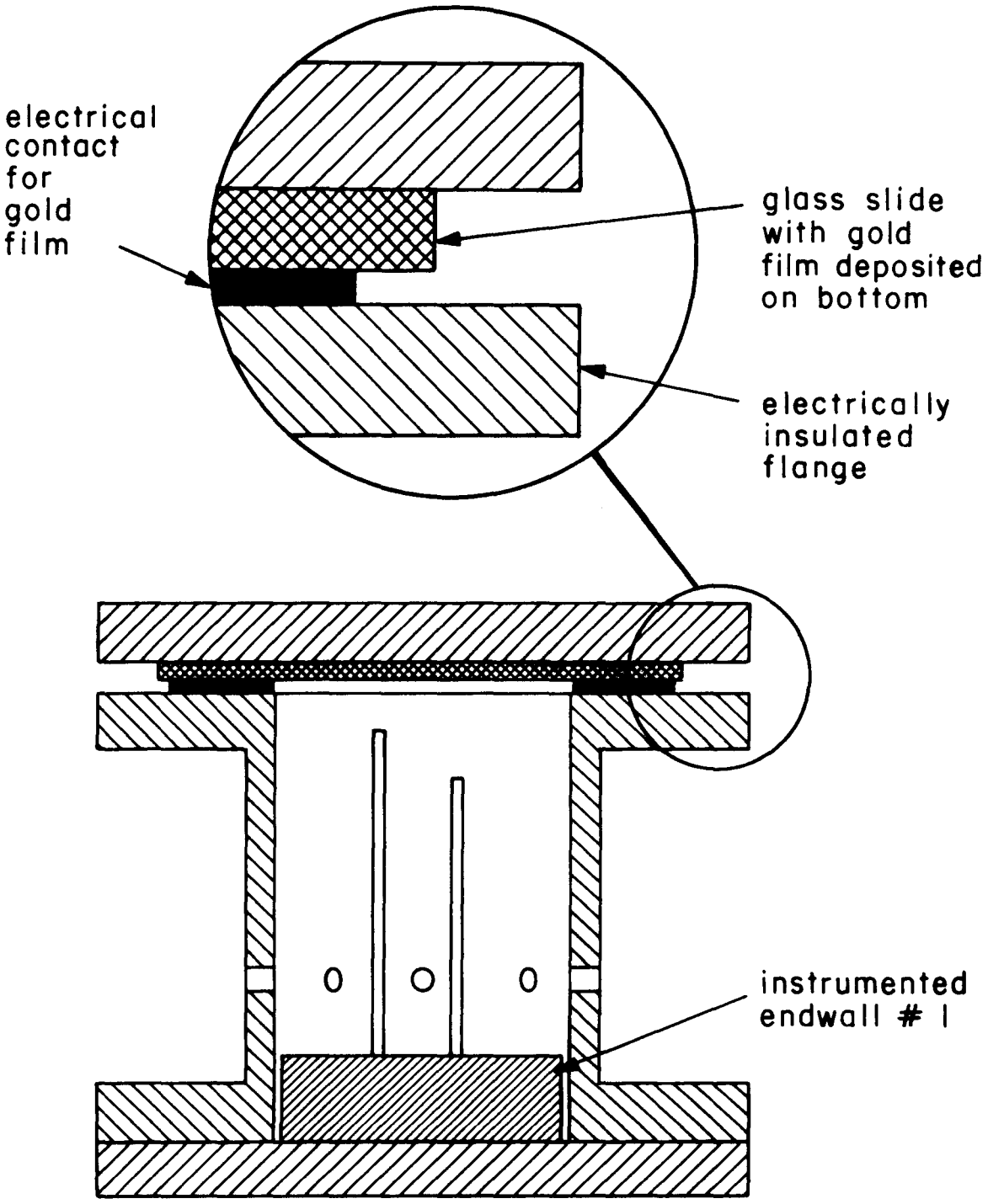

Figure 34. Schematic Drawing of the Calibration Cell

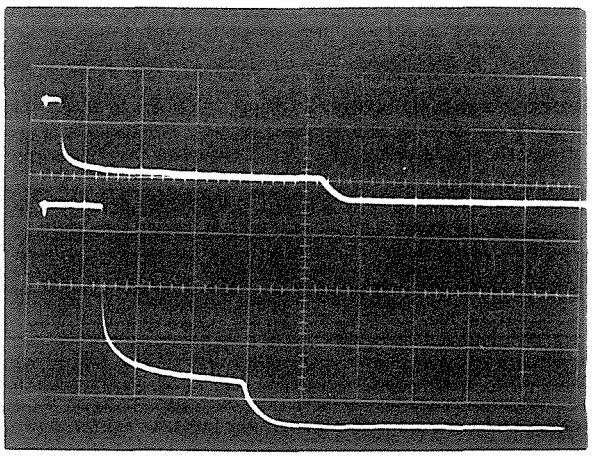

$P_1 = P_{s.v.} = 47$ torr

$T_1 = 2.26°K$

.02 volt/cm

50 μ sec/cm

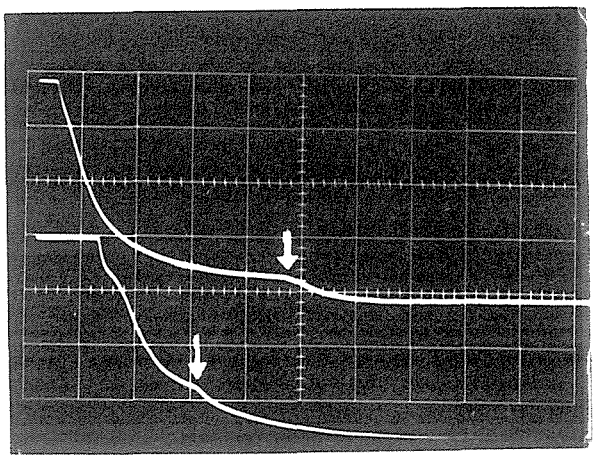

$P_1 = P_{s.v.} = 3$ torr

$T_1 = 1.46°K$

.04 volt/cm upper beam

.03 volt/cm lower beam

20 μ sec/cm

Figure 35. Response of the Gas Detectors to the Incident and Reflected Shock

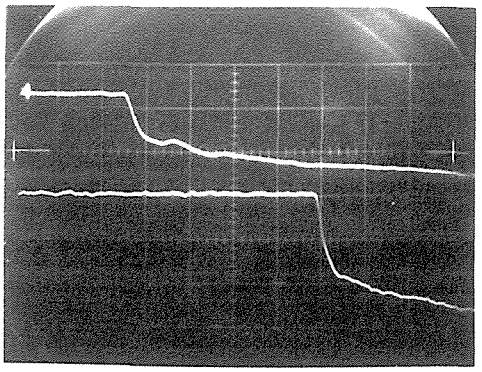

$P_1 = P_{S.V.} = 47$ torr
$T_1 = 2.26°K$
TOP MOUNTED DETECTORS
.2 volt/cm
5μsec/cm

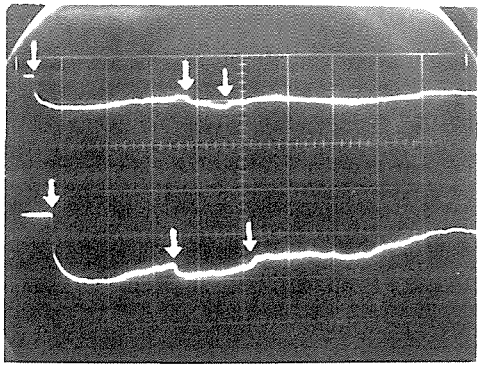

$P_1 = P_{S.V.} = 47$ torr
$T_1 = 2.26°K$
TOP MOUNTED DETECTORS
.5 volt/cm
50μsec/cm
(incident, reflected, and rereflected waves)

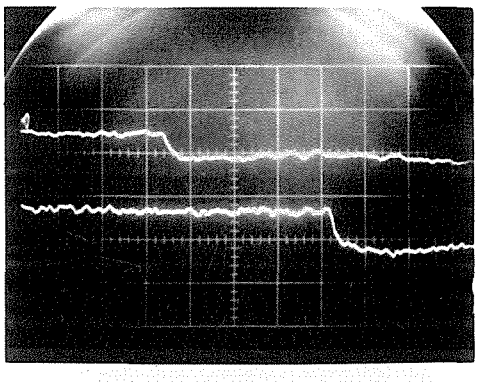

$P_1 = P_{S.V.} = 3$ torr
$T_1 = 1.46°K$
TOP MOUNTED DETECTORS
.05 volt/cm
5μsec/cm

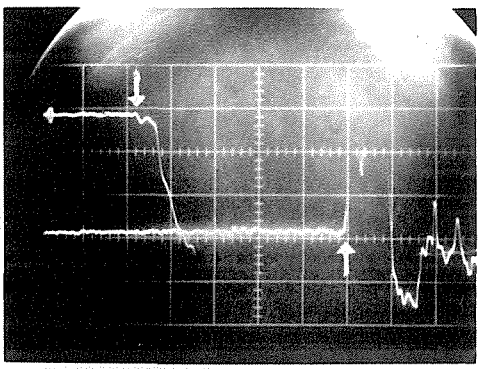

$P_1 = P_{S.V.} = 47$ torr
$T_1 = 2.26°K$
SIDE MOUNTED DETECTORS
.2 volt/cm
10μsec/cm

Figure 36. Response of the Liquid Detectors to the First Sound Wave

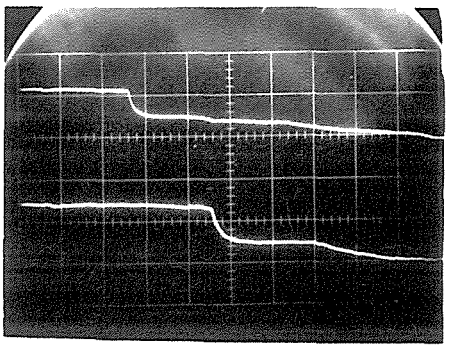

TOP MOUNTED DETECTORS
.5 volt/cm
50μ sec/cm

DATA TAKEN USING SHOCK TUBE

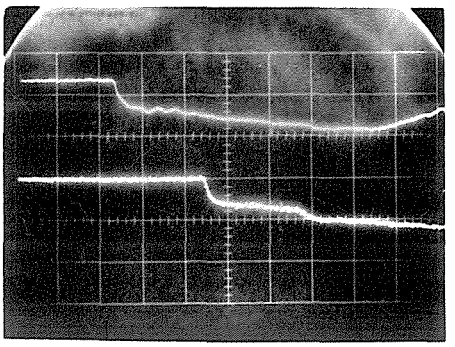

TOP MOUNTED DETECTORS
.2 volt/cm
50μ sec/cm

DATA TAKEN USING CALIBRATION CELL

electrical pulse { 15.6 watts/cm^2 amp.
300μ sec duration

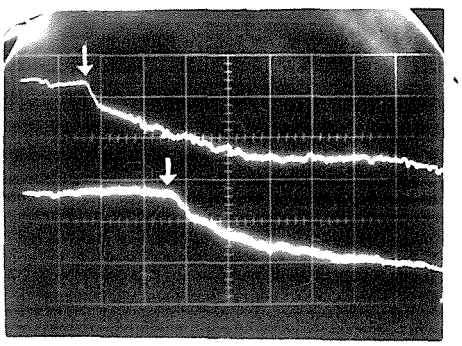

SIDE MOUNTED DETECTORS
.2 volt/cm
50μ sec/cm

DATA TAKEN USING SHOCK TUBE

Figure 37. Response of the Liquid Detectors to Second Sound Waves: Shock Tube and Calibration Cell Data (Initial Temperature 1.46°K)

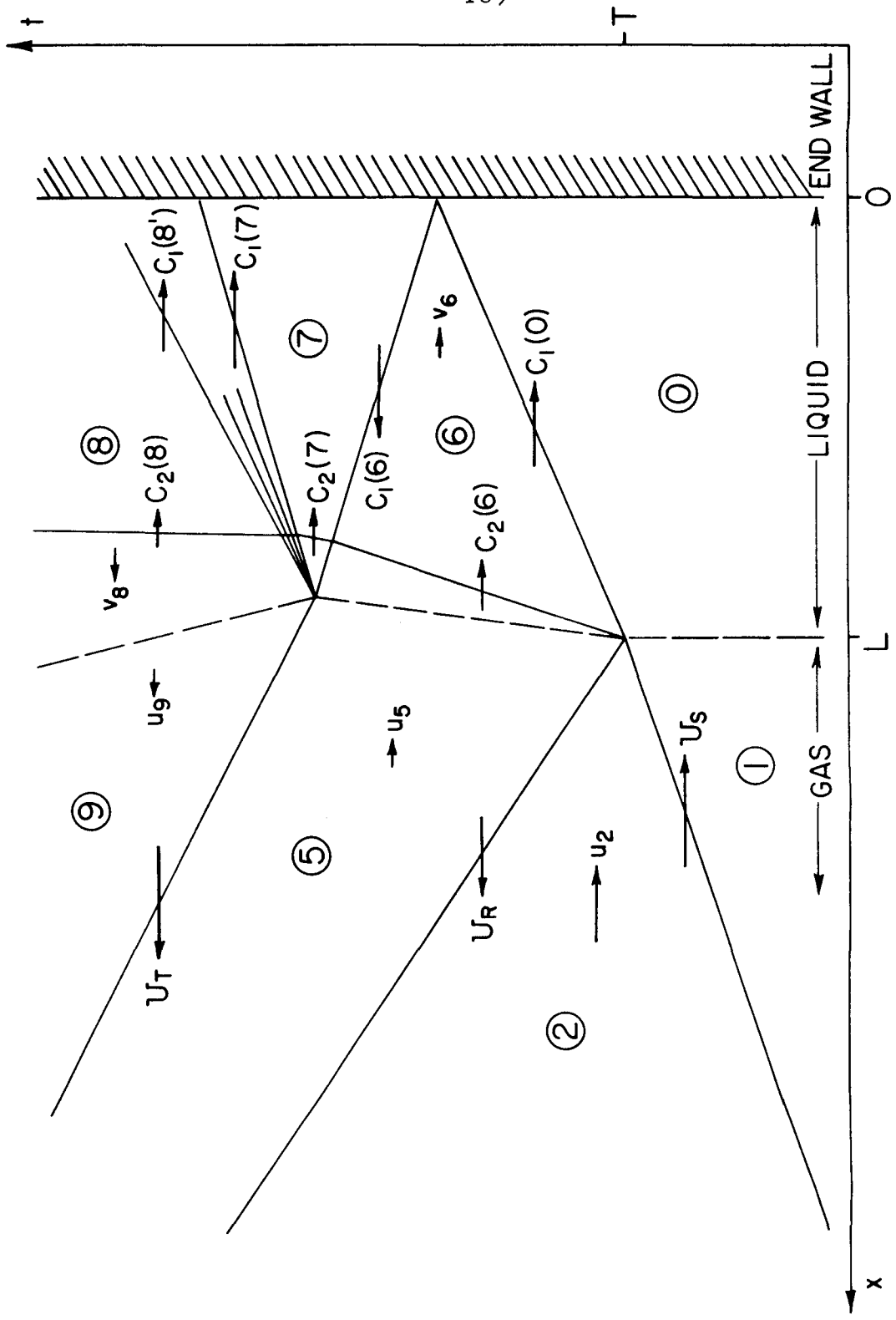

Figure 38. x-t Diagram: Notation and Concepts

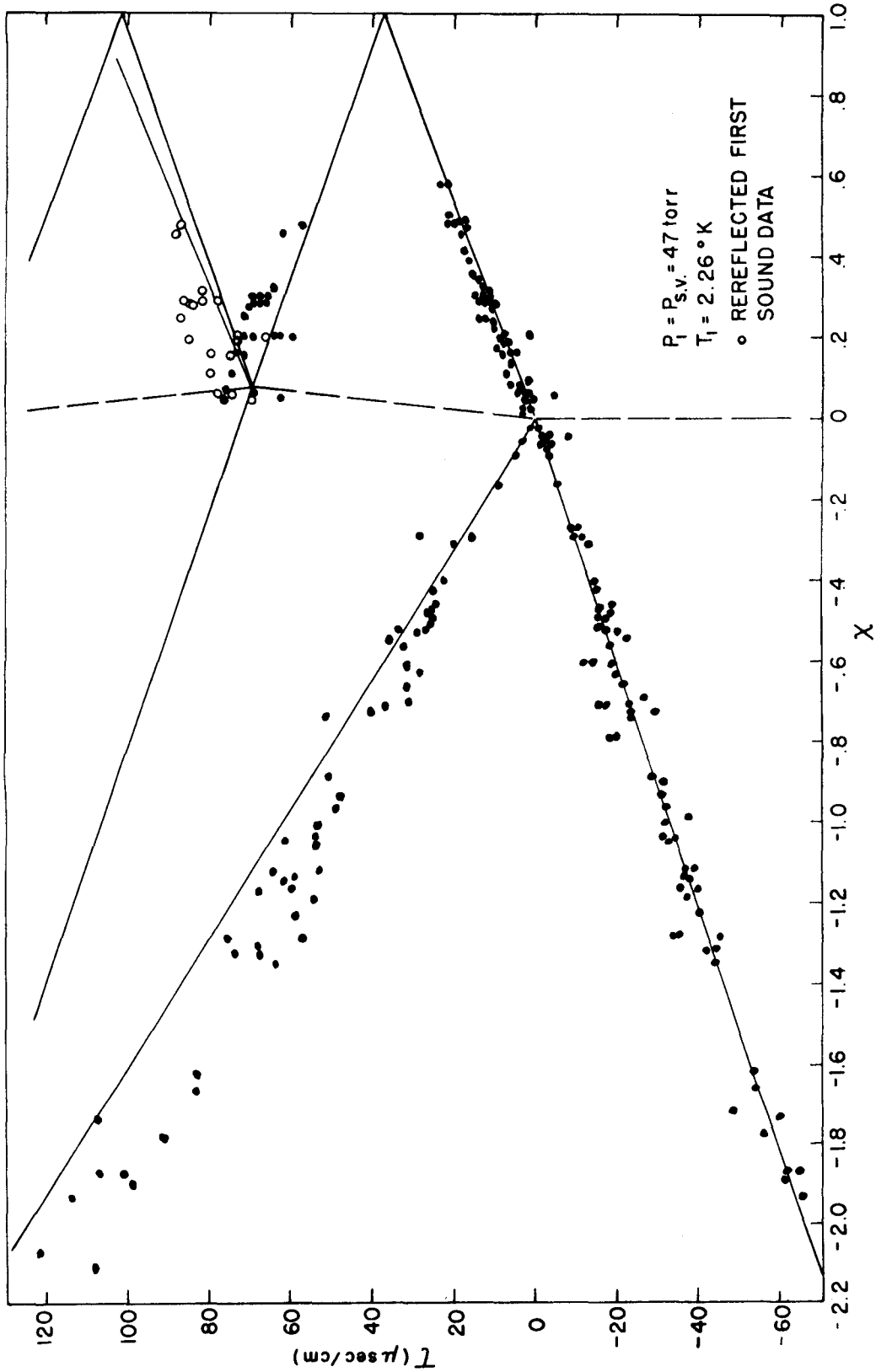

Figure 39. χ-τ Diagram for $T_1 = 2.26^{\circ}K$

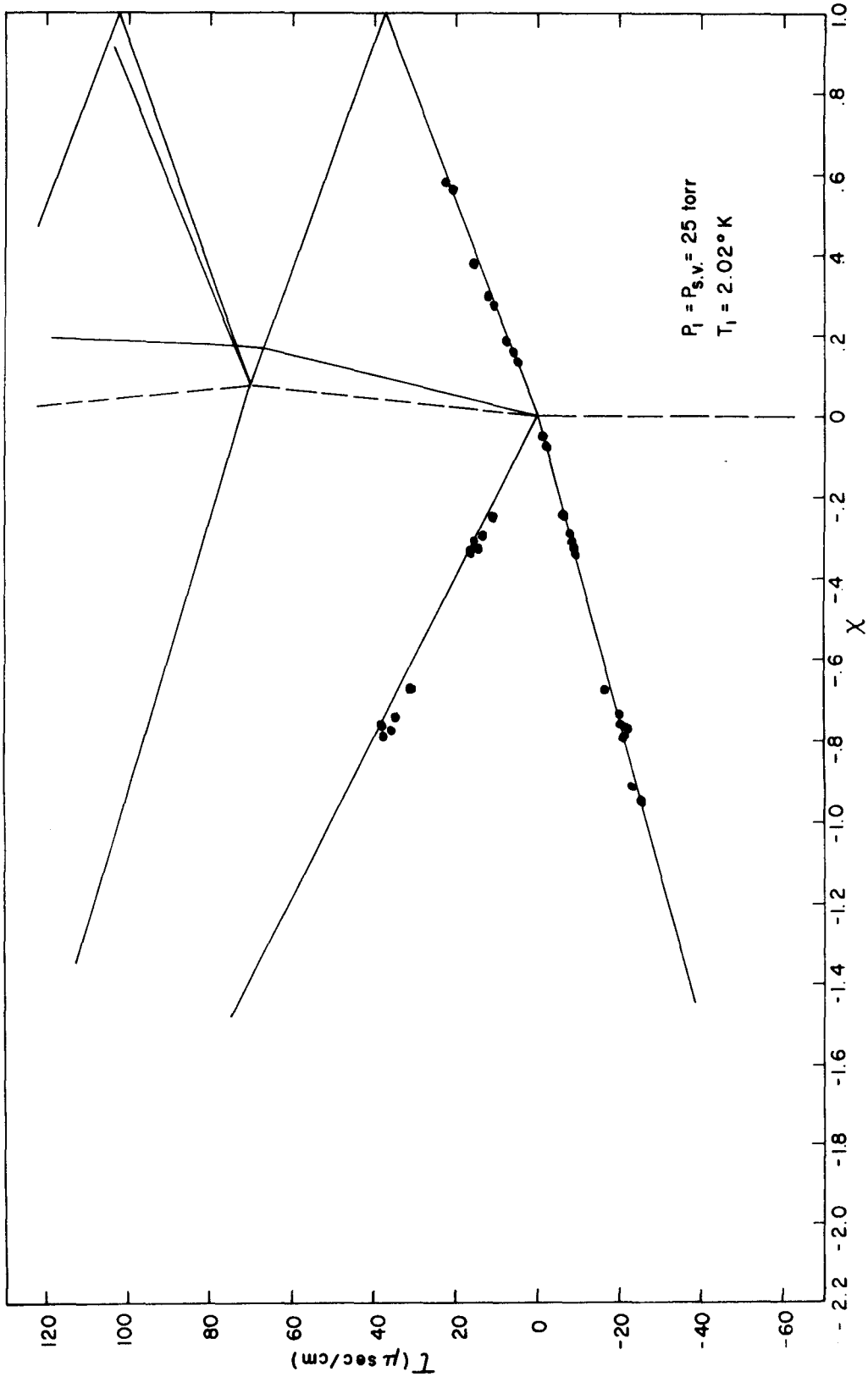

Figure 40. χ-τ Diagram for $T_1 = 2.02^{\circ}K$

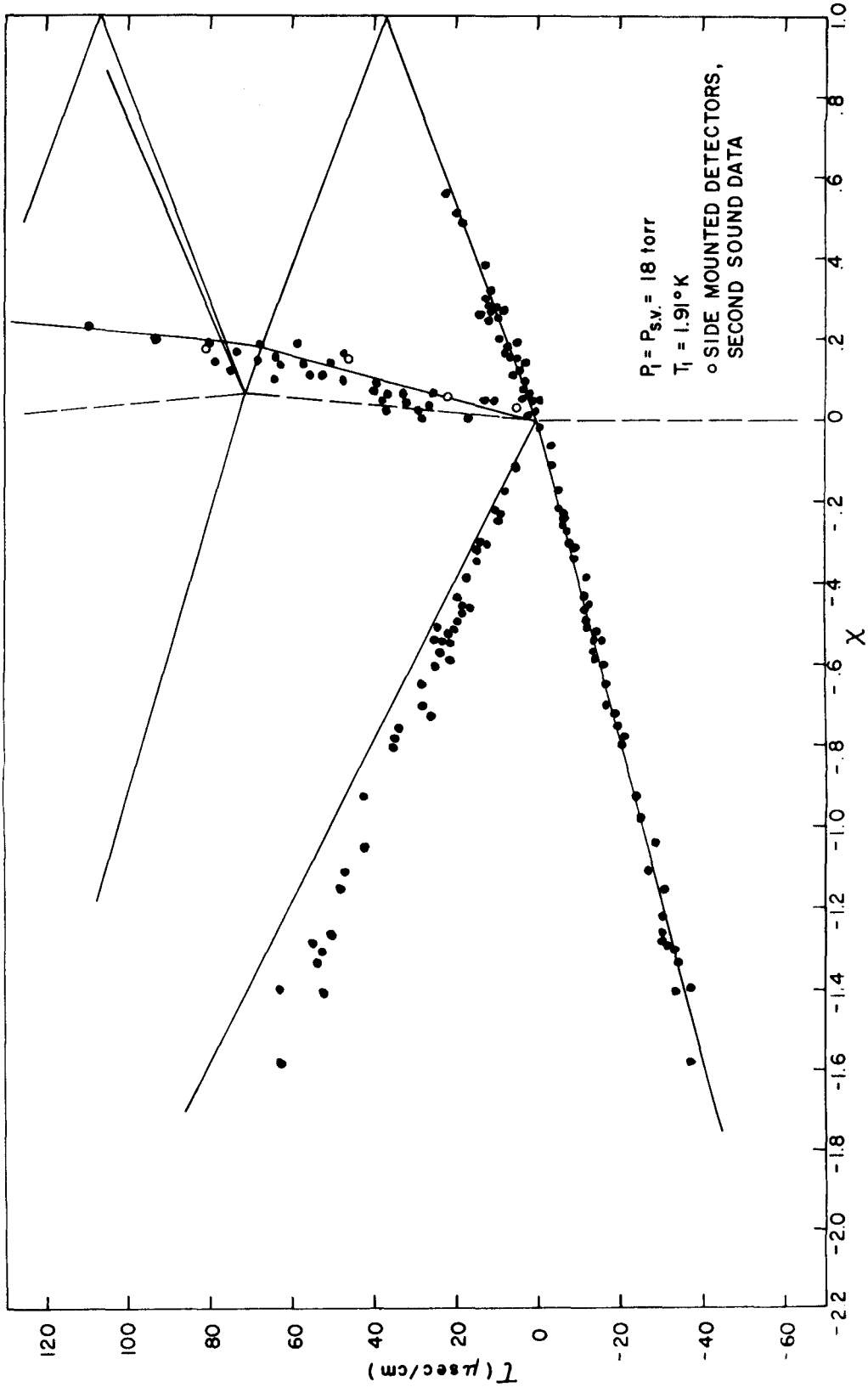

Figure 41. χ-τ Diagram for $T_1 = 1.91^{\circ}K$

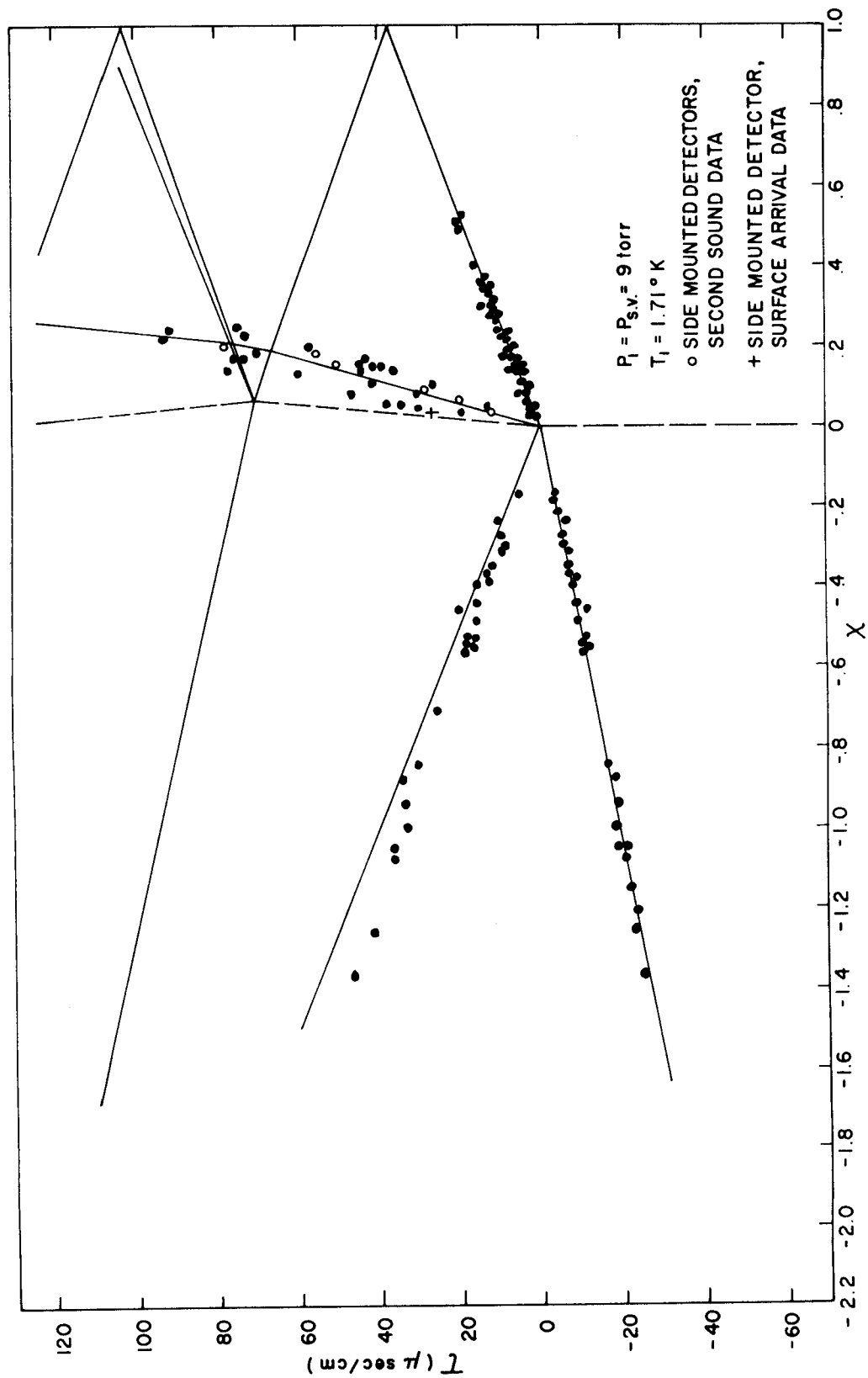

Figure 42. χ-τ Diagram for $T_1 = 1.71^{\circ}K$

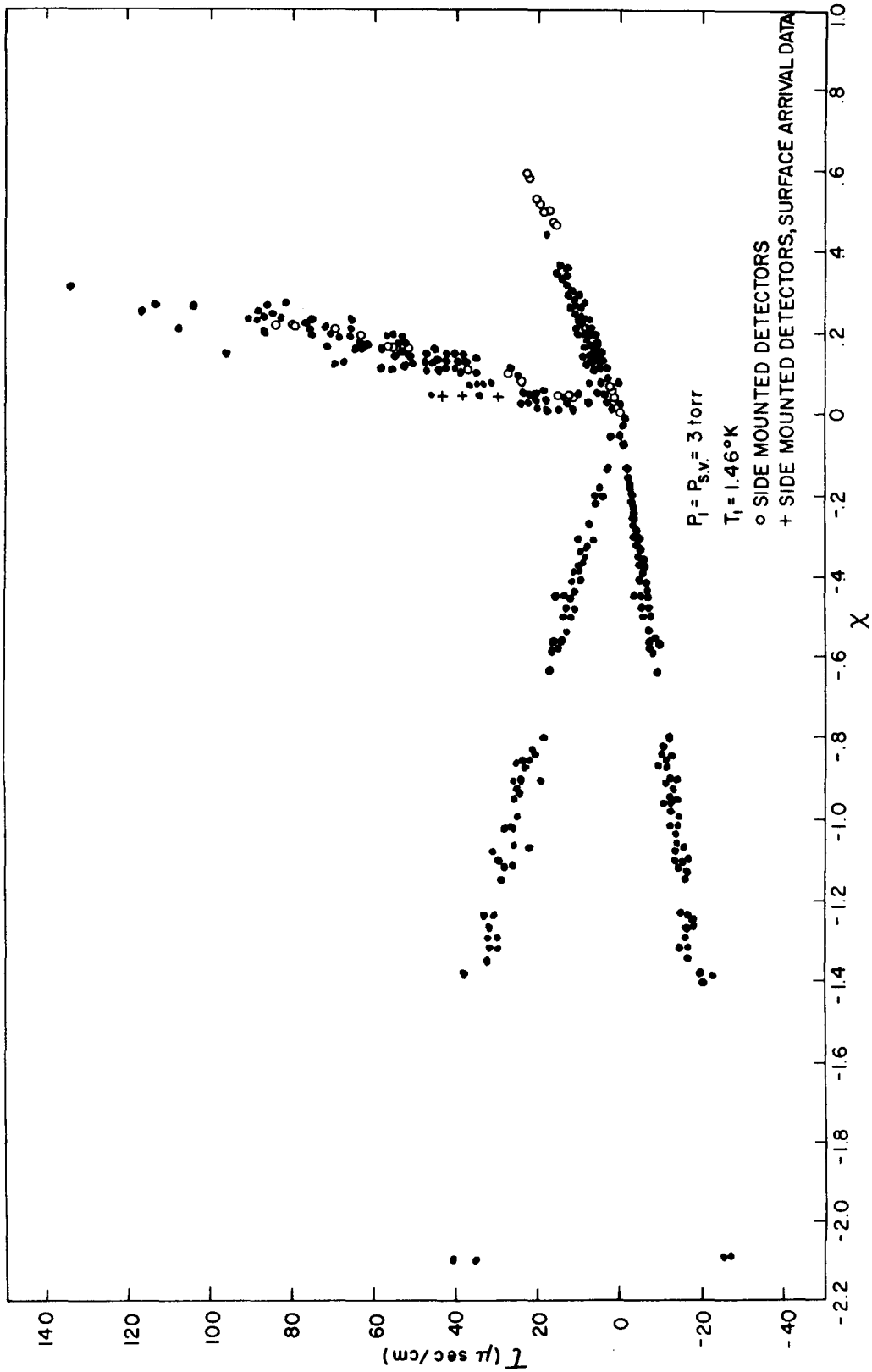

Figure 43. (χ, τ) Data for $T_1 = 1.46^{\circ}K$

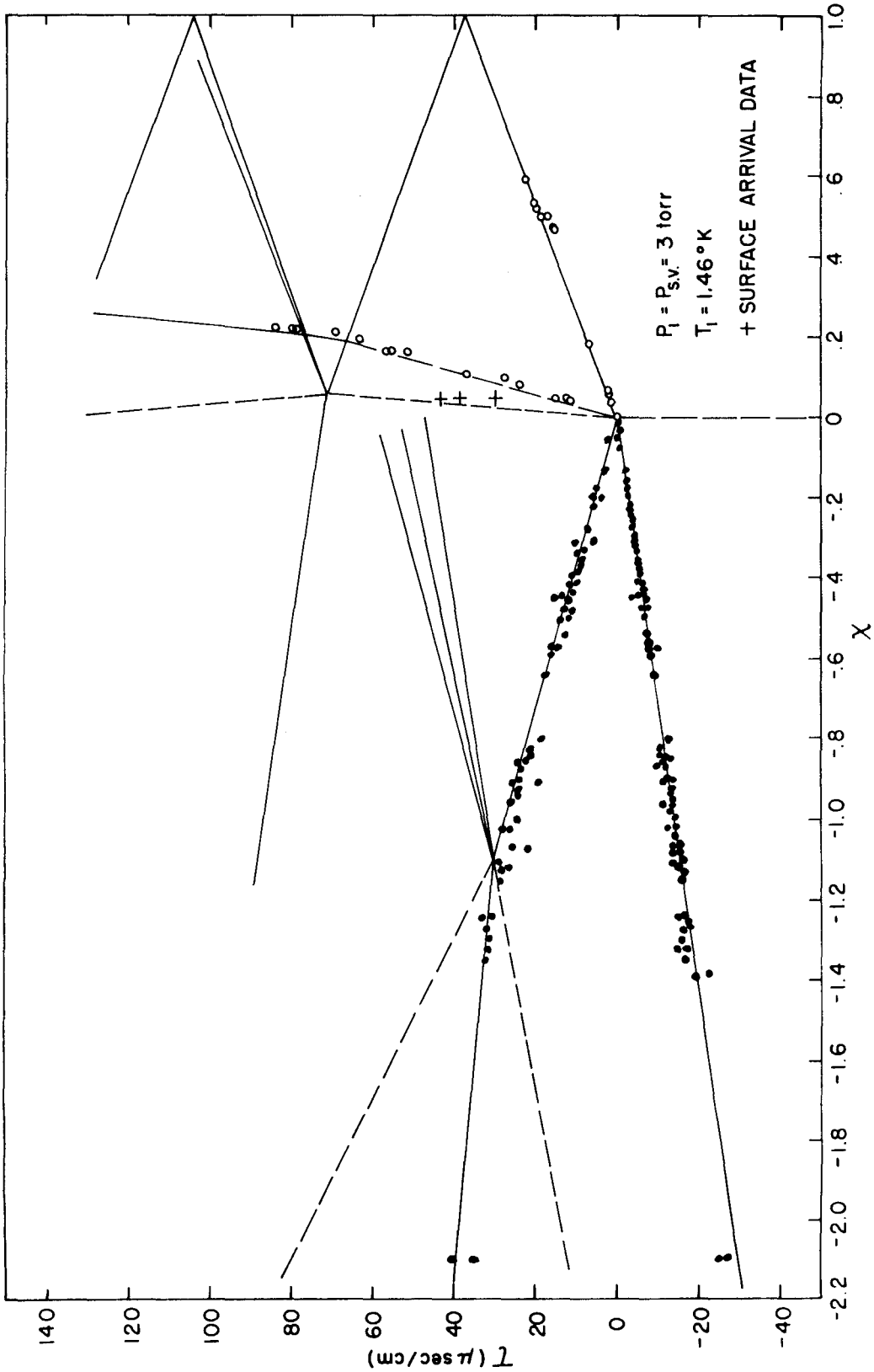

Figure 44. χ-τ Diagram for $T_1 = 1.46^{\circ}K$ (Side Mounted Liquid Detector Data Only)

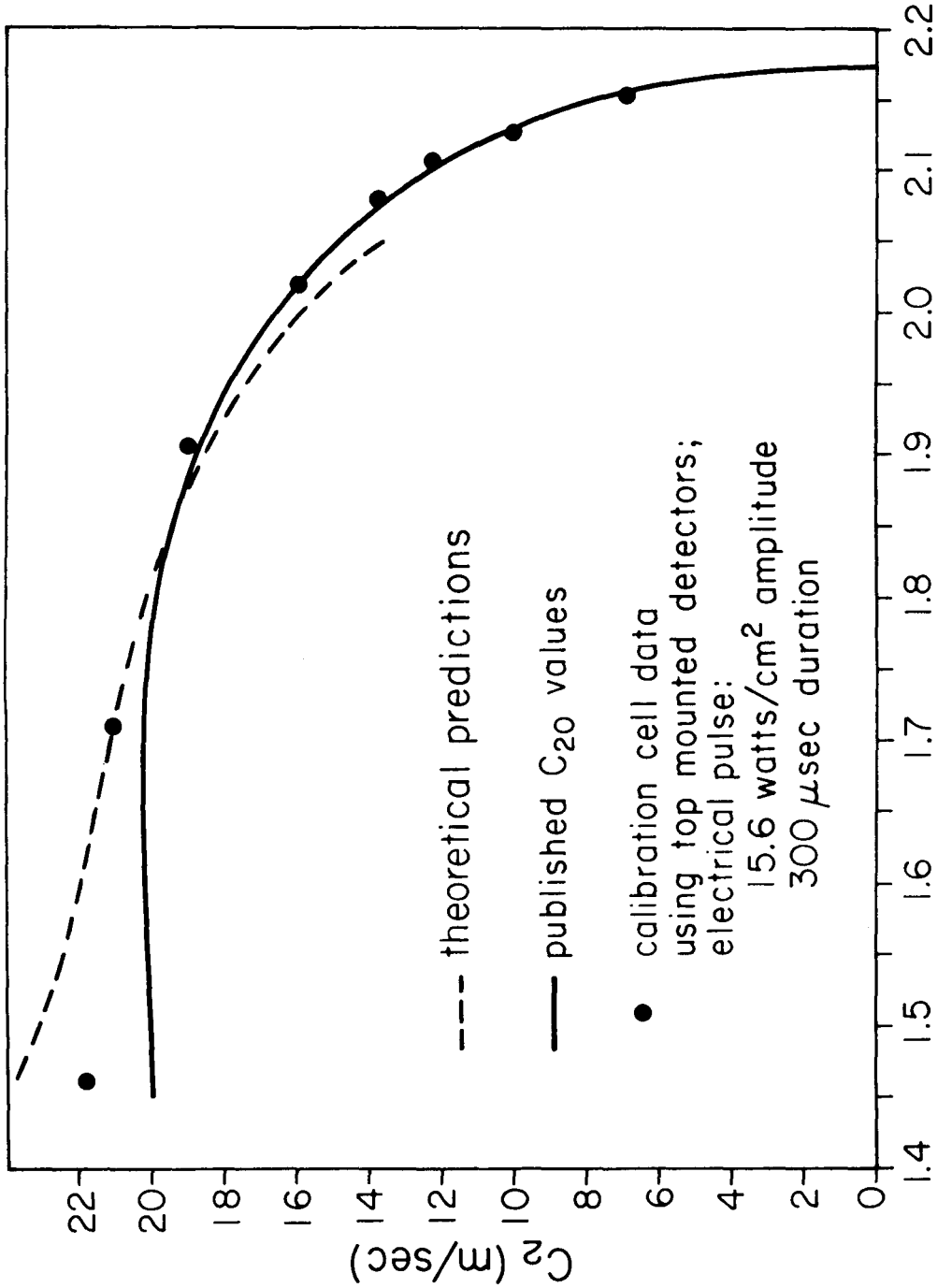

Figure 45. Comparison of Calibration Cell C_2 Data with Theoretical Predictions and C_{20} Values

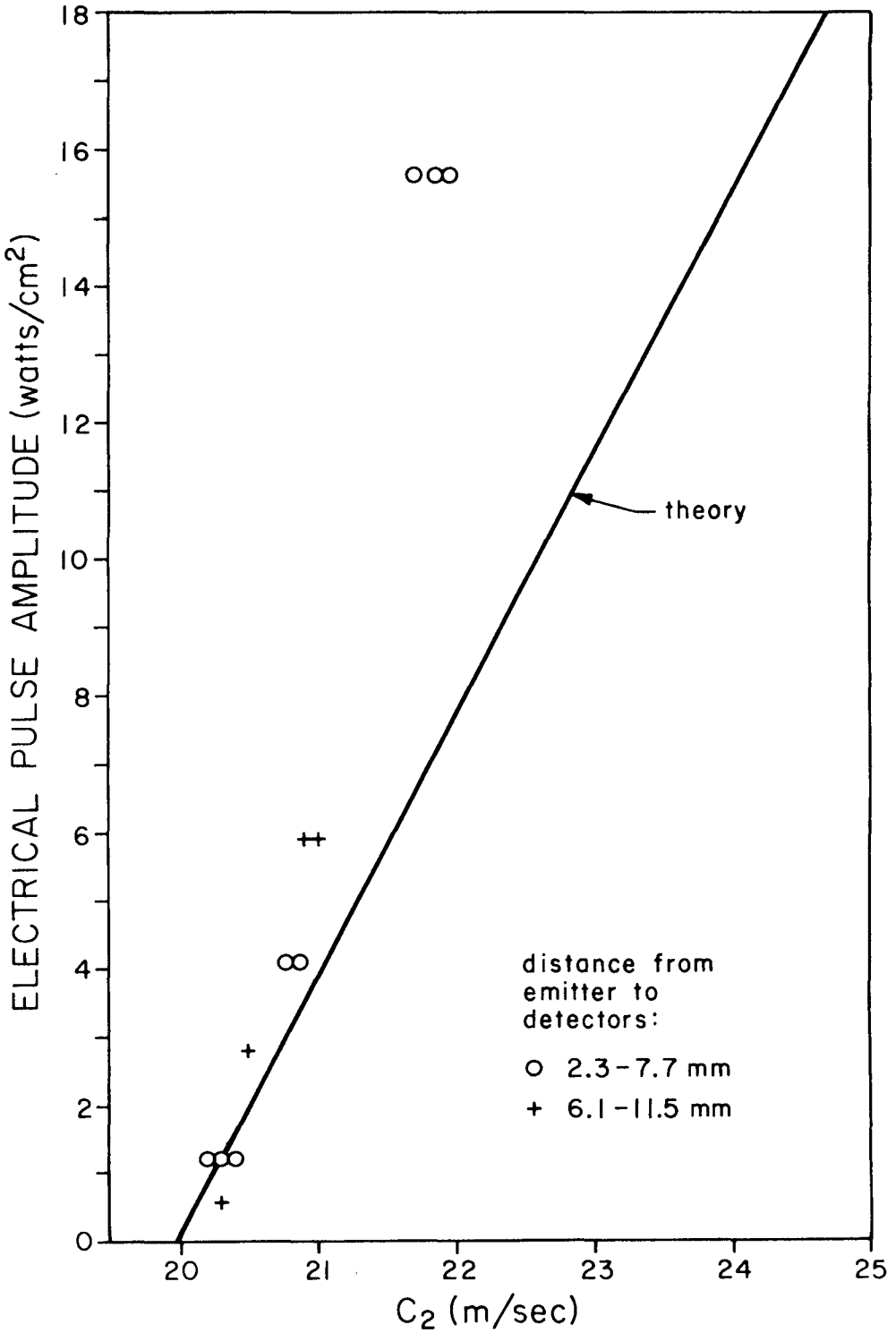

Figure 46. Comparison of Calibration Cell Data with Theoretical Predictions (Initial Temperature 1.46°K)

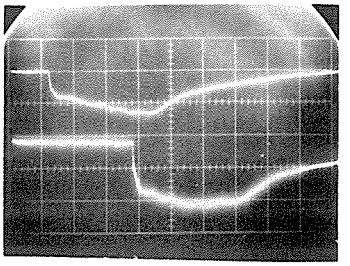

T_I = 1.46°K
. 2 volt/cm

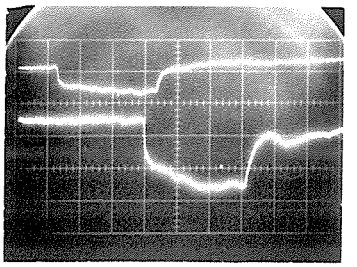

T_I = 1.71°K
.05 volt/cm upper beam
. I volt/cm lower beam

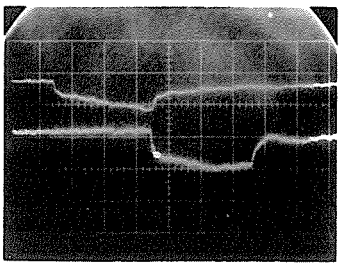

T_I = 1.91°K
. I volt/cm

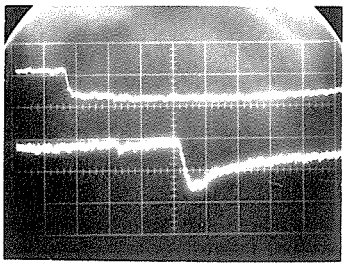

T_I = 2.02°K
.05 volt/cm

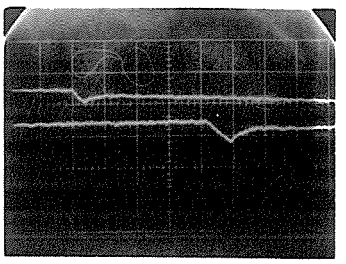

T_I = 2.08°K
. I volt/cm

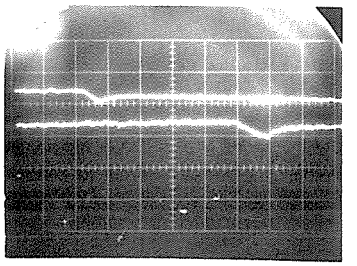

T_I = 2.107°K
. I volt/cm

TOP MOUNTED DETECTOR OUTPUTS USING THE CALIBRATION CELL. SAME TWO DETECTORS ON ALL OSCILLOGRAMS.

time scale : 100 μsec/cm

electrical pulse { 15.6 watts/cm^2 amplitude
300 μsec duration

Figure 47. Typical Calibration Cell Data